DIPLOMARBEIT

2D Finite Element Analysis Simulation Framework in OPERA2D

zur Erlangung des akademischen Grades

Diplom-Ingenieur/in

im Rahmen des Studiums

Biomedical Engineering – Medical Physics

eingereicht von

Lisa Suette
Matrikelnummer 11810035

ausgeführt am
Atominstitut der Fakultät für Physik der Technischen Universität Wien (TU Wien)

in Zusammenarbeit mit der
Europäischen Organisation für Kernforschung (CERN)

Betreuung
Betreuer/in: **Privatdoz. Dipl.-Ing. Dr.techn. Michael Benedikt** (TU Wien, CERN)
und
Thomas Zickler (CERN)

Genf, 27.01.2025

(Unterschrift Verfasser/in)

(Unterschrift Betreuer/in)

Acknowledgments

First and foremost, I would like to express my sincere gratitude to my advisor, Thomas Zickler, for his invaluable support throughout this thesis. He was always available to answer my questions and provided valuable input thanks to his broad knowledge. I am especially grateful for the freedom he gave me to develop and pursue my own ideas and approaches.

I would also like to thank my professor, Privatdoz. Dipl.-Ing. Dr.techn. Michael Benedikt, for granting me the extraordinary opportunity to write my master's thesis at CERN. His continuous support throughout my time at CERN was invaluable, and I deeply appreciate his guidance.

Furthermore, I am grateful to all my colleagues whom I had the pleasure of meeting during my research. The many discussions and the knowledge exchanged, as well as the emotional support, were essential to the completion of this work. In particular, I would like to thank Markus Brugger, Florian Stummer, Maarten Van Dijk, Laurence James Nevay, Lau Gatignon, Deepti Kadhol, Kieran Geiger, Fabian Metzger, Angelique Foussat, and Natalya Kahn.

Lastly, I want to express my deepest gratitude to my family—my parents, my sisters, and my partner. Their constant encouragement, patience, and unconditional support have been invaluable throughout this journey. They were always there to listen, to motivate me, and to stand by my side, helping me navigate even the most challenging decisions.

Zusammenfassung

Diese Masterarbeit befasst sich mit der präzisen Modellierung zweidimensionaler Magnetfelder für die Strahlführungslinien in der North Area (NA) am CERN. Genau berechnete Magnetfeldkarten sind essenziell für verlässliche Strahlsimulationen. Dennoch fehlen für viele Magnete in der NA entweder präzise Feldkarten oder die vorhandenen Karten weisen unzureichende Genauigkeit auf. Die Hauptursachen für diese Ungenauigkeiten liegen in Unsicherheiten bezüglich der Materialeigenschaften der Magnetjoche sowie in inkonsistenten Simulationsmethoden. Diese Faktoren können erhebliche Fehler in der Strahloptik verursachen und somit die Qualität experimenteller Ergebnisse beeinträchtigen.

Um dieses Problem zu lösen, wurde ein simulationsbasiertes Framework entwickelt, das eine validierte und reproduzierbare Grundlage für die Erstellung präziser Magnetfeldkarten für C- und H-förmige Dipole sowie Quadrupole bietet. Das Framework verfügt über eine benutzerfreundliche Oberfläche, die es ermöglicht, Feldkarten ohne Programmierkenntnisse zu erstellen, wodurch schnelle und effiziente Simulationen ermöglicht werden. Dies standardisiert nicht nur den Prozess der Feldkartenerstellung, sondern gewährleistet auch eine einheitliche Modellierung über verschiedene Magnettypen hinweg.

Um Unsicherheiten im Bezug auf die Jochmaterialien zu minimieren und die Genauigkeit der Simulationen weiter zu verbessern, wurden zwei umfassende Materialstudien durchgeführt. Die erste Studie untersuchte das Magnetfeld innerhalb der Magnetapertur und identifizierte das am besten geeignete Material für jeden Magneten, indem simulierte Feldwerte mit Messdaten verglichen wurden. Die zweite Studie weitete die Analyse auf die gesamte Magnetgeometrie aus und bewertete die Sensitivität der Simulationen gegenüber Variationen der Jochmaterialien. Diese detaillierte Untersuchung ermöglichte eine fundierte Bewertung der Modellgenauigkeit sowohl im linearen als auch im Sättigungsbereich, um präzisere Feldberechnungen über einen breiten Betriebsbereich hinweg zu gewährleisten.

Die Ergebnisse dieser Arbeit führten zur Entwicklung neuer, hochpräziser Magnetfeldkarten sowie zur signifikanten Verbesserung bestehender Modelle. Durch die Etablierung einer robusten Methodik zur Feldkartenerstellung trägt diese Arbeit dazu bei, die Genauigkeit der Strahlsimulationen in der North Area zu verbessern. Dadurch wird letztlich die Optimierung experimenteller Aufbauten und die Qualität der wissenschaftlichen Daten am CERN unterstützt.

Schlagwörter: Magnete, North Area, Magnetfeldkarten, OPERA, OPERA2D, Python, Simulation, FEA

Abstract

This master's thesis focuses on the precise modeling of two-dimensional magnetic fields for the beamlines in the North Area (NA) at CERN. Accurate magnetic field maps are crucial for reliable beam simulations; however, for many magnets in the NA, such maps are either unavailable or lack sufficient precision. The main sources of these inaccuracies stem from uncertainties in the material properties of the magnet yokes and inconsistencies in the applied simulation methodologies. These factors can introduce significant errors in beam optics calculations, ultimately affecting the quality of experimental results.

To address this issue, a simulation-based framework was developed, providing a validated and reproducible approach for generating accurate magnetic field maps for C-shaped and H-shaped dipoles as well as quadrupoles. The framework features a user-friendly interface that enables researchers to generate field maps without requiring programming expertise, allowing for fast and efficient simulations. This approach not only standardizes the field-mapping process but also ensures consistency across different magnet types.

To further improve the accuracy of the simulations, two extensive material studies were conducted to minimize uncertainties related to the yoke materials. The first study focused on analyzing the magnetic field behavior within the magnet aperture, identifying the most suitable material for each magnet by comparing simulated field values with measured data. The second study expanded the scope to the entire magnet geometry, assessing the sensitivity of the simulations to variations in yoke materials. This comprehensive analysis allowed for a detailed evaluation of the model's reliability both in the linear and saturation regions, ensuring more precise field calculations across a wide range of operating conditions.

The results of this work led to the development of new, high-precision magnetic field maps as well as significant improvements to existing ones. By establishing a robust methodology for field map generation, this thesis contributes to enhancing the accuracy of beam simulations in the North Area, ultimately supporting the optimization of experimental setups and data quality at CERN.

Key words: magnets, North Area, magnetic fieldmaps, OPERA, OPERA2D, Python, simulation, FEA

Table of Contents

1 Introduction

1.1.1 Background and Motivation

The setup of beamlines in accelerator facilities, like those at CERN, involves several complex sub-systems that work together to guide and focus the particle beam with precision to the location of a fixed target or a collision experiment. Vacuum systems [1] maintain an almost airless environment, preventing collisions with air molecules that could weaken the beam while Beam Position Monitors (BPMs) [2] track the beam's position, ensuring it stays on the correct path. Beam profiling systems [3] analyze the shape and distribution of the beam, checking its quality, and collimators capture unwanted particles, protecting both the accelerator and detectors from scattered radiation. A very important and fundamental part of beamlines, however, are magnets. Magnets such as dipoles, quadrupoles, sextupoles and others play a crucial role in beamlines, where they are used to control the motion of charged particles, such as electrons or protons. Since charged particles respond to magnetic fields, magnets are essential for bending, focusing, and correcting the path of the particle beam. [4][5]

Among the different types of magnets used in beamlines, dipole magnets are used for bending the beam. These magnets create a uniform magnetic field, which applies a Lorentz force on the charged particles, causing their trajectory to bend. The extent of the bending depends on the velocity and charge of the particle and the strength of the magnetic field.[6] Dipole magnets are typically used to guide the particle beam on a circular path, as seen in circular accelerators like the Large Hadron Collider (LHC) or the Super Proton Synchrotron (SPS) but also to guide the beam along transfer lines (TL) for example in the North Area (NA) at CERN. Additionally, dipole magnets are used in momentum separation because particles with different momenta will experience different degrees of bending in the same magnetic field. The bending radius R of the particles is related to their momentum p, the magnetic field strength B, and their charge q by the equation

$$R = \frac{p}{qB} \tag{1}$$

This relation shows that higher magnetic field strengths or lower particle momenta result in tighter bending, which is crucial for guiding beams in circular paths. [6][7]

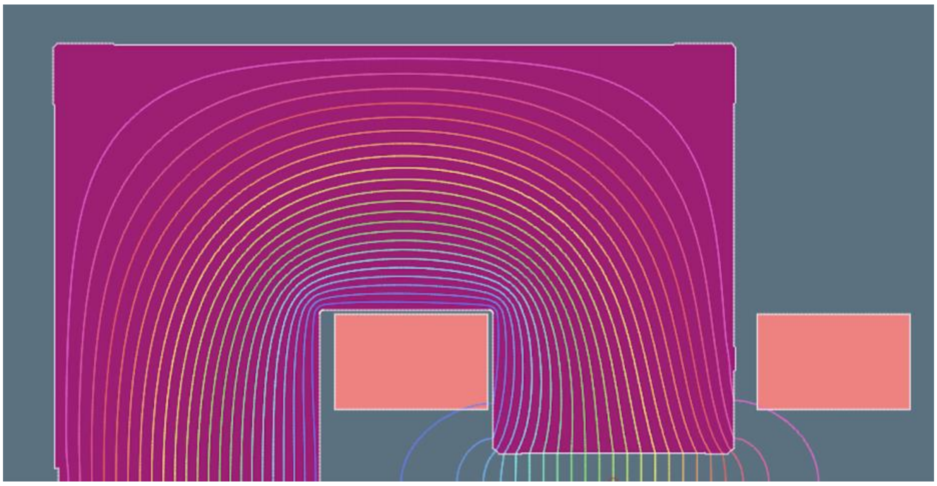

Figure 1: magnetic fieldlines in a dipole

Quadrupole magnets serve a different purpose. They are used to focus the particle beam, ensuring it remains narrow and controlled as it travels through the beamline. This is especially important in applications where beam quality must be maintained over long distances, such as in linear accelerators or large circular accelerators. [6][7] Unlike dipole magnets, which provide a uniform magnetic field, quadrupoles generate a magnetic field gradient, meaning the field strength increases with distance from the center. The magnetic field *B(x)* generated by a quadrupole magnet as a function of the position *x* can be described by

$$B(x) = G \cdot x \tag{2}$$

where G is the magnetic field gradient.
This results in a focusing effect in one direction and a defocusing effect in the perpendicular direction. To maintain overall beam focus, quadrupoles are often arranged in pairs or groups, such as in a FODO lattice. FODO is a magnetic structure which features alternating focusing and defocusing quadrupoles with minimal spacing between them. [8]

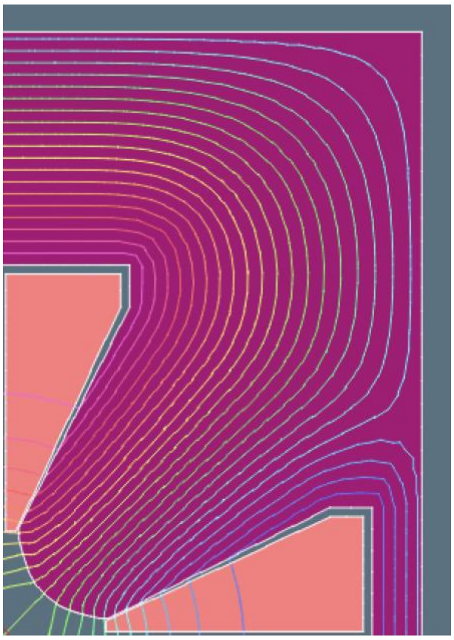

Figure 2: Magnetic fieldlines in a quadrupol

Beamline setups like these are not only found in large circular accelerators such as the LHC or the SPS, but also in beamlines that lead to fixed-target experiments. An example of this is the North Area at CERN, where particle beams are guided along specialized beamlines to hit fixed targets. Built in the 1970s, the North Area comprises six beamlines with a total length of over 6.3 km and three experimental halls with an area of approximately 31,000 m², supplemented by service buildings and underground tunnels. Over the past 50 years, the North Area has established itself as one of CERN's most intensively used experimental areas, thanks to the unique properties of its beamlines in terms of energy, particle type and flexibility. Currently, more than 560 beam guidance magnets of 40 different types are in operation in the North Area. [9]

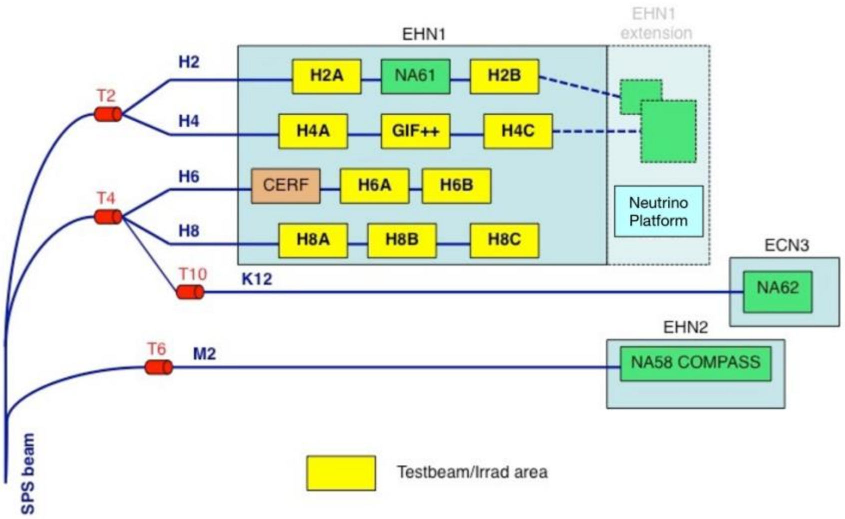

Figure 3: Schematic drawing of the transfer lines in the North Area at CERN[1]

At CERN, building a precise and functional beamline requires extensive simulations to ensure that the design will perform as expected before any physical components are installed. A key aspect of these simulations involves the use of magnetic field maps, which provide a highly detailed representation of the magnetic fields within the beamline magnets. These field maps are essential because they allow programs like BDSIM (Beam Delivery Simulation) [5][10] to accurately simulate the behavior of charged particles, such as protons or electrons, as they travel through the magnets. Instead of assuming that the magnetic fields are perfectly uniform—an approximation used in simplified models—field maps capture the real variations in the magnetic field, both in strength and direction, at different points in space. [11]

A magnetic field map is essentially a two- or three-dimensional grid, where each point (or node) contains information about the magnetic field components in the x, y (and z) directions (B_x, B_y, (and B_z)). These field values are generated either through detailed electromagnetic simulations of the magnets using software like OPERA [12] or ANSYS [13] or from experimental measurements of the actual magnet.

The use of field maps in BDSIM is necessary for several important reasons. First, they provide the accuracy needed to model complex magnetic regions that would otherwise be poorly represented by simpler models. Real-world magnets often exhibit non-linear behaviors due to factors like saturation, where the magnetic field no longer increases linearly with the applied current. Field maps capture these non-linearities, ensuring that the simulations reflect the actual conditions that particles will encounter.

Moreover, field maps are crucial for accounting for fringe fields, especially in the aperture region—the area through which the particle beam travels. In this region, the magnetic field must be known with high precision because even small discrepancies can lead to significant errors in the predicted path of the particles. The accuracy of the field map within this region directly influences the quality of the simulation, as it ensures that particles do not stray from their intended path, which could result in collisions with the beamline structure or other unintended consequences. [5]

The precision of these field maps is determined by the spatial resolution of the grid used to generate them. A finer grid, with closely spaced nodes, is necessary in regions where the

---

[1] https://cds.cern.ch/record/2651120/files/North-Area.png

magnetic field changes rapidly, such as near the edges of the magnet. This allows the simulation to capture small but important variations in the magnetic field.

Furthermore, it is important that they must not only provide detailed information about the magnetic field within the aperture, where the primary beam travels, but also about the magnetic field throughout the entire magnet geometry. This also includes regions outside the aperture. The extended field information is particularly crucial in fixed-target beamlines, where background particles can significantly affect experimental outcomes and equipment integrity. [14]

In a fixed-target beamline, a high-energy particle beam, is directed at a stationary target to generate secondary particles. These secondary particles, which can include a wide variety of particle types, are then used for experiments or further studies. However, the interaction of the primary beam with the target produces not only the desired secondary particle beam but also a substantial amount of background. In the context of particle accelerators and beamlines, background refers to particles or radiation that are not part of the primary beam but still exist in the system due to interactions with the beamline components, residual gas, or other environmental factors. These background particles can interfere with experimental measurements, reduce the precision of results, and potentially cause damage to equipment. Therefore, understanding and controlling these background sources is critical. [15] Pions, kaons, muons and neutrons are among the most commonly produced particles in such collisions, as well as high-energy photons from electromagnetic processes. [16] In addition, a significant number of electrons and positrons can be generated through electromagnetic showers, while protons and other heavy particles can be scattered from the target. These background particles can scatter in all directions, filling the beamline with unwanted radiation and noise, which can interfere with detector systems or damage sensitive equipment. [9]

In contrast to all other background particles, muons and neutrons are the only background particles that typically make it through the entire beamline setup after the fixed-target interaction. Muons are produced in large numbers from the decay of pions and kaons, but they are highly penetrating due to their relatively low interaction cross-section with matter compared to other particles. [17] While particles like protons, pions, and kaons will typically lose energy or be absorbed by the shielding and components along the beamline, muons—being much more weakly interacting—can pass through substantial layers of material. This makes muons a dominant component of the background that must be carefully considered, especially in areas of the beamline far from the target. [15]

The magnetic field outside the aperture is particularly important for simulating how background particles, including muons, might scatter or interact with the surrounding infrastructure. Even though most background particles are absorbed or deflected, field maps are used to predict where residual particles might travel and ensure that sufficient shielding is in place to protect detectors and equipment.

Muons feel the effects of magnetic fields because they are charged particles. As they pass through the beamline, the magnetic field can slightly alter their trajectory. This allows researchers to predict and check the paths of muons, ensuring the presence of muons is accounted for in background studies. [15][18]

Given all of this, it is clear that having precise magnetic field maps for every magnet in a beamline is absolutely crucial. Only with precise field maps can the interaction of the particle beam with the fields of the various magnets be properly represented. Furthermore, it is crucial that these field maps not only achieve the required accuracy but also be adaptable to varying operational scenarios, such as different field levels.

However, there is currently no existing simulation framework that adequately creates simulation models of the magnets in the North Area and generates their two-dimensional (2D) magnetic field maps. This thesis focuses on developing a simulation framework within the OPERA software that can efficiently and accurately simulate both dipoles and quadrupoles, regardless of their shape, and generate their corresponding field maps. The goal is to create a flexible code that can easily adapt to different magnet geometries, making it applicable to a wide range of magnet configurations while maintaining an intuitive and user-friendly design.

A 2D Finite Element Analysis (FEA) simulation was chosen, based on the geometric and operational characteristics of the accelerator magnets. The magnets have a length significantly greater than their cross-sectional dimensions, which allows for the assumption that the magnetic field within the aperture is uniform along the longitudinal axis. As a result, 2D simulations provide an accurate representation of the magnetic field distribution and offer greater computational efficiency compared to more complex 3D modeling approaches.

1.1.2 Problem Statement

The simulation of magnetic field maps for the magnets in the North Area has been carried out using various software tools, such as FEMM and OPERA. However, the creation of these field maps lacked a standardized and systematic approach. Instead, the simulations were conducted sporadically and independently by different members of personnel at different times. This fragmentation has led to significant uncertainties regarding the precision and reliability of the field maps generated, as well as their accuracy in reflecting actual operational conditions.

Beam physicists' current reliance on other team members to create magnetic field maps adds to these issues, creating inefficiencies and reducing the overall reliability of the simulation process. The lack of a centralized simulation framework that includes all necessary information further intensifies the problem, as it restricts accessibility and reduces consistency in the simulation outputs.

A standardized and systematic methodology for the computation of magnetic field maps is therefore needed in the North Area at CERN. This approach would reduce the dependency on individual experts and enable any team member to generate accurate field maps efficiently.

1.1.3 Scope of the Work

This thesis aims to develop a comprehensive and standardized framework for simulating two-dimensional magnetic field maps for all dipoles and quadrupoles in the North Area. The primary objective is to create a simulation code in an OPERA-specific version of Python that operates independently of specific magnet geometries. Magnet-specific parameters such as the geometry, material, and number of windings will be compiled in an external *Input file*. Such Input files are created for every magnet separately and provided to the code when needed. This design ensures flexibility across various magnet configurations while maintaining user-friendliness.

Key features of the code developed include an intuitive user interface, making it accessible to users without a background in FEA or programming. To further enhance usability, critical parameters which influence the simulation outcomes are predefined or restricted within acceptable ranges. This minimizes the risk of user error while allowing for necessary adjustments.

The code also incorporates the ability to iterate over a list of input current values and calculate corresponding field maps. This functionality is essential for simulating magnetic field behavior under different operational conditions.

Validation of the developed simulation code is then performed through comparison with experimental data obtained from existing CERN documentation. This step is crucial to confirm that the simulation model accurately reflects the real-world behavior of the magnets, yielding reliable and precise results.

Additionally, the thesis includes two in-depth material studies. The first study aims to identify the best-fit yoke material for the magnets, while the second evaluates the impact of different materials on the magnetic field simulations. Based on this assessment, it determines whether the magnet model is sensitive to changes in material properties.

Finally, the reliability and accuracy of the models developed will be evaluated, based on the availability of the needed documentation and the sensitivity of the magnet to material changes.

1.1.4 Overview of the methodology

This master's thesis is structured into four main sections, each focusing on a specific aspect of the development and validation of the simulation framework for 2D magnetic field simulations.

The first section provides a comprehensive discussion of the theoretical background which is necessary for understanding the following chapters. The theoretical background provides an overview of the composition of accelerator magnets, an explanation of the procedure for creating a simulation model in OPERA2D, and a review of the key physical phenomena that play a role in magnetic field behavior.

Following this, the general structure and functionality of the simulation code implemented in this thesis is thoroughly explained. This includes a description of the algorithmic framework and the specific features of the software. Additionally, the construction and formatting of the Input files required for the simulations are outlined.

To ensure clarity, the validation method for dipoles as well as quadrupoles used in the work is explained. This validation process is critical to confirm the reliability and accuracy of the simulation framework in simulating magnetic field distributions under various conditions.

The second section presents an attempt to identify the magnet material through chemical analysis of both the magnet material and a steel sample, comparing them to determine if they originate from the same batch. If confirmed, BH curve measurements could then be performed on the steel samples. The organisation by magnet families was intended to serve as an initial grouping, after which two methods – X-ray Fluorescence (XRF) and Optical Emission Spectroscopy (OES) – were considered to determine the chemical composition of the magnets. However, due to the high complexity and limited resources available for this work, this approach was not pursued further.

The third section contains two detailed material studies that thoroughly examine how different materials used for yokes affect the simulation of the magnetic field within the magnet geometry. The first study focuses on the region within the aperture of the magnet and aims to find the best-fit material for each magnet model. This is achieved by comparing the simulated and measured BI curves of the respective magnets. A BI curve is a curve that represents the relationship between the magnetic field [B] and the current [I] applied to the magnet.

In the second study, for every simulation model, the magnetic field distributions for various materials were simulated and subsequently compared. By analyzing these differences, it was possible to determine whether the individual simulation models are sensitive to variations in the yoke material, both within the linear operating range and in the saturation region.

The fourth section covers the reliability statement, which serves to evaluate each magnet simulation model in terms of uncertainties and potential sources of error. Various factors are considered, including inaccuracies in the geometry, the accuracy of the magnetic measurements, the agreement between the simulated and measured BI curves, as well as the sensitivity to material changes in the simulation. Based on these factors, an overall uncertainty value is determined and provided for each magnet.

1.2 Theoretical Background

1.2.1 Composition of an Accelerator Magnet

The structure of an accelerator magnet is a complex assembly designed to guide and control charged particle beams in particle accelerators. Each component plays a vital role in the generation and management of the magnetic field, which is essential for beam manipulation.

At the core of the magnet is the yoke, which can be constructed as a single solid block or as laminated sheets, also called *lamelles*. The magnets referred to in this work are manufactured with laminated yokes. These yokes consist of thin layers of magnetic material, stacked together to minimize eddy currents that can occur when exposed to varying magnetic fields. [19]

The coils of the magnet are crucial for generating the magnetic field. When an electrical current flows through the coils, a magnetic field is produced, with the strength and shape determined by the coil configuration and the intensity of the current. The design of the coils, including the number of turns and their arrangement, allows for tailoring the magnetic field to meet specific operational requirements, such as bending or focusing the particle beam. These coils are constructed from copper. [6]

The aperture is a central feature of an accelerator magnet, typically a cylindrical or rectangular space surrounded by a vacuum chamber made from non-magnetic materials like stainless steel or aluminium. This aperture is the pathway through which the particle beam travels, and its design is critical for ensuring that the magnetic field within it is uniform and properly shaped to achieve the desired trajectory for the beam.

The Good Field Region (GFR) refers to the spatial region within the aperture of a magnet where the magnetic field strength remains within an acceptable tolerance. This region is crucial for ensuring that the magnetic field is uniform and stable, which is essential for a properly operating beamline. [7]

Supporting the structural elements of the magnet are the tension plates and tie plates. Both are constructed from high-strength, non-magnetic materials, such as stainless steel. Tension plates provide essential structural support. They maintain the alignment of the coils and yoke, preventing mechanical deformation that could misalign the magnetic field. Tie plates serve to connect various magnet components, helping to distribute mechanical forces throughout the structure, which is crucial for maintaining precise alignment during operation.

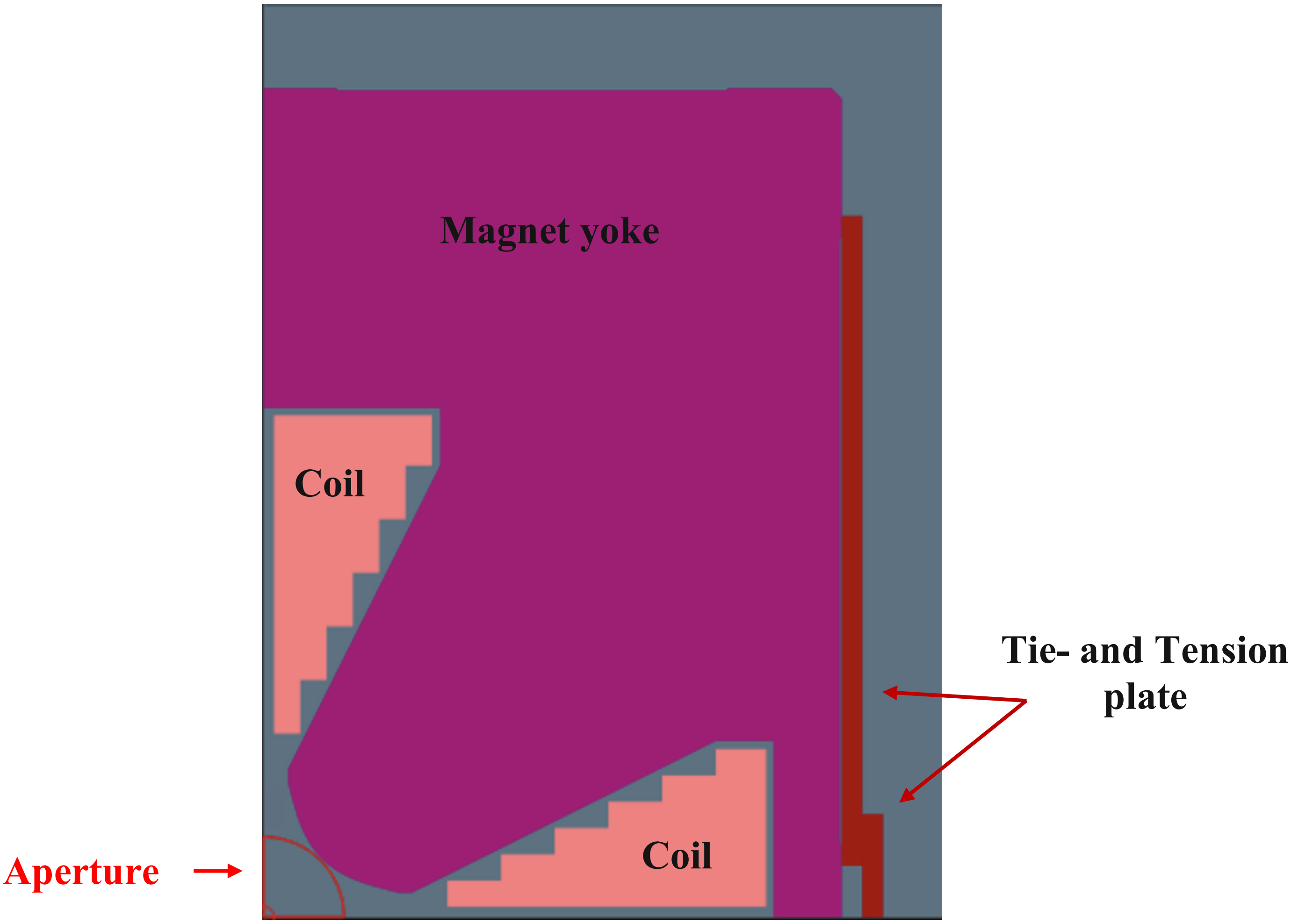

Figure 4: All important magnet model components, illustrated by the quadrupole QNL

2 Code developement

2.1.1 Procedure for creating a Simulation Model

To create an accurate magnet simulation model in OPERA2D, several steps are necessary, which will be explained below to ensure understanding of the subsequent code description.

The first step in creating a simulation model in OPERA2D is to define the geometry of the magnet in question. This means that all components of the magnet relevant to the magnetic simulation must be modeled as accurately as possible. This is crucial for carrying out a meaningful simulation. The components that constitute the geometry of the magnet in the simulation model include the magnet's yoke, the coils, and other parts such as tension plates that could influence the magnetic field in any way. Additionally, the air gaps between individual components must be defined as such.
After the geometry is created, the symmetry, element types, and material properties are defined. The choice of symmetry is crucial for improving the efficiency of the calculations. The symmetry reduces the number of elements to be computed, thus minimizing computational effort by reducing the problem size and avoiding redundant calculations.
In OPERA2D, there are two main types of symmetry: Cartesian and axisymmetric (rotational) symmetry. Cartesian symmetry is used when the problem can be represented in a rectangular (Cartesian) coordinate system. This is ideal for geometries that are symmetric along the axes, like the magnets modeled in this work. The advantage of Cartesian symmetry lies in simplifying calculations by mirroring results across symmetry axes.

The choice of element types is also crucial for enhancing both the efficiency and accuracy of the calculations and directly affects the required computation time.
In OPERA2D, two primary types of elements are commonly used: linear (low-order) and quadratic (higher-order) elements. Linear elements only have nodes at the corners of the elements, while quadratic elements include additional nodes at the midpoints of the element sides, in addition to the corner nodes. The use of quadratic elements enables quadratic interpolation, which improves accuracy and leads to better convergence properties compared to linear interpolation, even with a similarly fine mesh. However, this comes at the cost of increased computational effort, resulting in longer computation times and greater memory requirements. [20]

In addition to selecting the appropriate element types for accurate calculations, the choice of the material also plays an important role in the overall performance of the simulations. OPERA2D offers a big material database, with a wide range of different materials. These predefined materials can be directly used as magnetic materials in the simulations. However, if the database does not include a specific material that is required, it can be expanded with custom user-defined materials.

In OPERA, materials can be distinguished based on their permeability characteristics as either having linear or non-linear permeability. Linear materials, like air, exhibit a constant permeability μ, resulting in a straight-line BH curve, where the magnetic flux density $\vec{B}$ is directly proportional to the magnetic field strength $\vec{H}$, as described by the equation:

$$\vec{B} = \mu \cdot \vec{H} \tag{3}$$

whereas non-linear materials display variable permeability μ, leading to a curved or complex BH curve that reflects changes in magnetic properties with varying field strength. This is typical for ferromagnetic materials like those used in magnetic yokes. In such cases, permeability decreases with increasing magnetic field and eventually reaches saturation.
When defining a new material in OPERA, the BH curve of the respective material is added by specifying the magnetic flux density (B) as a function of the magnetic field strength (H), typically using a table of data points that captures the non-linear hysteretic behavior of the material under varying magnetic field conditions. [21]

The next step involves defining the boundary conditions and excitations.
In FEA, boundary conditions play a vital role in accurately modeling physical systems, as they define the behavior of field variables at the edges of the computational domain. There are two primary types of boundary conditions used in the simulations: Dirichlet and Neumann boundary conditions.

Dirichlet boundary conditions specify the exact value of a field variable, such as the magnetic field, at the boundaries of the domain. In magnetic field simulations, Dirichlet conditions are often applied to surfaces where the field is known or can be assumed to be constant, such as the surface of a magnet or at the interface between different materials. These conditions are utilized when the precise value of the field at the boundary is determined by material properties or external influences. [22]

Neumann boundary conditions, on the other hand, specify the derivative of the field variable normal to the boundary, typically representing the flux across that boundary. For magnetic field problems, Neumann conditions are applied along symmetry axes or at boundaries with free space, where there are no sources or sinks of the field. These conditions imply that there is no change in the field normal to the boundary, making them ideal for simulating regions without magnetization or material influence. [23]

Once the geometry of the individual components has been determined and their properties are defined, the meshing process can begin.
Meshing is a critical step in FEA. In this process, the continuous geometry is divided into small, discrete elements via the Finite Elements Method (FEM) to enable the numerical solution of Maxwell's equations. [24] OPERA offers both automatic and manual methods for generating an appropriate mesh. A finer mesh typically results in more accurate outcomes but requires greater computational power and time. Therefore, a balanced approach must be found between mesh refinement and the available computational resources.
Once the mesh has been created with the required level of accuracy, field quantities are automatically calculated after the simulation has started.

When the calculation is complete, the results can and should be analyzed in the post-processing phase. OPERA provides a variation of tools for visualizing and evaluating the magnetic fields, such as the display of field lines, flux densities, and potential distributions.
The analysis should also include verifying the plausibility of the results and assessing whether the simulation meets the defined requirements. This is done via validation, which involves comparing the simulation results with experimental data or theoretical expectations and ensures that the carried-out simulation is accurate and reliable.

2.1.2 Influence of different Materials on the Magnetic Field

When an electric current flows through a coil surrounding a magnetic material, it generates a magnetic field $\vec{H}$. The magnetization $\vec{M}$ of the material is a result of this magnetic field.
Magnetization $\vec{M}$is the material's magnetic response to the applied magnetic field and is proportional to $\vec{H}$:

$$\vec{M} = \chi_m * \vec{H} \tag{4}$$

where χ_m represents the magnetic susceptibility of the material.

In the *linear region*, the magnetization increases proportionally to the applied field $\vec{H}$, and the relationship between the magnetic flux density $\vec{B}$, the applied field $\vec{H}$, and the magnetization $\vec{M}$ is given by:

$$\vec{B} = \mu_0 * \left(\vec{H} + \vec{M}\right) = \mu_0 * (1 + \chi_m) * \vec{H} = \mu * \vec{H} \tag{5}$$

Here μ_0 is the permeability of free space, and $\mu = \mu_0 * (1 + \chi_m)$ represents the permeability of the material, which depends on the susceptibility. [25]
In this region, the domains within the material start to align with the magnetic field that is applied, leading to a linear increase in both $\vec{M}$ and $\vec{B}$.
As the field strength continues to rise, the material enters the *saturation region*. Here, the rate of increase in magnetization starts to slow down. Initially, the magnetization increases rapidly as the domains rotate into alignment with the field, but as more domains align, fewer remain that can still be magnetized. This causes the rate of increase of $\vec{M}$ to decrease, and the relationship between $\vec{M}$ and $\vec{H}$ becomes non-linear. The material's magnetization is still growing, but at a slower rate and, eventually, the material reaches its saturation point, where nearly all the domains are fully aligned with the field. [26]
At this stage, the magnetization $\vec{M}$ reaches its maximum value $\vec{M}_{Sat}$

$$\vec{M} \approx \vec{M}_{Sat} \tag{6}$$

and further increases in the applied field $\vec{H}$ result in very little change in $\vec{M}$. The magnetic flux density $\vec{B}$ continues to rise, but primarily due to the external field, as the contribution from the magnetization becomes negligible.
The magnetic flux density $\vec{B}$ then approaches:

$$\vec{B} \approx \mu_0 \cdot \vec{H} + \mu_0 \cdot \vec{M}_{Sat} \approx \mu_0 \cdot \vec{H} + \mu_0 \cdot \vec{M}_{Sat} \tag{7}$$

This behavior signifies the material's inability to respond further to the applied field due to the near-complete alignment of its domains. As the magnetic field $\vec{H}$ increases beyond saturation, the flux density $\vec{B}$ increases linearly with $\vec{H}$, as the contribution of $\vec{M}$ no longer increases.
Thus, in the saturation region, the material's magnetization has reached its maximum, and the magnetic susceptibility χ_m effectively decreases, making the material's response to the external field less pronounced. The flux density continues to grow, but only due to the increasing external field, as the material has become magnetically saturated. [27][28]

When the magnetic field $\vec{B}$ is calculated over a range of currents $[0, I_{max}]$ the resulting magnetic field in the magnetic material changes. In this context, the permeability of the respective material plays a crucial role. Materials with higher permeability are more capable of aligning their magnetic domains in response to an applied magnetic field, allowing them to achieve higher levels of magnetization at lower field strengths. Conversely, materials with lower permeability require a stronger external field to reach the same level of magnetization. As a result, when materials with different permeabilities are subjected to the same external magnetic field or current, they will exhibit distinct behaviors. [29][30]
Therefore, it is essential to assign the correct material to a simulation model. Ensuring that the right material properties are used guarantees reliable and accurate results, as the material's magnetic characteristics directly influence the simulation's outcome.

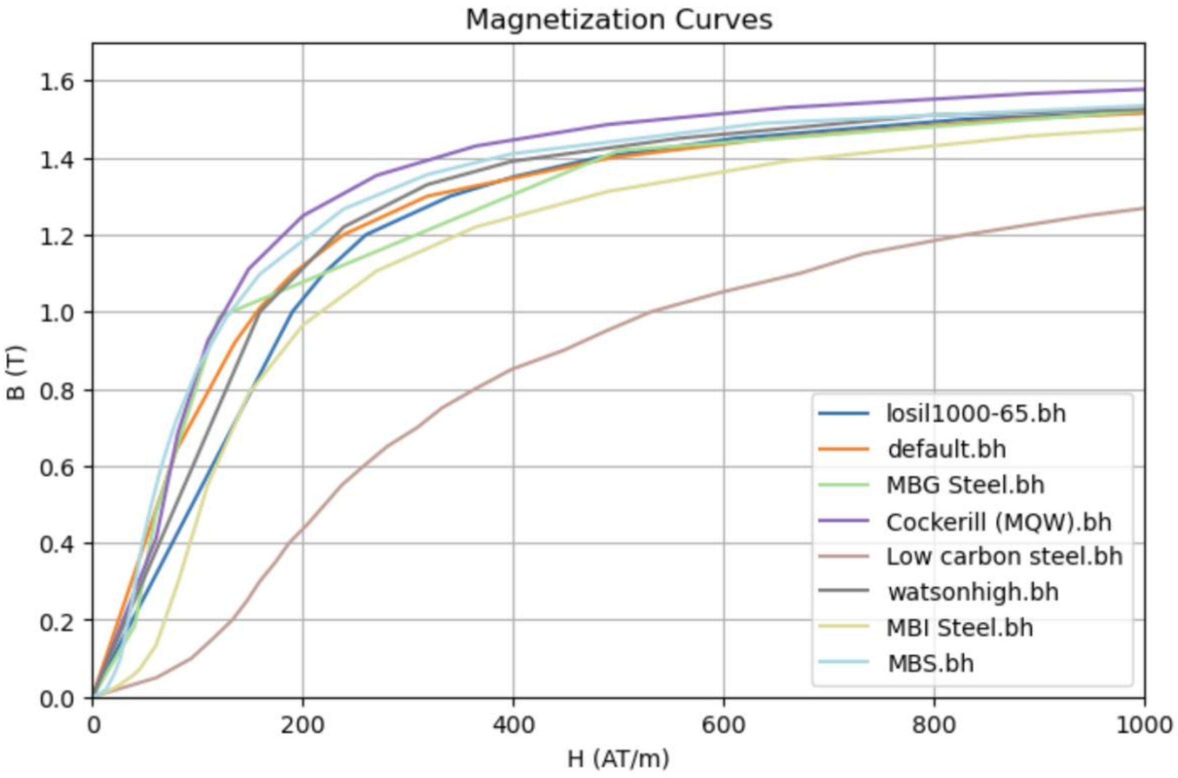

Figure 5: Magnetization and field intensity curves of the magnetic materials observed in this work

Table 1 lists all the magnetic core materials that were used and compared in the course of this work. The materials and their respective BH-curve values are listed in **Appendix A**.

Materials
Cockerill (MQW).bh
default.bh
losil1000-65.bh
Low carbon steel.bh
MBG steel.bh
MBI Steel.bh
MBS.bh
watsonhigh.bh

Table 1: List of all magnetic material observed in this work

2.2 Methodology

2.2.1 Special Structure of the Code

The finite element simulation program OPERA offers two programming languages for carrying out 2D simulations: COMI and an internal version of Python. For the present work, OPERA's internal version of Python was used. This decision was based on several factors, including Python's flexibility and user-friendliness, which allows for the efficient design and management of complex simulations, as well as the ability to create the Input files using Python.

In this context, "OPERA-internal" means that while the programming language is based on Python, it includes specific functions that cannot be executed in a standard Python environment such as Spyder [31] or JupyterLab [32]. These specialized functions are exclusively available within the designated user interface of OPERA2D.

2.2.1.1 Symmetry

All the magnets considered in this work are Cartesian. When simulating Cartesian dipoles and quadrupoles of this kind, it is sufficient to model only half (for C-shaped dipoles) or one-quarter (for H-shaped dipoles and quadrupoles) of the system due to the symmetry properties of the magnetic fields. This symmetry significantly reduces the computational load, as fewer geometric data needs to be processed, allowing the calculations to be performed more quickly and efficiently.

A C-shaped magnet features a semi-circular or arc-like shape, causing the field lines to follow a distinct curvature based on the magnet's geometry. By modeling only half of the magnet, boundary conditions can be applied that use this symmetry.

Neumann boundary conditions were applied along the symmetry axis, in this case the x-axis. These conditions specify that the normal derivative of the magnetic field is zero, which means there is no change in magnetic flux density along the symmetry line. The field remains constant in the direction perpendicular to the axis of symmetry. Conversely, Dirichlet boundary conditions were applied at the outer boundary of the modeled region—representing a transition to the air surrounding the magnet. The chosen symmetry and the applied boundary conditions can be seen in Figure 6.

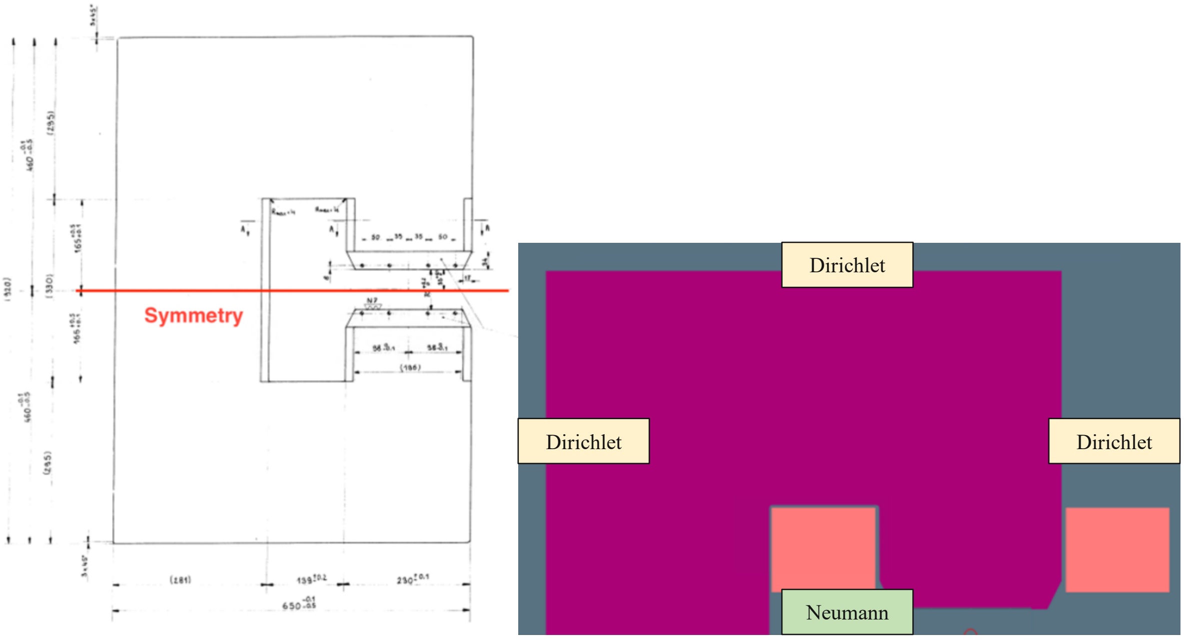

Figure 6: Left: component drawing of the cross section of a C-shaped dipole (MCW magnet) with marked x-symmetry, Right: simulation model in OPERA2D with the defined boundary conditions

The H-shaped dipole consists of two vertical legs connected by a central crossbar, resembling the letter H. In the case of the H-shaped dipole, which was only modeled to a quarter, a careful selection of boundary conditions was crucial to accurately represent the magnetic field behavior at the edges of the model. Along the vertical symmetry axis (the y-axis), *Dirichlet* boundary conditions were applied. This is because the magnetic flux lines in the H-shaped dipole typically emerge from one pole and curve through space toward the other pole, creating a pattern where the field values at the y-axis are defined. *Dirichlet* boundary conditions were also applied at the outer boundary region, where a transition occurs from the magnet to the surrounding air. In contrast, along the horizontal symmetry axis (the x-axis), *Neumann* boundary conditions were applied.

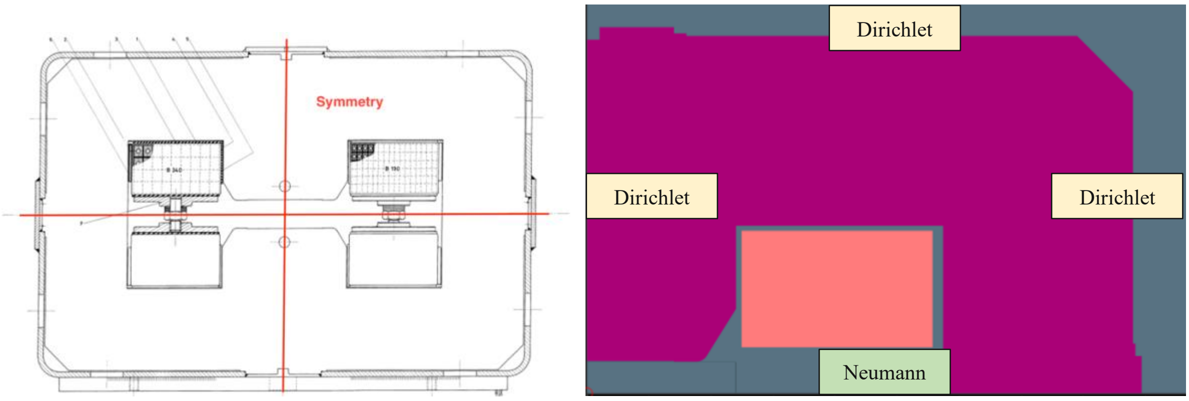

Figure 7: Left: component drawing of the cross section of an H-shaped dipole (MAL magnet) with marked x- and y-symmetry, Right: simulation model in OPERA2D with the defined boundary conditions

The quadrupole magnets simulated in this work consist of four poles arranged symmetrically. *Neumann* boundary conditions were applied along the symmetry axes (the x-axis and y-axis). On the surfaces of the magnetic poles, where the material interfaces with air, again, *Dirichlet* boundary conditions were employed.

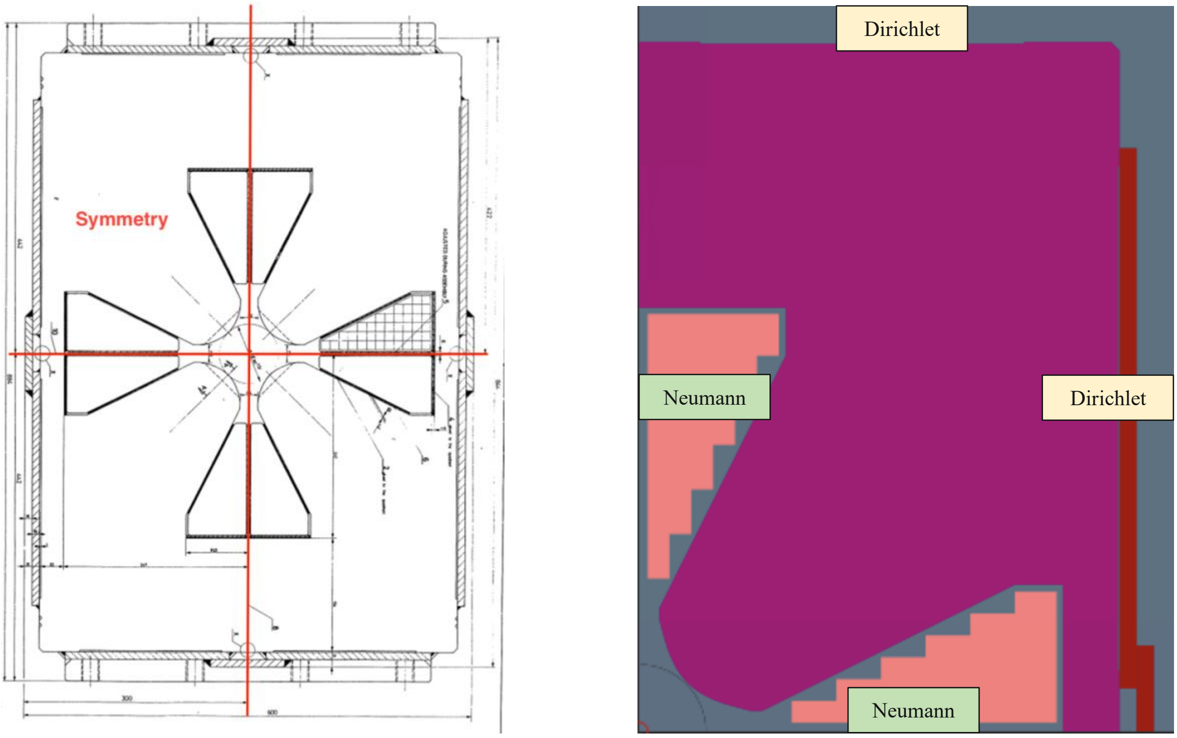

Figure 8: Left: component drawing of the cross section of a quadrupole (QNL magnet) with marked x- and y-symmetry, Right: simulation model in OPERA2D with the defined boundary conditions

2.2.1.2 Changeable Parameters

In this work, special attention was given to designing the simulation code in a way that is both simple and effective. A key objective was to minimize the number of adjustable parameters. This approach not only made the code easier to use but also helped to prevent unintended changes by different users that could affect the field maps calculated.

As a result the modifiable parameters were divided into two subgroups based on the level of expertise required to change them.

2.2.1.2.1 Actions to be done on the Model by Normal Users

The following parameters can be modified by all users, even without prior knowledge of magnets or FEA simulations, and are sufficient for a basic magnet simulation. This means that just by adjusting these parameters, all magnets in the North Area can be simulated at different field levels (generated by entering various current values), and their field map, field line plot, colorplot, and other results can be calculated. In Table 2 all adjustable parameters are listed, accompanied by a brief description of each.

Parameters accessible to the user		
list_currents	A list of currents for which the whole field map is calculated	list
points_list	Coordinate points where the magnetic field is calculated, e.g. for the functions FieldInPoint_txt and FieldInPoint	Tuple, list of tuples
author	The name of the author	string
magnet	The accurate name of the magnet to be modelled.	string

Table 2: Parameters that can be changed by normal users to execute the magnet simulations

This simulation code is specifically designed to calculate the field maps for various magnets at different currents. This means that by executing the code once, field maps can be calculated for an arbitrary number of currents. To do this, all currents for which the field map should be calculated must be entered in the list named *list_currents*.

2.2.1.2.2 Actions to be done on the Model by Advanced Users

The following parameters should only be adjusted by individuals who fully understand how changes could affect the magnetic field simulation.

Parameter	**Function**	**Input**
globalmesh	factor that will be multiplied with all values of mesh size • if <1, mesh = more dense • if >1, mesh = less dense	integer
meshvalue_coil	factor that will be multiplied with all values for the YOKE • if <1, mesh = more dense • if >1, mesh = less dense	integer
meshvalue_yoke	factor that will be multiplied with all values for the COILS • if <1, mesh = more dense • if >1, mesh = less dense	integer
mesh_value_air_close	factor that will be multiplied with all mesh values for the background region that is closest to the magnet *magnet_edges* • if <1, mesh = more dense • if >1, mesh = less dense	integer
gridsize_x	defines the distance of points in x in the readout grid for the field map (grid resolution)	integer
gridsize_y	defines the distance of points in y in the readout grid for the field map (grid resolution)	integer
background_size_factor	Creates the outermost background	integer
reduced_background_size_factor	Creates the middle background	integer
magnet_edges_size_factor	Creates the background which is closest to the magnet model → magnet_edges	integer

Table 3: Parameters that should only be changed by experienced users

The size of the field map is defined by a background region which splits up in three different parts and is automatically calculated for every magnet model. The outermost background region defines the overall size of the field map and is calculated by taking the x values of the left- and right-most coordinate value and the y value of the highest coordinate value of a given magnet geometry and multiplies it with a factor of 1.5. This ensures that the background adjusts its size according to the size of the given model and always exceeds the magnet geometry in size. The middle and smallest background regions are created the exact same way but are multiplied with a factor of 1.3 and 1.1 respectively. The reason for creating three regions instead of one big background region is a different mesh density. In the outermost background region, the mesh is the biggest and gradually gets finer when coming to the innermost background region, where it is almost as fine as the mesh in the yoke and the coils. This ensures the reduction of unwanted calculation time as there is no unnecessary fine mesh in areas where there is almost no field.

2.2.2 Postprocessing tools

The parameters shown in Figure 9 represent all the available simulation functions that can be executed with this code. A brief explanation of each of these simulation functions is provided in Table 4. To execute a desired function, the corresponding value must be changed from *False* to *True*.

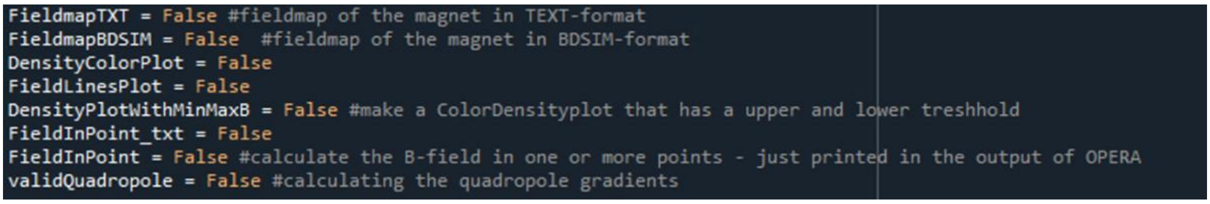

```
FieldmapTXT = False #fieldmap of the magnet in TEXT-format
FieldmapBDSIM = False  #fieldmap of the magnet in BDSIM-format
DensityColorPlot = False
FieldLinesPlot = False
DensityPlotWithMinMaxB = False #make a ColorDensityplot that has a upper and lower treshhold
FieldInPoint_txt = False
FieldInPoint = False #calculate the B-field in one or more points - just printed in the output of OPERA
validQuadropole = False #calculating the quadropole gradients
```

Figure 9: All post-processing functionalities implemented in the simulation code

Function	**Short description**
FieldmapTXT	Calculates the field map of a magnet in .txt format
FieldmapBDSIM	Calculates the field map of a magnet in BDSIM format
DensityColorPlot	Calculates a colormap of the magnetic field. • Bx – B-field in x-direction • By – B-field in y-direction • B – general B field • POT – Potential Defaults to B!
FieldLinesPlot	Calculates and generates a field line plot • Bx – B-field in x-direction • By – B-field in y-direction • B – general B field • POT – Potential Defaults to B! res_linesplot → number of lines to be drawn
DensityPlotWithMinMaxB	Calculates a colormap of the magnetic field between an upper and lower B threshold, which can be freely selected. To do this, the values highlighted in green must be modified. • minB_colorplot: minimal B • maxB_colorplot: maximal B
FieldInPoint_txt	Calculates the magnetic field at one or more specified coordinate points and saves the results in a .txt file
FieldInPoint	Calculates the magnetic field at one or more specified coordinate points and outputs the results exclusively in OPERA (console)
Quadropole_gradient	Calculates the gradient in the aperture of a quadrupole **Note:** This function is only applicable to quadrupoles!

Table 4: All simulation functions of the simulation code and a short description of each

2.2.3 Special and optimized structure of the code

To keep the code as simple and as universal as possible, magnet-specific data was generally not integrated directly into the simulation code during its implementation. This means that the code itself does not contain any data related to the specific details of individual magnets like the geometry and material of the yoke or the number of windings in the coils.

In this simulation framework, two files work together to manage and process the magnet simulation parameters. The first file, known as the Input file, defines a dictionary that organizes the various magnet-specific parameters. This dictionary consists of key-value pairs, where each key represents a specific parameter—such as geometry, windings, or material—and each value contains the corresponding numerical data or descriptive information. The exact structure and format of these Input files are decribed in chapter 2.2.4.

The second file is the main simulation code, and it is responsible for performing the computational tasks. It retrieves the necessary parameter values from the dictionary defined in the Input file. To achieve this, the main simulation code dynamically loads the Input file during execution. Once loaded, it accesses the required values by referencing the relevant keys in the dictionary.

As the main simulation code runs, it systematically pulls data like the geometry, symmetry, or the magnet material from the dictionary, integrating these values into the simulation functions and formulas. This ensures that all essential parameters are readily available for accurate simulation and field map calculations.

This method allows for easy updates and flexibility. If a parameter needs adjustment—such as changing the number of windings or the yoke material—it can be modified directly in the Input file without altering the main simulation code. This separation of parameter definition and computation ensures modularity, making it easier to maintain and update the files independently. Additionally, it simplifies managing multiple simulations with different magnet configurations, as only the Input file needs to be adjusted for new parameter sets, while the main simulation code remains unchanged.

However, despite these benefits, the calculation of field maps can still be very time-consuming. The time needed to generate a field map depends on various factors, such as the geometric complexity, the mesh density, and the choice of element types. When running the code through a list of currents without optimization, the entire geometry of the magnet is recreated and recalculated for each current value. This results in unnecessarily high computational and memory demands, significantly reducing the efficiency of the code.

To optimize the code's efficiency in terms of computation time, a specific optimization approach was adopted in this work. The chosen optimization strategy is based on integrating only the current-dependent parts of the simulation code into the loop over the current values. This means that the geometry of the magnet, the coils, the components, and the background are created only once. Similarly, assigning the specified materials to the respective components, selecting symmetry and element types, and defining the boundary conditions for all components are also done just once. These steps remain constant for all current values and serve as the basis for the calculations.

Within the loop for the different current values, only the current-specific calculations are performed. These include calculating the current density in the coils, generating the mesh, solving the model, calculating the field map, and performing post-processing. This optimization significantly reduced computation time by avoiding redundant steps and repeatedly executing only the current-dependent parts of the code. This means that the simulations for generating the field map of a magnet take between one second and a maximum of two minutes, depending on the size of the magnet.

2.2.4 Creation of the Input Files

As described in the previous chapter, the simulation code is designed to be magnet-independent, with all relevant information for each magnet externalized into the Input file. Consequently, a separate input file has been created for each magnet to be simulated.

2.2.4.1 Extraction of Geometries from Documentation

One of the main challenges in creating the simulation models was to replicate the real geometry of the magnets as accurately as possible within the OPERA simulation software. Achieving this level of precision required a thorough review of older documentation from the archives. Most of these documents date back to the 1960s and 1970s, which significantly complicated the search for detailed component and general assembly drawings. In many cases, it was difficult or even impossible to find complete and accurate drawings of the individual components.

For precise modeling, it was necessary to use the cross-section drawings of the magnet yoke and coils, as well as the component drawings of the tie and tension plates, if needed.

Figure 10 presents the cross-sectional drawing of the upper half of the magnet yoke for the MAL magnet. This drawing was utilized to generate the point list for the magnet yoke geometry of the MAL simulation model in OPERA and serves as a representative example for all the magnet geometries modeled in this study.

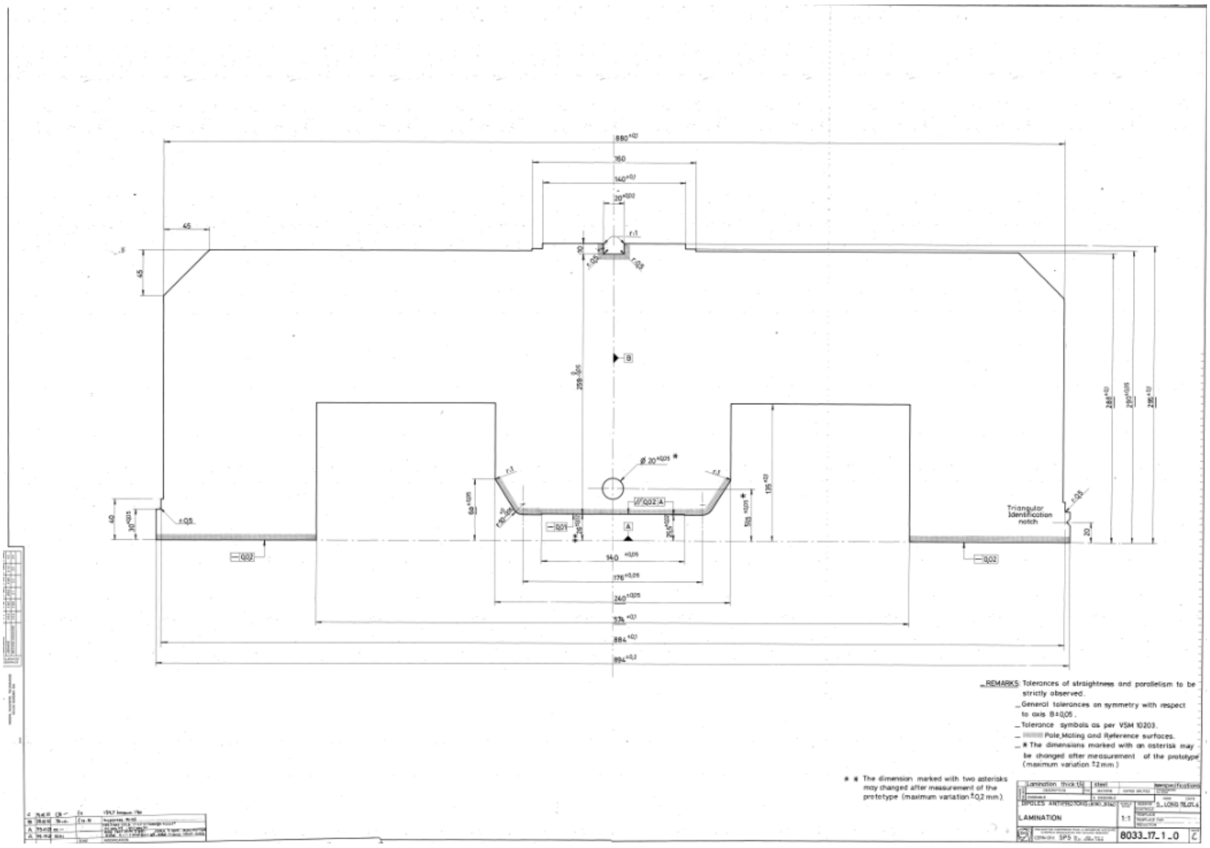

Figure 10: Lamination drawing of the cross section of the upper half of the MAL magnet

2.2.4.2 Structure of the Input file

The structure of the Input file is identical for every magnet and is defined by a single dictionary which consists of the following entries:

Symmetry: a central parameter that specifies whether the magnet is a C-shaped or H-shaped dipole, or a quadrupole. This symmetry information is crucial for the correct modeling of the magnet's structure.

- 'reflectxydipole' – H-shaped dipole
- 'reflectxzdipole' – C-shaped dipole
- 'reflectxyquadrupole' – Quadrupole

Objects: In addition to symmetry, the dictionary also contains a list called *Objects*. This list contains the complete data for the individual components of the magnet. For each component (such as the yoke, coils, and covers), there is a separate dictionary within Objects, which stores the relevant information about the components as key-value pairs.

An overview of the structure of the Input files and the main simulation code is presented in Figure 11.

A dedicated code was also developed for creating the input files, which includes predefined functions to facilitate the calculation of coordinates for features such as rounded corners and hyperbolas. These functions were specifically designed to capture and model the geometric details of the magnets with precision, thus making the process of generating input files for new magnets easier. After the coordinates are calculated, the generated input files are saved in the correct format and appropriate folder, allowing them to be used directly as input for the OPERA2D simulation.

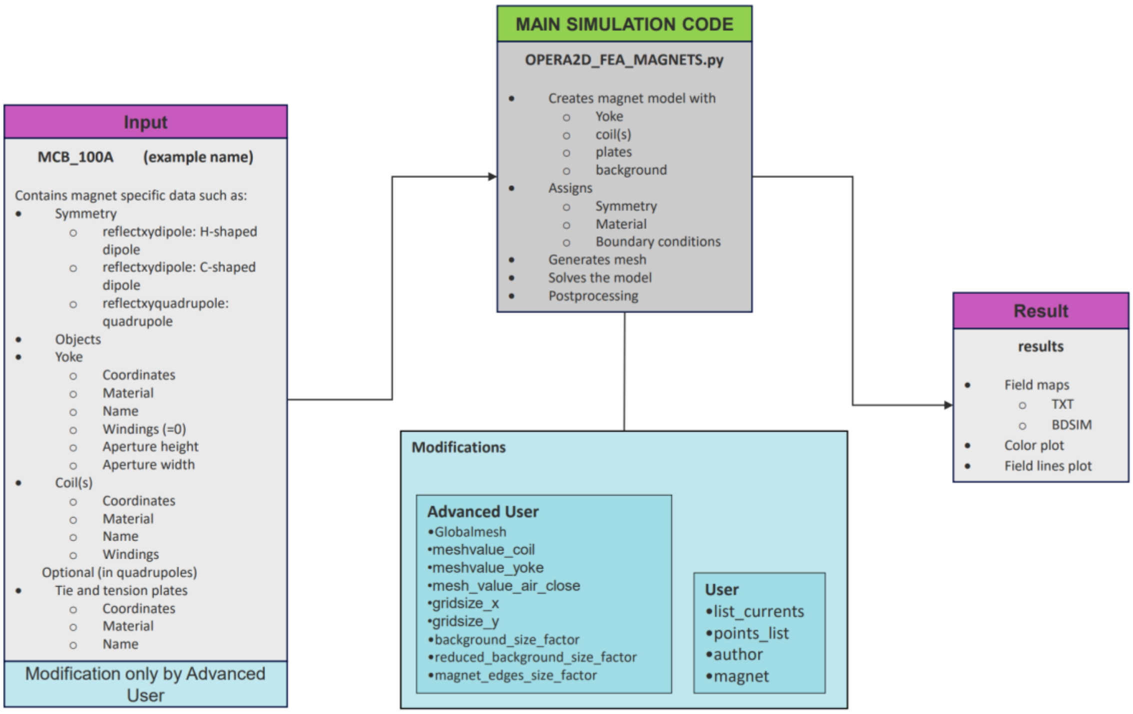

Figure 11: Structure and connection of the Input file and the main simulation code

2.2.5 Validation of the Simulation Code

For the validation of the simulation models developed in this master's thesis, a method was used that analyzes the simulated BI curves in comparison to the corresponding experimentally measured BI curves for each magnet. By comparing these curves, potential differences between the simulated results and the actual measurements could be identified and examined. Any deviations between the two curves may indicate inaccuracies in the model calculations or the input data, like the geometry of the magnets or the number of windings. Achieving a precise match between the experimentally measured BI curves and the simulated curves was essential for the successful validation of the code developed in this work. Such a match indicates the reliability and accuracy of the simulation process and confirms the correctness of the underlying models and the selected parameters. This validation ensures that the code can produce realistic and meaningful results, which can be utilized for future simulations of the beamlines. Given that the calculation of the BI curves for dipoles and quadrupoles is based on different methods, separate approaches were chosen for the validation of the dipoles and quadrupoles.

2.2.5.1 Validation of the Dipole Models

The approach for validating the dipole models involved calculating the magnetic field at the center of the aperture, specifically at the coordinate point (0,0), for the simulation. To ensure that the result is representative and well comparable and to provide a consistent basis for comparison, the same current values used in the real measurements of the magnet were also applied as the basis for calculating the magnetic field values in the simulation.
The calculated magnetic field values at the center of the aperture were then plotted alongside the measured values taken from documentation and checked for consistency and potential deviations.

2.2.5.2 Validation of the Quadrupole Models

To validate quadrupole models, the method used for dipoles could not be applied directly because the magnetic field in an ideal quadrupole is zero at the center of its aperture. Therefore, an alternative approach was employed to obtain the BI curves. This involved calculating the gradient of the magnetic field within the quadrupole's aperture. The gradient was determined using the formula:

$$\mathrm{G} = \frac{B_2 - B_1}{\Delta x} \tag{8}$$

with $\Delta x = x_2 - x_1 = 0.1 * d_{aperture} - 0$
$B_2 =$ Field at Δx
$B_1 = 0$

This calculated gradient was then used to characterize the behavior of the quadrupole at various current levels. Analogous to the dipoles, the gradient values for the simulation were generated using the same currents as in the real measurements. This ensured comparability and accuracy of the simulation results.

For successful validation of the developed code, a precise match between the measured and simulated BI curves was necessary for every current.

2.3 Results

2.3.1 Magnet Model

Figure 12 shows the cross-section drawing of the MAL magnet from the documentation where the right upper quadrant is framed in red, and Figure 13 displays the model of the upper right quadrant of the MAL magnet generated by the simulation code in OPERA2D. The MAL magnet is an H-shaped dipole, symmetric along the x- and y-axes. The blue area in Figure 13 represents the background, which is defined as *air* in terms of material. The pink area represents the magnet yoke, which was reconstructed as accurately as possible based on the old documentation for the magnet, including the shims. Since the precise material of the magnet yoke is unknown for any of the magnets, a standard material (MBS.bh) was used for the calculations in the simulation.
The orange area simulates the coil, for which copper was selected as the material. The mesh size varies throughout the plot. In areas far from the magnet yoke and the coil, the mesh is bigger. As the mesh approaches the yoke, coil and aperture, it becomes finer. Inside the aperture region, the mesh is particularly fine.

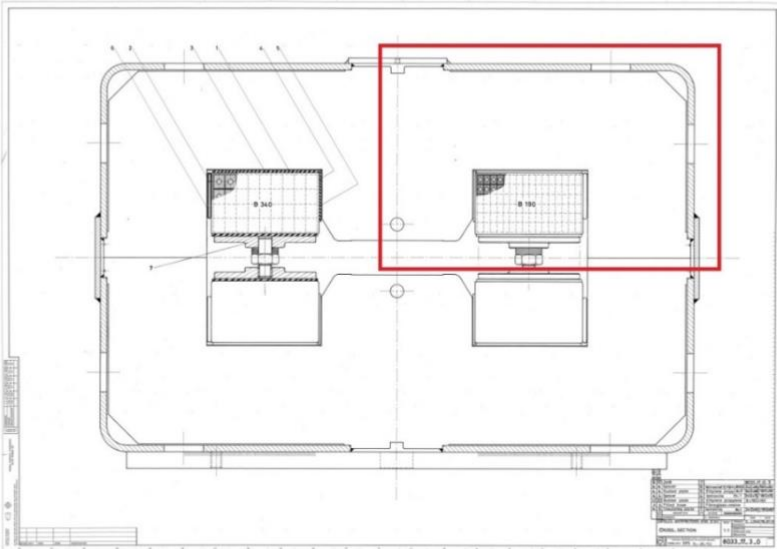

Figure 12: Cross section of the MAL magnet

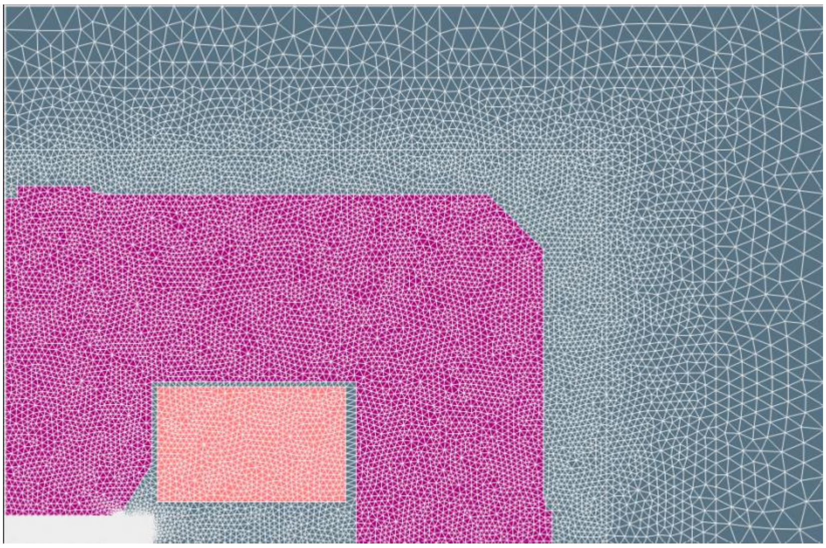

Figure 13: Simulation model of the right upper quadrant of the MAL-magnet with mesh

2.3.2 Validation plots

Figure 14 and Figure 15 compare the measured BI curve (blue line) with the simulated BI curve (orange line) for the material that was designated as the standard for all magnets at the time of generating these plots, namely MBS.bh. It is important to note that the material MBS.bh was initially chosen because it was assumed to represent the magnetic properties of the magnets quite well.

The magnetic flux density B is shown on the vertical axis in Tesla (T) for dipoles and in Tesla per meter (T/m) for quadrupoles, while the current I is displayed on the horizontal axis in Amperes (A). Both, the measured and simulated curves, exhibit a similar non-linear increase in B with increasing I across all magnets.

In the following, two magnets are used to illustrate the results of the model's validation. For clarity, the validation plots for all magnets are included in **Appendix B**.

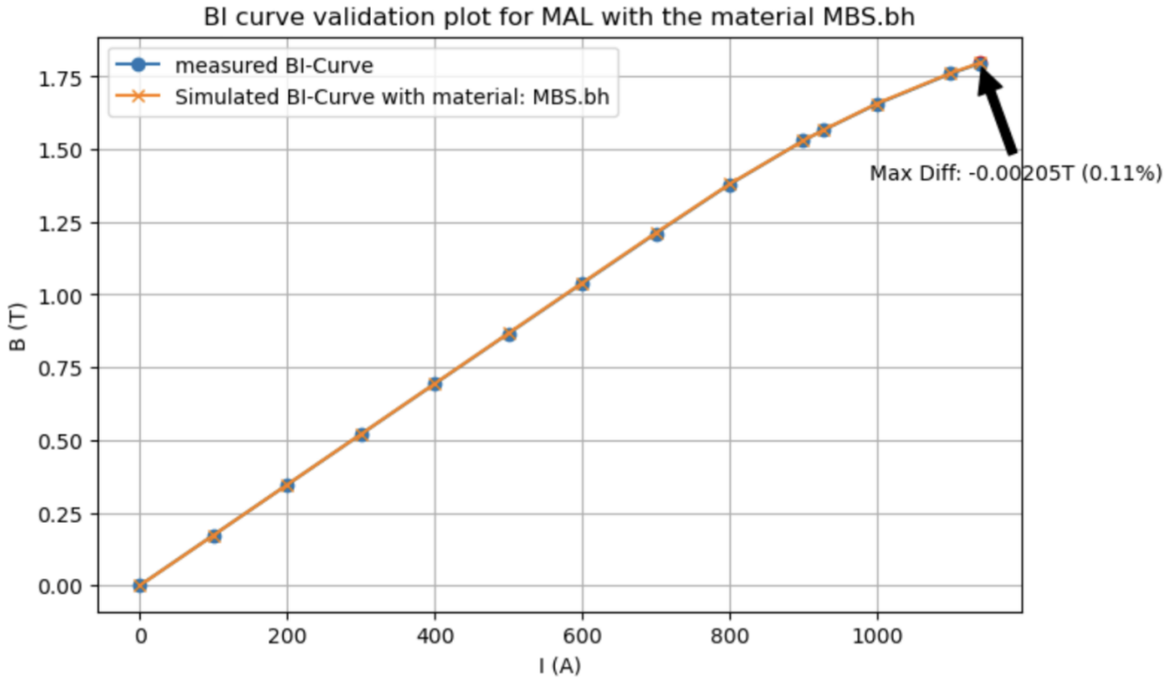

Figure 14: Comparison of the simulated and measured BI curve for the MAL magnet, material used: MBS

Figure 14 shows the validation plot for a well-matching and thus validated simulation model of the MAL magnet. The agreement between the two curves is remarkably precise across the entire range, both in the linear region at low currents and in the saturation region at higher currents. This indicates a high level of accuracy in the simulation model created.
The annotation in the plot marks the maximum difference between the measured and simulated curves, which occurs at a current of 1140 A. The difference is 0.002 T, representing 0.16% of the measured *B*.

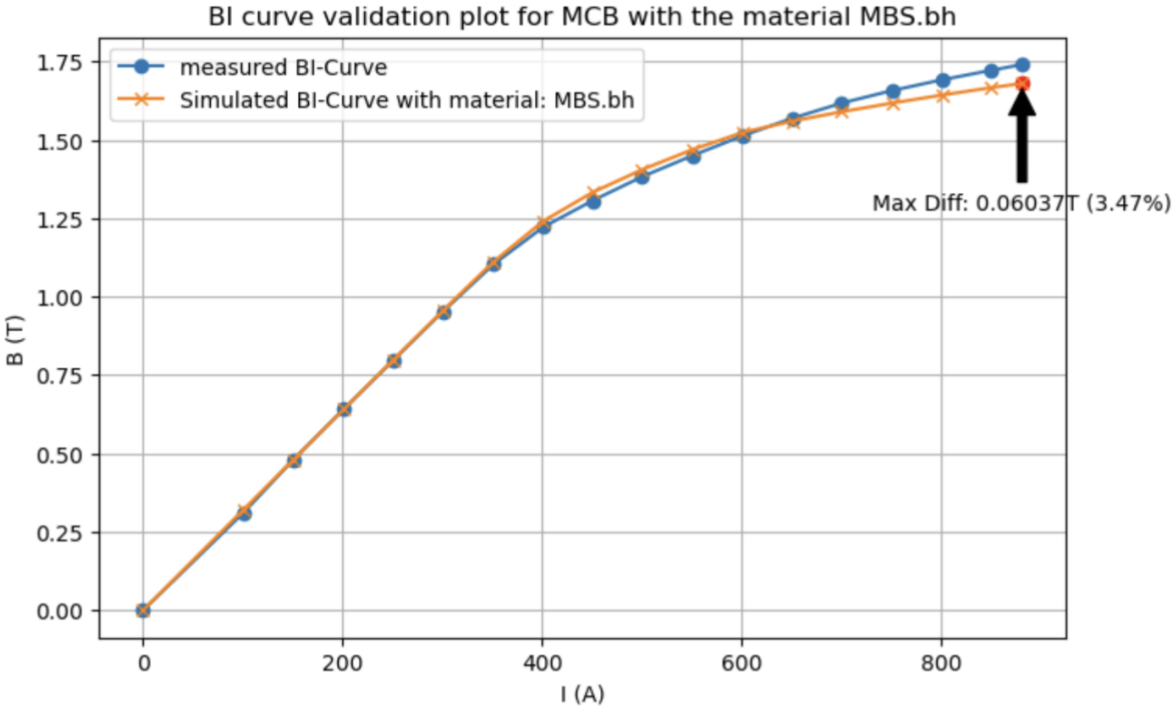

Figure 15: Comparison of the simulated and measured BI curve for the MCB magnet, material used: MBS

Figure 15 shows a validation plot for the MCB magnet, which does not exhibit the level of curve agreement required to justify validation. Up to a current of approximately 350 A, both curves run nearly identically, with minimal differences. Beyond this point, the simulated curve begins to slightly exceed the measured curve but then flattens more quickly as the current increases. The deviation between the two curves becomes more evident at higher currents. At a current of 880.9 A, the simulated curve shows a flux density of about 1.679 T, while the measured curve reaches 1.735 T. This maximum difference is highlighted in the plot by an annotation. The maximum difference is 0.056 T, which corresponds to 3.21% of the measured flux density. This suggests that the simulated material exhibits a different permeability at higher currents compared to the material actually measured.

In Table 5 the maximum deviation in the BI curves for all dipoles are displayed. To maintain clarity, only the maximum deviations of the curves in the validation plots are presented. The first column contains the name of each magnet, the second column displays the absolute value of the maximum deviation between the measured and simulated curves and the third column provides the maximum deviation as a percentage.

Table 6 is identical to Table 5, except that it documents all the quadrupoles to be modeled. In this case, the maximum deviation between the curves is given in T/m.

Magnet	Max. deviation in T	Max. deviation in %
MAL	0.002	0.16
MBE	0.007	0.61
MBN	0.054	2.58
MBPL_110	0.040	2.40
MBPL_140	0.057	3.04
MBPL_170	0.024	1.41
MBPL_200	0.036	2.07
MBPS_140	0.074	5.19
MBW	0.018	2.61
MCA	0.024	1.99
MCB	0.056	3.21
MCV	0.009	0.74
MCVS	0.002	1.04
MCW	0.061	4.34
MDA	-	-
MDL	0.004	0.40
MDS	0.005	0.55
MDP	0.028	5.62
MDX_100	0.011	1.41
MDX_80	0.022	1.63
MDX_52	0.017	1.45
MPLS	0.054	5.38
MSN	0.011	0.64
MTN	0.052	2.46
MTR	0.105	4.78

Table 5: Maximal absolute and relative deviation of the simulated from the measured BI curve for every dipole

Magnet	Max. deviation in T/m	Max. deviation in %
QFS	0.647	3.30
QM	-	-
QNLB	0.359	1.32

QNL	0.317	1.31
QNRB	0.467	1.31
QPL	0.310	2.82
QPS	0.505	4.55
QSL	0.975	4.89
QTA	0.261	1.34
QTL	0.821	2.97
QTS	0.255	1.34
QWL	0.210	1.06

Table 6: Maximal absolute and relative deviation of the simulated from the measured BI curve for every quadrupole

2.4 Discussion

The validation plots presented in 2.3 on one hand show very good agreement between the measured and simulated curves, as demonstrated by the example of the MAL magnet. On the other hand, the validation plots for some magnets also reveal inconsistencies in the curve progression, as illustrated by the MCB magnet.

To discuss possible causes for these discrepancies, it is important to take a closer look at the model creation process and the data sources used to create the models. As mentioned earlier, the simulation models are based on existing, old documentation. These documents were thoroughly examined to gather as much relevant information as possible about the precise geometry of the magnet components. For most magnets, detailed data on geometry and coil configuration was found. However, for a few magnets, not all the necessary information was available, which could be a reason for uncertainty in the model.

Consequently, the results of the model validation can be divided into two main categories. The first category includes the validation plots where the simulated BI curve already shows a high degree of agreement with the measured BI curve. The strong agreement between the measured and simulated curves can be attributed to two key factors.

Firstly, well-documented measurement data of the BI curve at the center of the aperture was available for these magnets. Secondly, very accurate and complete drawings of the magnet's cross-section and its components were found. This includes exact information about the geometry of the yoke, shims, and coils, as well as the number of windings. With all this data, it was possible to recreate the magnet in the model so accurately that the calculated magnetic values closely matched the measured values.

The second category includes those magnets whose validation plots show a less clear agreement between the simulated and measured curves. This means that the two curves do not align with each other. For these magnets, either no well-documented or up-to-date BI curve measurement could be found, or the simulation model could not be fully developed to include all essential details due to insufficient documentation of the magnet's geometry.

For some magnets, where no or insufficient documentation of the measured BI curve was available, satisfactory comparison values were obtained by scaling the measurement data from another magnet within the same magnet family. In this context, magnets belonging to the same magnet family means that their cross-sections are either identical or differ only minimally. Consequently, it can be assumed that the magnetic fields they generate are comparable.

An example of this is the QNLB magnet, for which no measured BI curves could be found. This magnet belongs to the family of QNL magnets and shares the exact same cross-sectional geometry as the QNL magnet. The only difference between the QNL and QNLB magnets lies in the mineral-insulated coils. This results in a slight modification of the coil geometry, but it has only a minor impact on the simulation of the field at the center of the aperture. For this reason, the measured BI curve of the QNL magnet was used for the validation of the QNLB model.

A similar approach was applied to the QTS magnet. This magnet has the same cross-sectional and coil geometry as the QTL magnet, for which precise measurement data is available. The only difference between these two magnets is their length. However, since the simulations were conducted in 2D, the length of the magnet has no effect on the simulation results. Hence, the same measurement data as for the QTL magnet was used but limited to the maximum current of the QTS, which is 416 A.

Another example is the QNRB magnet, for which no measured BI curve could be found in the documentation either. The QNRB differs in cross-sectional geometry from the QNL magnet, so this time the measured BI curve of the QNL could not be used for this validation. However, a measured BL curve was found, which was subsequently used for validation. Given a BL curve representing the integrated magnetic field at the center of the aperture, the corresponding magnetic field B could be calculated using the formula:

$$B = \frac{BL}{l} \tag{9}$$

where l represents the magnetic length of the magnet.
When plotted against the current, the calculated B values, again, resulted in a BI curve, which then could be used to validate the QNRB simulation model.

Using existing data and scale or transforming it, allowed comparable validation results for similar magnets to be achieved, even when direct measurement data was lacking.
In this work, only the MDA magnet could not be validated. Although a functional simulation model is available, the required measurement data from the real magnet was missing, preventing the model's validation.

In addition to the geometric inaccuracies that may arise from incomplete documentation, a key factor contributing to the discrepancies observed is the uncertainty about the exact material of the magnet yoke. To generate the validation plots, the same material was used for all magnets, which is assumed to accurately reflect the real magnetic properties. However, this material may differ significantly from the actual yoke material in terms of magnetic properties, such as permeability and saturation behavior.
The discrepancies between the measured and simulated BI curves can therefore be attributed to both geometric inaccuracies, due to missing information in the documentation, and differences in material properties. These inaccuracies can become more significant at higher magnetic fields, where the magnetic field distribution is more sensitive to geometric details due to saturation.

To minimize these inaccuracies and improve the agreement between measurements and simulations, it was essential to know the material of each magnet as accurately as possible. Therefore, the second part of this thesis focuses on finding a method of determining the exact magnet material. This material identification is intended to align the simulated curves in the validation plots of all magnets with the measured curves, allowing each magnet model to be considered validated.

3 Identification of the magnetic materials

3.1 Motivation

In **Error! Reference source not found.** the simulation code was successfully validated, d emonstrating its ability to deliver realistic results. However, to further refine the precision of these simulations, it is essential to accurately define the magnetic properties of each material used in the construction of the magnets. In OPERA2D, this is resolved by using the corresponding BH curve of the material.

Unfortunately, no measured BH curves for the specific materials used in the magnet yokes were found in any of the existing documentation, despite a detailed review of the available documentation, including those related to the production of the magnets. Furthermore, conducting direct measurements of the BH curves on the assembled magnets is unfeasible due to the physical inaccessibility of the yoke materials as the magnets are already installed within a beamline configuration, where such components are not directly reachable for testing. Given these constraints, a new method for assigning appropriate BH curves to the magnet models had to be found.

3.2 Methodology

The proposed approach was based not on the direct measurement of the BH curve on the magnet but on the identification of the chemical composition of the material. First, the magnets were grouped into subgroups based on their manufacturer and production year. It was assumed that magnets within the same group were made from the same type of steel. Subsequently, a search was conducted in the material storage to determine whether steel samples could be found for each of these groups. By analyzing the chemical composition of these steel sheets and comparing it to the chemical composition of the yoke material of each magnet, a direct correlation between a specific steel sheet and a magnet should then be established.

Once a steel sheet was confidently linked to a particular magnet, it the should be used to produce a test specimen for BH curve measurements. CERN provides several methods of determining the BH curve of a material using samples of the respective material. Two of the methods considered were the measurement with an Epstein frame [33] or with ring samples [34]. The BH curve obtained for a respective material could then be integrated into the simulations, improving the accuracy of magnet models.

3.2.1 Chemical Analysis Experiment with XRF and OES

A steel sheet was found in storage, which was believed to correspond to SPS steel. SPS steel in this context means the steel that was used to produce the main magnets for the SPS at CERN. This steel was used in the manufacture of several magnet families located in the North Area. The identification of this steel sheet was important as it served as a reference material for the following measurements.

After pre-grouping the magnets, the next step was to determine the chemical composition of the steel sample identified, as well as the chemical composition of the magnets prepared for testing. This analysis was crucial to verify whether the steel sample and one from the magnets are identical in their chemical composition and thus the steel sample actually represented the SPS steel. Confirming this hypothesis would allow a large group of magnets to be assigned to a specific material. Additionally, the same measurement method could be applied to other magnet groups to determine their chemical composition, if a sample of their steel was found. This would allow for systematic and comprehensive characterization of the various steels used.
For the measurement of chemical composition, two main methods were used: XRF and OES.

XRF is a technique used to determine chemical composition by directing X-rays at a material, which then emits characteristic fluorescence radiation. This fluorescence is element-specific and allows for the identification and quantification of the elements present in the sample. XRF is particularly useful due to its fast analysis times, minimal sample preparation, and the ability to detect a wide range of elements with high precision and accuracy. [35][36]

Optical emission spectroscopy (OES) is another method for analyzing chemical composition. In this technique, the material is excited in a plasma or spark discharge, causing it to emit light. The emitted light is then spectrally decomposed and analyzed. Each element emits light at specific wavelengths, enabling a qualitative and quantitative analysis of the chemical composition. OES is particularly suited for the analysis of metals and alloys, offering high sensitivity and the ability to detect both major and trace elements. [37]

For both methods, the use of a portable version of the measurement device made it possible to conduct measurements directly on the magnet, on-site, in the magnet measurement hall at CERN. This allowed for measurements to be taken using both techniques for cross-checking. To perform a measurement using XRF or OES, a smooth, polished, grease- and paint-free surface of the material to be analyzed is required. [36] However, in this work, the yokes of already fully assembled magnets had to be measured. These yokes are laminated, consisting of approximately 1.5 mm thick lamellae that are compressed and held together by two solid end plates. Once the magnet is fully assembled, the surface of the individual lamellae is no longer accessible. Even if the magnet was opened in the measurement hall, only the surface of the magnet poles, created by the parallel arrangement of the lamellae, remained accessible (see Figure 16).
Given these circumstances, all measurements on magnets could only be conducted perpendicular to the surface of the individual lamellae, across multiple lamellae. This means that the analysis of the chemical composition was impacted by the limited accessibility and the less-than-ideal surface preparation. Despite these challenges, both the surfaces of the magnets to be measured and the surface of the steel sample were thoroughly polished and cleaned with alcohol before measurement began. These cleaning and polishing procedures were necessary to remove paint, coatings, and other potential contaminants that could distort the measurement results.
The only measurement conducted under ideal conditions was that of the SPS steel sample. This sample allowed for precise determination of the chemical composition, as it was fully accessible and properly prepared. Three different preparation methods were applied to the steel sample to verify the accuracy of the measurement process. One section of the sample was brushed and then cleaned with alcohol, another section was cleaned with alcohol only, and a third section was left untreated. This sample can also be seen in Figure 16.

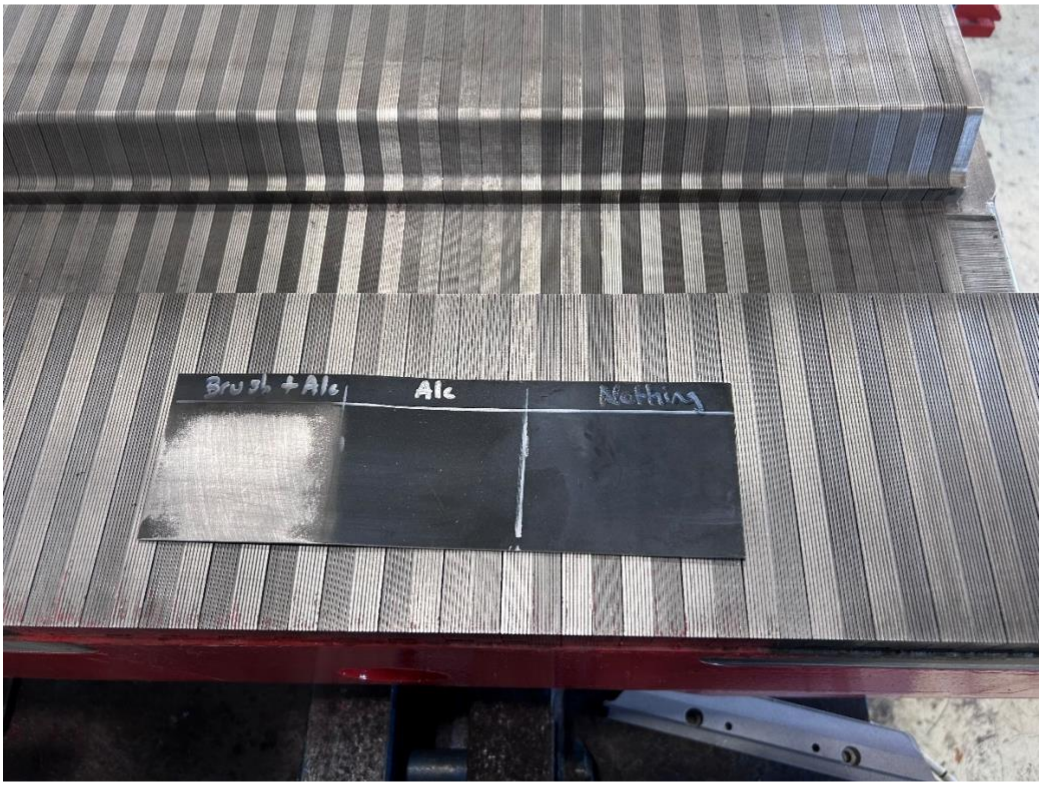

Figure 16: Lower half of a laminated H-shaped dipole on which measurements were taken and on top there is the SPS-steel sample which was prepared in three ways, going from left to right: brushed+ cleaned with alcohol, just cleaned with alcohol and no special preparation.

3.2.2 Results and Discussion

3.2.2.1 Magnet Groups

Based on the results that could be obtained from the document review, the magnets were grouped into smaller magnet families. This grouping can be seen in Table 7 where magnets with the same color represent a subgroup.

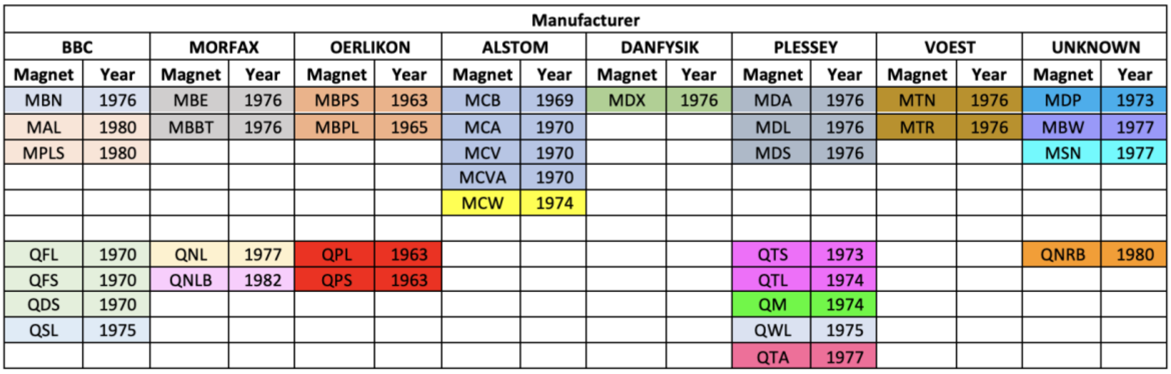

Manufacturer															
BBC		**MORFAX**		**OERLIKON**		**ALSTOM**		**DANFYSIK**		**PLESSEY**		**VOEST**		**UNKNOWN**	
Magnet	**Year**	**Magnet**	**Year**	**Magnet**	**Year**	**Magnet**	**Year**	**Magnet**	**Year**	**Magnet**	**Year**	**Magnet**	**Year**	**Magnet**	**Year**
MBN	1976	MBE	1976	MBPS	1963	MCB	1969	MDX	1976	MDA	1976	MTN	1976	MDP	1973
MAL	1980	MBBT	1976	MBPL	1965	MCA	1970			MDL	1976	MTR	1976	MBW	1977
MPLS	1980					MCV	1970			MDS	1976			MSN	1977
						MCVA	1970								
						MCW	1974								
QFL	1970	QNL	1977	QPL	1963					QTS	1973			QNRB	1980
QFS	1970	QNLB	1982	QPS	1963					QTL	1974				
QDS	1970									QM	1974				
QSL	1975									QWL	1975				
										QTA	1977				

Table 7: Magnets grouped by manufacturer and manufacturing year

By pre-grouping the magnets into smaller clusters, initial consolidation was achieved. All magnets grouped by their manufacturer and year of production are subsequently assigned the same material.

3.2.2.2 XRF Measurements

In contrast to the measurements of the steel sample, both measurement methods XRF and OES failed to deliver the expected results when applied to the magnet yokes.

The results of the measurements conducted using XRF, despite prior polishing and careful preparation of the measurement sites, were inaccurate. They included elements that should not typically be present in the steel of magnet laminations. This was due to tiny contaminants present in the gaps between the lamellae, which could not be removed even with repeated polishing. OES could also just be applied effectively to the SPS steel sample. When attempting measurements on the magnet poles with parallel lamellae, no meaningful results could be obtained, even from the very first magnet, which led to the decision not to proceed with further measurements on other magnets.

Despite the challenges, it was possible to find a match in the chemical composition between the XRF measurement of the SPS sample and the magnet MBB in the North Area.

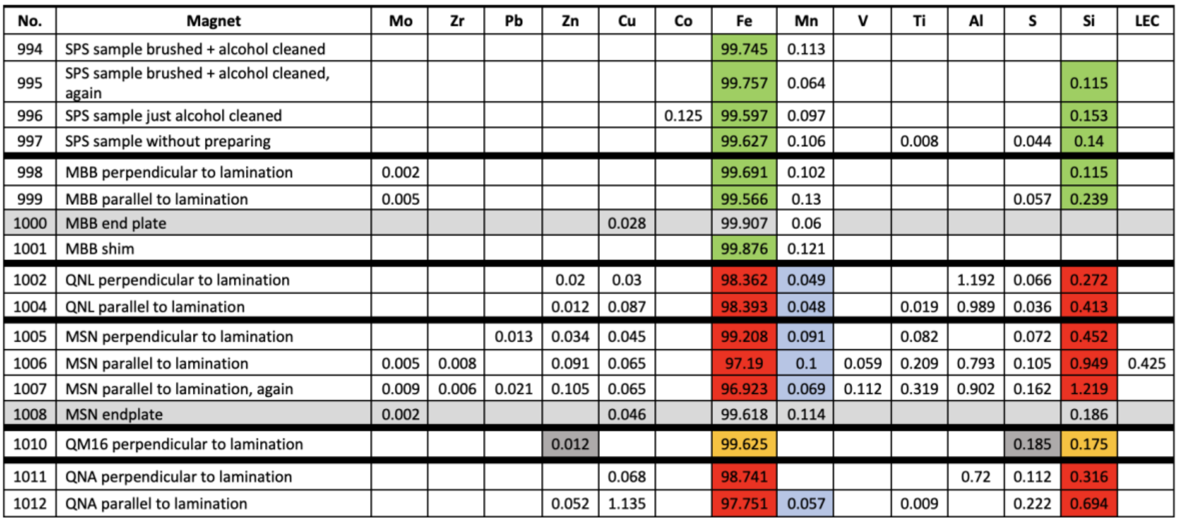

No.	Magnet	Mo	Zr	Pb	Zn	Cu	Co	Fe	Mn	V	Ti	Al	S	Si	LEC
994	SPS sample brushed + alcohol cleaned							99.745	0.113						
995	SPS sample brushed + alcohol cleaned, again							99.757	0.064					0.115	
996	SPS sample just alcohol cleaned						0.125	99.597	0.097					0.153	
997	SPS sample without preparing							99.627	0.106		0.008		0.044	0.14	
998	MBB perpendicular to lamination	0.002						99.691	0.102					0.115	
999	MBB parallel to lamination	0.005						99.566	0.13				0.057	0.239	
1000	MBB end plate					0.028		99.907	0.06						
1001	MBB shim							99.876	0.121						
1002	QNL perpendicular to lamination				0.02	0.03		98.362	0.049			1.192	0.066	0.272	
1004	QNL parallel to lamination				0.012	0.087		98.393	0.048		0.019	0.989	0.036	0.413	
1005	MSN perpendicular to lamination			0.013	0.034	0.045		99.208	0.091		0.082		0.072	0.452	
1006	MSN parallel to lamination	0.005	0.008		0.091	0.065		97.19	0.1	0.059	0.209	0.793	0.105	0.949	0.425
1007	MSN parallel to lamination, again	0.009	0.006	0.021	0.105	0.065		96.923	0.069	0.112	0.319	0.902	0.162	1.219	
1008	MSN endplate	0.002				0.046		99.618	0.114					0.186	
1010	QM16 perpendicular to lamination				0.012			99.625					0.185	0.175	
1011	QNA perpendicular to lamination					0.068		98.741				0.72	0.112	0.316	
1012	QNA parallel to lamination				0.052	1.135		97.751	0.057		0.009		0.222	0.694	

Table 8: XRF measurement results for all magnets measured

Table 8 presents the results of the XRF measurements of the SPS sample and the measured magnets MBB, QNL, MSN, QM16, and QNA in percent. The columns display the measurement number, the corresponding magnet with the measurement direction, and the various chemical elements detected. Each row represents the results of a specific measurement for the respective magnet. Identical color markings indicate similar quantities of a given element, while different color blocks highlight variations in the detected amounts of an element.

A comparison of the measured values in the SPS sample and MBB revealed a high similarity in their chemical composition, particularly in iron (Fe) content and the low concentrations of manganese (Mn) and silicon (Si). The SPS samples exhibited an Fe content ranging from 99.6% to 99.8%, and the MBB samples also range from 99.6% to 99.8%. The results furthermore indicated that both SPS and MBB samples have Fe ≥ 99% and Si ≤ 0.25% (highlighted in green), whereas all other magnets show Fe ≤ 99% and Si ≥ 0.25% (highlighted in red).

The QNL samples show a lower Fe content (98.36% to 98.39%) compared to the SPS and MBB samples.

The MSN samples display the greatest variation in composition, with a Fe content ranging from 96.9% to 99.2%, along with significant fluctuations in Mn, Si, Titanium (Tu), Aluminium (Al), and Sulphur (S) concentrations. For example, the Mn content varies from 0.069% to 0.1%, and the Al content ranges from 0% to 0.9%.

The QM16 sample has an Fe content of 99.6%, along with moderate amounts of Zinc (Zi) (0.01%), S (0.19%), and Si (0.18%).

The QNA samples show significant differences in Fe content (97.75% to 98.74%) and in the amounts of Copper (Cu) and Al. For instance, measurement 1012 contains 1.14% Cu and 0% Al, while measurement 1011 contains 0.07% Cu and 0.72% Al.
Measurements 1000 and 1008 were excluded from this context as they refer to the end plates of the magnets, which are known to be made from different materials.

Overall, the analysis confirmed a high degree of similarity between the SPS and MBB samples. The consistent values for Fe, Mn, and Si content, along with the low concentrations of other elements, suggested that the SPS and MBB samples were made from the same or a very similar type of steel. This finding supported the hypothesis that certain magnets in the North Area, such as the MBB, were made from steel comparable to that found in the SPS sample.
All other magnets exhibited higher deviations in iron content and additional elements were detected, ruling out a direct match to SPS steel. Significant fluctuations were also observed between measurements on the same magnet. For instance, measurement 1006 on the MSN magnet showed a Mn content of 0.1% and a Vanadium (V) content of 0.59%, while measurement 1007, taken in the same direction, showed 0.006% Mn and 0.11% V.

However, the dimensions of this SPS steel sample did not meet the requirements for a BH curve measurement using the Epstein frame or ring samples, making a corresponding BH curve measurement impossible.
Given the imprecise measurement conditions, it was not possible to get meaningful measurements with either XRF or OES, and thus, comprehensive chemical characterization of all magnet materials could not be achieved. The limited accessibility and the unavoidable contamination from the gaps between the lamellae significantly influenced the measurement results. Due to the challenges described and the limited time available, chemical material analysis was not pursued further in this study.
These facts made it necessary to find an alternative approach to assign the correct magnet materials in the simulations. This approach is described in 4.

4 Material Classification

4.1 Motivation

Since the chemical analysis did not yield any satisfactory results, another method had to be found. Rather than conducting measurements on the actual magnet material or analyzing its chemical composition, a simulation-based alternative was chosen. This method was based on the already known and validated BI curves, providing a reliable basis for analyzing different materials. The aim was to assign each simulation model a known material from the database with an already defined BH curve.

4.2 Methodology

4.2.1 Determining the best-fit Material

To identify the material that most accurately reflected the magnetic behavior of the real magnet, this approach involved the comparison of the BI curves of a series of potential yoke materials in simulations with the measured BI curve of the respective magnet.
The set of materials used is the same as previously defined in 2.1.2.

To generate the BI curves for comparison, the same magnet model was simulated using each of the eight materials, and the magnetic field at the center of the aperture was calculated. To ensure a consistent basis, the same currents used in the real measurement were applied in the simulation of the magnet model. After running the simulations for all materials, the calculated BI curves were plotted alongside the measured BI curve, allowing for direct comparison. The measured BI curve of the magnet served as the reference curve.

Each material was evaluated based on the deviation of its BI curve from the measured reference BI curve.
The maximum absolute difference (AD) refers to the greatest deviation in the B-field between the measured and simulated curves and is calculated as:

$$AD_{I_k} = \left|B_{measured,I_k} - B_{simulated,I_k}\right| \tag{10}$$

and the total absolute difference (TAD) is a value that calculates the deviation between the comparison and reference curves at all points and averages it over the number of points. It is calculated as:

$$TAD = \sum_{k=0}^{n} AD_{I_k} = \sum_{k=0}^{n} \left|B_{measured,I_k} - B_{simulated,I_k}\right| \tag{11}$$

where I_k is the specific current at index k.
The maximum relative difference (RD) indicates the deviation as a percentage of the measured value and is calculated as:

$$RD_{I_k} = \frac{\left|B_{measured,I_k} - B_{simulated,I_k}\right|}{\left|B_{measured,I_k}\right|} \cdot 100\% \tag{12}$$

The material whose simulated BI curve showed the smallest TAD was subsequently designated as the new standard material for that specific magnet and defined as the new yoke material in the *Input file*. The decision assumed that this material most accurately replicates the magnetic properties of the real material. This procedure was applied to each magnet observed in this work.

4.2.1.1 Comparison of old and new Material

To enable a direct comparison and assess whether the simulation accuracy improved with the new material, the AD_{I_k} and RD_{I_k}, as well as the TAD between the simulated and the measured BI, were calculated, once for the old standart material MBS and once for the newly assigned best-fit material of the respective magnet. MBS was selected as standard material for this analysis because it has long been considered a reliable material that provides a good fit for most magnet models.

Since all of that benchmarking was done just at the center of the aperture, it could not be guaranteed, even after this material study, that the selected material best represented the actual properties of the magnet. There was still some uncertainty about whether a different material, with a BI curve that differed more in the center, might actually behave more like the real magnet in the region outside the apterture.
To address this question not only qualitatively but also quantitatively, it was necessary to do another study including the whole field map area of the magnet.

4.2.2 Material Sensitivity Study

In this study, the field map—representing the magnetic field across the entire magnet geometry, the background, the coils, and the GFR—was used to examine the changes in the magnetic field using different yoke materials.
To establish a basis for equivalent comparisons between the different materials, the newly defined standard material for each magnet was chosen as the reference material. Using this material, the reference field map was calculated. Subsequently, field maps were also calculated for all the seven other possible magnet materials. The field map created by the

newly assigned material is called *reference field map* and the field maps of all other materials are called *comparison field maps*.

The goal was to assess the sensitivity of different magnet models to material changes by comparing their magnetic field behavior under varied conditions. This is achieved by analyzing the absolute deviations between a reference field map and several comparative field maps, focusing on identifying regions where the deviations exceed a predefined threshold. Specifically, the analysis aims to determine what percentage of these absolute deviations exceeds a threshold value of 0.1 T, indicating potential material sensitivity. The results of this comparison can then be used to classify the magnet model as either *sensitive* or *not sensitive* to material changes, depending on the magnitude of the deviations within a specific reference region.

4.2.2.1 Selection of Current Levels

To carry out the sensitivity analysis, two distinct currents were selected based on their positions in the magnet's BI curve:

1. Saturation Region Current I_{sat}: This current is chosen from the saturation region of the BI curve. In this case, the maximal operation current for each magnet was chosen as I_{sat}. The behavior in this region is critical for understanding how the magnet responds to high levels of current.

2. Linear Region Current I_{lin}: To represent the linear behavior of the magnet, a current is chosen that is half the saturation current. Mathematically, this can be expressed as:

$$I_{lin} = \frac{I_{sat}}{2} \tag{13}$$

By performing this analysis at two different current levels, the study provides insight into how material changes affect the magnet's behavior in both linear and saturated regions. This is important because different magnet models may exhibit varying degrees of sensitivity to material changes depending on whether the magnet is operating in its linear or saturation region.

4.2.2.2 Defining the Reference Region

To perform a meaningful comparison, it is necessary to define a so-called reference region within the reference field map for each magnet model. This region serves as a consistent area of interest when comparing the reference field map with multiple comparison field maps for that magnet model under the same current conditions. The reference region is particularly important as it narrows the focus of the analysis to areas of the magnet where the magnetic field strength exceeds a minimum value, ensuring that only significant deviations are considered. This also helps to avoid unnecessary noise in the data from low-field regions where minor deviations may not significantly impact the magnet's overall performance.

The green area in the plots in Figure 17 illustrates the reference region for a simulation of an MCB magnet at a current of $I_{lin} = 440$ A (left) and $I_{sat} = 880$ A (right). This region encompasses the entire magnet yoke, the aperture, and significant portions to the left and right of the aperture.

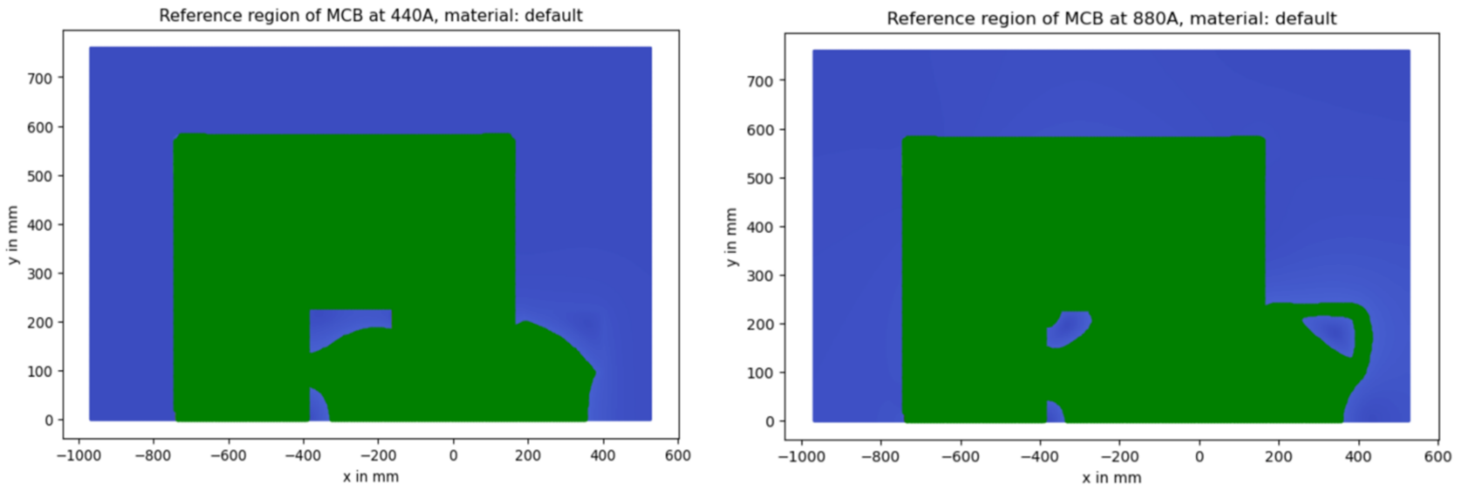

Figure 17: Reference region where B > 0.1 T for the MCB magnet at 440 A (left) and 880 A (right)

The blue area represents magnetic field strengths below 0.1 T, which were not considered in further analysis.

The reference region is specific to each magnet model and varies depending on the current applied. For each magnet model, the reference region must be defined independently for each current level at which the field maps are generated. This ensures that the region of interest accurately reflects the areas where the magnetic field is most relevant to the performance of the magnet. Once the reference region is defined, it remains constant for all subsequent comparisons of that particular magnet model.

4.2.2.3 Calculation of Absolute Deviations

The next step involves calculating the absolute deviations in the magnetic field values between the reference field map and each comparison field map at every point within the reference region. The difference is calculated point by point, generating a *difference field map* for each comparison.

Mathematically, the absolute deviation at each point i is given by:

$$\Delta B_i = \left| B_{ref,i} - B_{comp,i} \right| \tag{14}$$

where $B_{ref,i}$ is the magnetic field value at point i in the reference field map, and $B_{comp,i}$ is the corresponding value in the comparison field map. The resulting difference field map represents the absolute difference in magnetic field strengths across the entire reference region.

For each magnet model, these difference field maps are calculated for the two different current levels: one at I_{sat} and the other at I_{lin}.

4.2.2.4 Threshold Exceedance and Sensitivity Analysis

To find out whether the resulting deviations were large enough to cause changes in the particle trajectories during the simulations, a threshold was defined in a study done by a colleague. In this study, the accuracy of predicted field maps for use in particle tracking simulations was assessed. The focus was on muon transport through accelerator beamlines. The study examined how magnetic field deviations influence muon deflection compared to multiple scattering effects from magnet materials.

The study concluded that, in practical terms, if the magnetic field alters the total deflection angle by less than 10%, its influence can be considered minimal, as multiple scattering becomes the dominant factor in this situation. Therefore, the threshold in this case was determined as 0.1 T. [15]

Small differences in the magnetic field below this threshold $(\Delta B < 0.1\,T)$ could be ignored, as it was assumed that they do not lead to a significant change in particle trajectory.

In regions where the deviations exceed this threshold, the magnet model is considered to exhibit sensitivity to material changes.

To quantify this sensitivity, the analysis focuses on calculating the percentage of points within the reference region where the absolute deviation exceeds the 0.1 T threshold. This percentage is determined by:

$$\frac{\sum_{i=1}^{N} \delta(\Delta B_i > 0.1\,T)}{N} \cdot 100\% \tag{15}$$

where N is the total number of points within the reference region, and $\delta(\Delta B_i > 0.1\,T)$ is an indicator function that equals 1 if the absolute deviation at point i exceeds 0.1 T, and 0 otherwise. This calculation yields the percentage of points in the reference region where the deviation is significant enough for further investigation.

Once the percentage of threshold exceedances is calculated for each current level, the magnet model's sensitivity to material changes is evaluated based on the following criteria:

- If there are no exceedances of the 0.1 T threshold, or if the exceedances account for less than 1% of the total points in the reference region, the magnet model is classified as *not sensitive* to material changes at the given current. This indicates that any material changes within the comparative field maps have a negligible impact on the magnet's magnetic field performance.
- Conversely, if the percentage of points exceeding the 0.1 T threshold is greater than 1%, the magnet model is classified as *sensitive* to material changes at the given current. This suggests that even small variations in material properties may significantly alter the magnetic field distribution within the magnet, particularly in the areas of interest defined by the reference region.

4.3 Results & Discussion

4.3.1 Material Study

4.3.1.1 Determine the best-fit Material

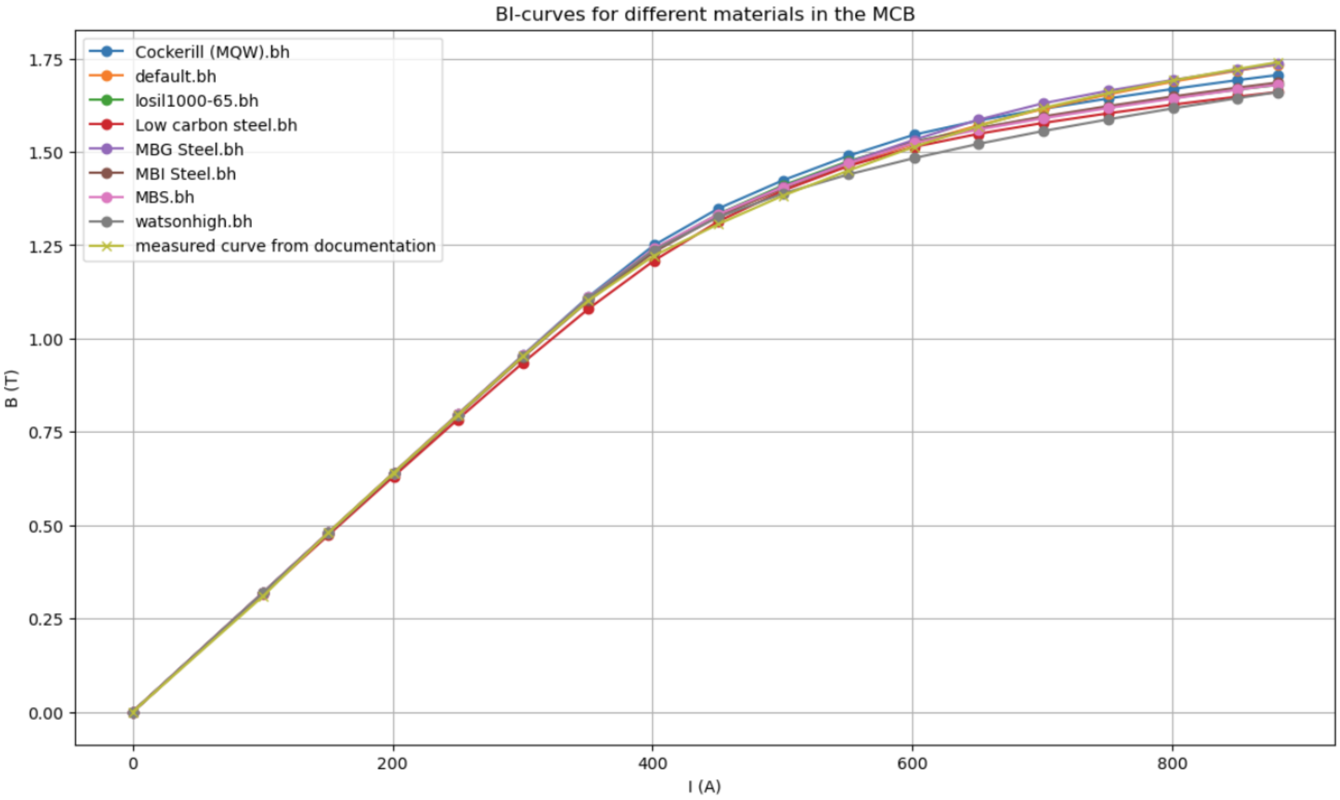

Figure 18: measured BI curve in comparison with the simulated BI curves for the MCB magnet plotted with all materials observed in this study

The plot shown in Figure 18 compares the BI curves simulated with all observed yoke materials to the real measured BI curve of the MCB magnet. The horizontal axis represents the current in A, ranging from 0 to 880 A. The vertical axis shows the magnetic flux density in T, with a range of 0 to 1.75 T.

The plot features eight curves, each representing a different material, as specified in the legend.

All curves start at [0,0] and exhibit the typical behavior of magnetic saturation. Starting from the same point, they are closely aligned and for currents below 200 A, all curves rise linearly. Around 200 A, they start to flatten slightly, indicating the start of saturation. At this point, the curves also begin to diverge slightly, with differences becoming more pronounced as the current increases. Between 400 A and 880 A, the curves flatten more and spread further apart, approaching a maximum value of around 1.70 T.

At a nominal current of 880 A, the lowest magnetic field value is 1.66 T, generated by the material watsonhigh, while the highest magnetic field value of 1.734 T was generated with MBG Steel.

By comparing the seven simulated curves with the reference curve and calculating their deviation, the curve with the smallest deviation from the reference curve was identified. In the case of the MCB magnet, the curve yielding the smallest deviation was generated with the material default.bh.

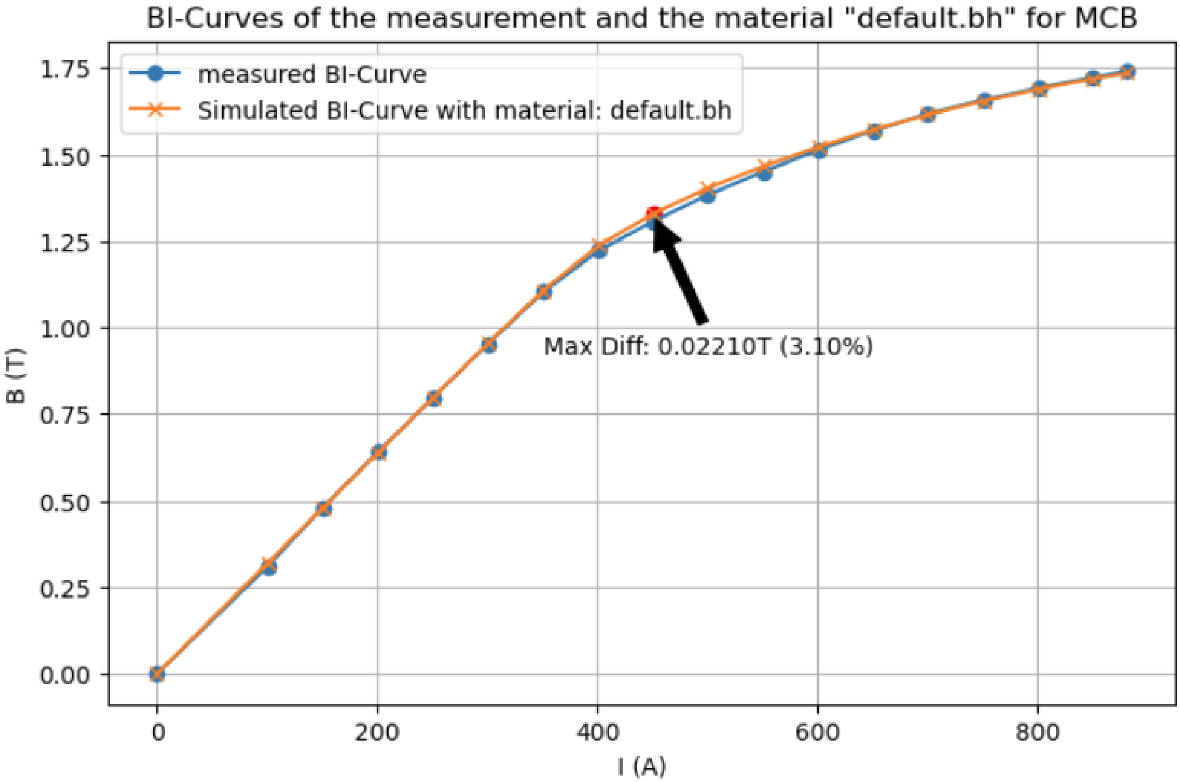

Figure 19: comparison of the measured BI curve with the BI curve of the best-fitting material default for the MCB magnet

The plot in Figure 19 illustrates the comparison of the measured BI curve with the BI curve of the material default.bh.
The horizontal axis, again, represents the current in A, while the vertical axis shows the magnetic flux density in T. The current range spans from 0 to 880 A, and the magnetic flux density ranges from 0 to 1.75 T.
The measured BI curve is represented by blue dots, while the simulated BI curve for the material designated as default.bh is depicted with orange crosses.
Both curves start at [0,0] and exhibit a nearly identical progression, indicating very good agreement between the simulation and measurement. At lower currents, both curves rise almost linearly and show a tendency toward saturation at higher currents. The maximum deviation occurs at around 400 A and is 9.35 mT, corresponding to 0.76%. A black arrow marks the point of maximal deviation.

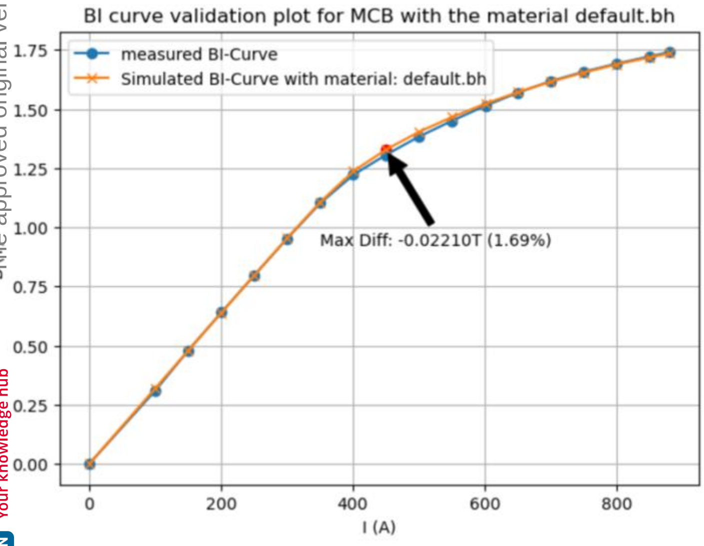

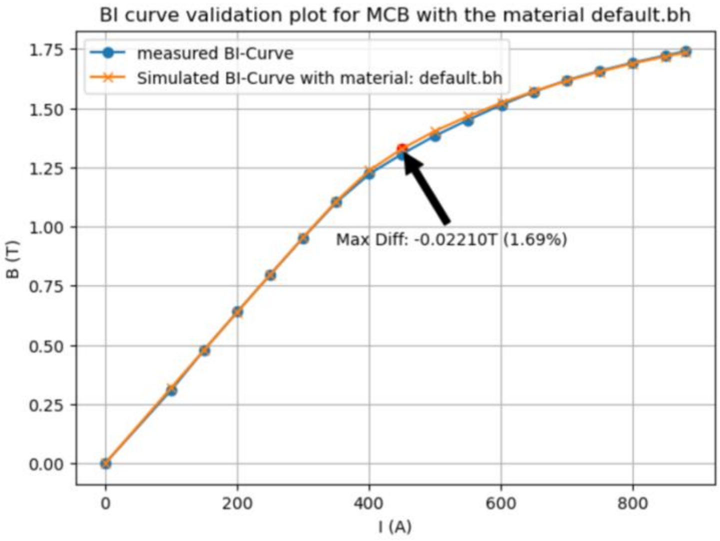

Figure 20: Accordance of the measured and simulated BI curves for the MCB magnet before (left) and after (right) the material study and the assignment of the new standard material default.bh

The two diagrams in Figure 20 ultimately compare the results from the material study applied to the validation plot from 2.2.5. The left-hand diagram shows the comparison between the measured BI curve and the BI curve calculated with the old standard material, MBS. This plot corresponds to the validation plot of the simulation code before the material study. The right-hand diagram shows the same comparison but using the newly assigned standard material default which was found to be the best-fit in the material study.

Both diagrams show that the BI curves rise almost linearly at lower currents and asymptotically flatten toward around 1.75 T at higher currents. In both cases, the agreement between the measured and calculated values is very good in the linear range at low currents. However, differences appear in the saturation region. While the simulated curve with the material MBS flattens more quickly at higher currents, falling below the measured curve, the BI curve with the material default matches the measured curve exactly up to the maximum current of 880 A. The largest deviation in the original plot occurs at 880 A, amounting to 55.8 mT, which corresponds to 3.21%. By using the new material, the error was reduced to 9.35 mT, or 0.76%, with this deviation now occurring at 400 A.
The result of this comparison therefore confirms the assumption that the newly assigned material more accurately represents the realistic properties of the magnet—at least within the GFR—and thus could enable more realistic simulation results.

4.3.1.2 Comparison of old and new Material

After determining the best-fit material for each magnet in 4.2.1, the results were compared with the pre-grouping of magnets to evaluate whether magnets belonging to the same family were consistently assigned the same material. In most cases, all magnets within a family were assigned the same material. However, there were instances where different materials were assigned. This discrepancy can be attributed to the remaining uncertainties in this study, as it was conducted solely within the aperture.

To maintain consistency with real-world conditions, all magnets within the same magnet family were ultimately assigned the same material. This decision is justified by the fact that, for example, in the case of magnets MBPL_110, MBPL_140, MBPL_170, and MBPL_200, only the aperture size varies, while the overall design of the magnets remains identical. Therefore, it is reasonable to use the same material across all four simulation models.

A comparison of the calculated deviations between the old standard material and the newly selected best-fit material reveals that, for nearly all magnets, the use of the new material resulted in a reduction of both the maximum absolute and relative deviations.
Despite the selection of the new materials, a few magnets still show a significant percentage deviation. This is the case for the MBPS_140 and MDS magnet.

There are also magnets, such as MAL, MBPL_170, MDS, MDX_52, QTS and QWL, where the maximum absolute and relative deviations increased with the new material, which may initially seem like a deterioration. However, when examining the total absolute deviation, each of these magnets shows a reduction, indicating an effective improvement in the overall agreement between the simulated and measured BI curves.

In summary, the reassignment of materials for the magnets resulted in a significant reduction in total deviations in the simulation results. The findings of this study demonstrate that using the new materials brings the magnet simulations closer to measured values in the GFR, improving the reliability and efficiency of the simulations.

Tables with detailed information of all magnet models and their assigned materials aswell as the calculated deviations can be found in **Appendix C**.

4.3.1.3 Material Sensitivity Study

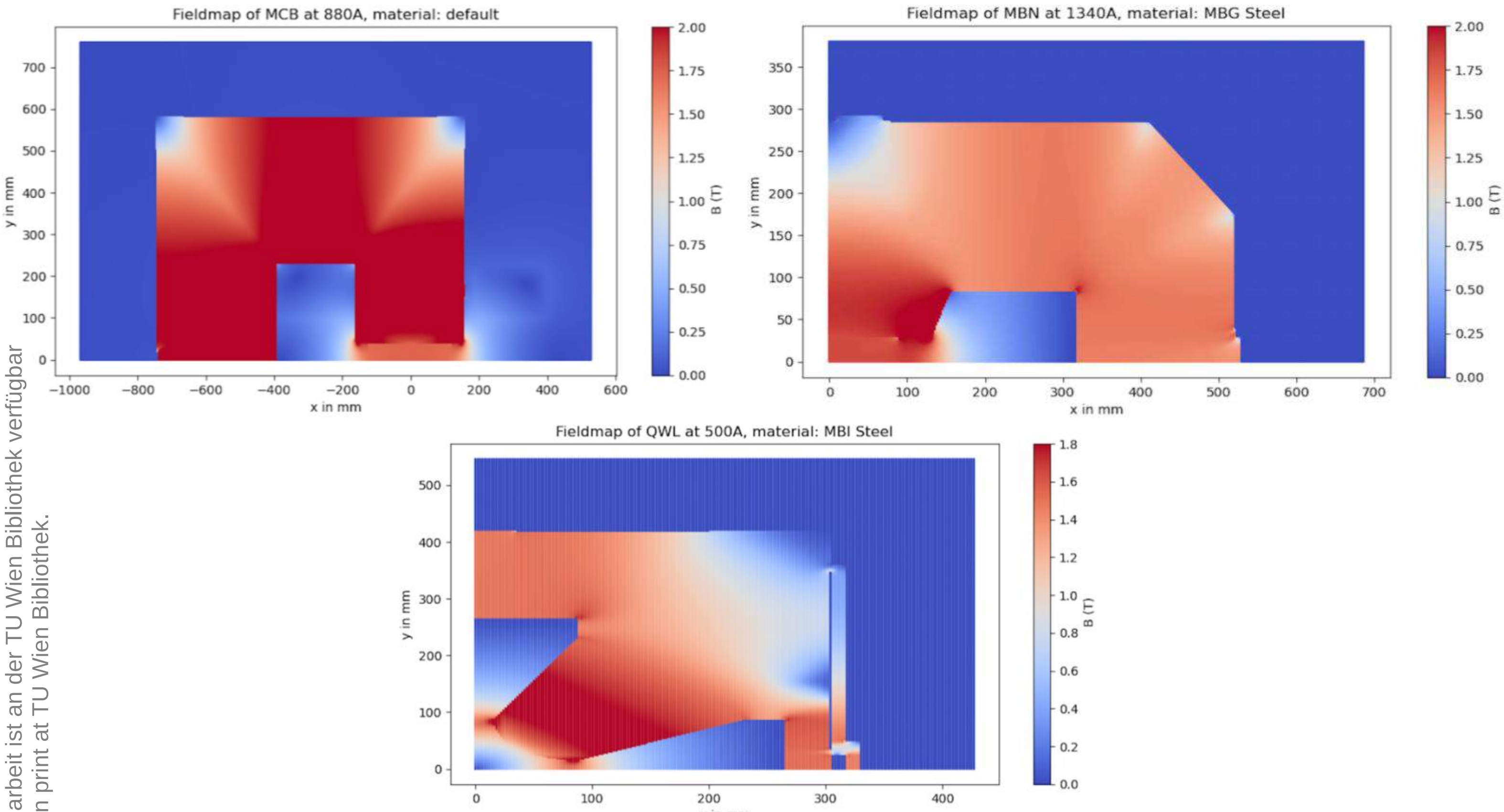

Figure 21: Field maps for a C-shaped dipole, H-shaped dipole and quadrupole

Figure 21 shows the visualization of a field map for a C-shaped dipole (top left), an H-shaped dipole (top right), and a quadrupole (center bottom), representing the three types of magnets considered in this work. These field maps illustrate the 2D distribution and intensity of the magnetic field for the respective magnets, based on the nominal current and the newly assigned material.

Red areas in the field maps indicate strong magnetic fields, while blue areas represent very weak or no magnetic field. High magnetic field strengths are primarily seen around the magnet yoke, shims, and aperture, while lower field strengths are visible in the background and at the outer corners of the magnets.

4.3.1.4 Linear Region

In the following analysis, the MCB magnet (C-shaped dipole) will be used as an example to illustrate the results of the material sensitivity study.

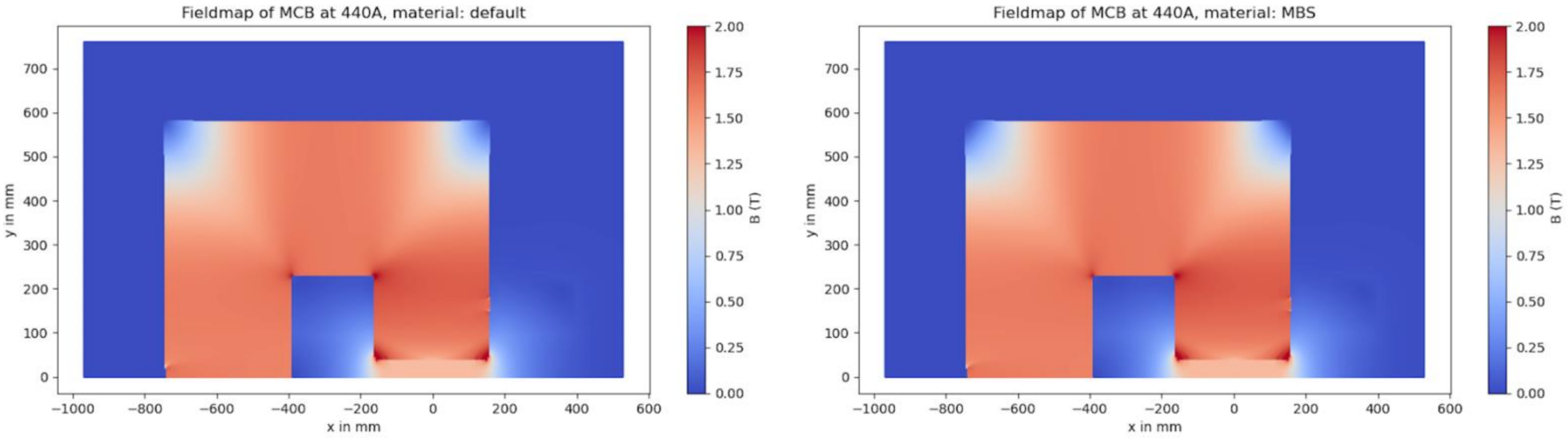

Figure 22: Reference field map with material default (left) and comparison field map with material MBS (right)

The plots in Figure 22 show the reference and comparison field map for the MCB magnet at a current of $I_{lin} = 440$ A. The reference field map is displayed in the left plot of Figure 22 and was generated using the newly assigned material $\mathrm{default}$. The comparison field map, shown in the right plot of Figure 22 was calculated with the old standard material MBS. Both field maps illustrate the distribution and intensity of the computed magnetic field in 2D.

The horizontal and vertical axes range from -1000 mm to 600 mm and from 0 mm to 700 mm, respectively. On the right side of the diagrams, a color scale is located, representing the magnetic field strength B in T, ranging from 0 T (blue) to 1.8 T (red). The upper value of 1.8 T was chosen to be larger than the maximum magnetic field present in the simulation so that the field variations can be fully displayed.

The highest field strengths (shown in dark red) occur in the magnet yoke and at the shims and correspond to a value of 1.73 T. The surrounding areas, transitioning from red to blue, indicate a weakening of the magnetic field, where the blue zones represent the background and denote a weak magnetic field (< 0.2 T).
Both plots show a similar distribution of magnetic field strength, with the magnet yoke and shims in both cases exhibiting the highest field strength. This, at first glance, suggested that the material MBS has similar properties to the material $\mathrm{default}$ regarding magnetic field distribution at the given current.

However, when examining the difference field map, minor distinctions in the field distribution become apparent when comparing the use of the two materials. More detailed insight into the differences in the magnetic field distribution can be obtained by looking at the difference field map in Figure 23.

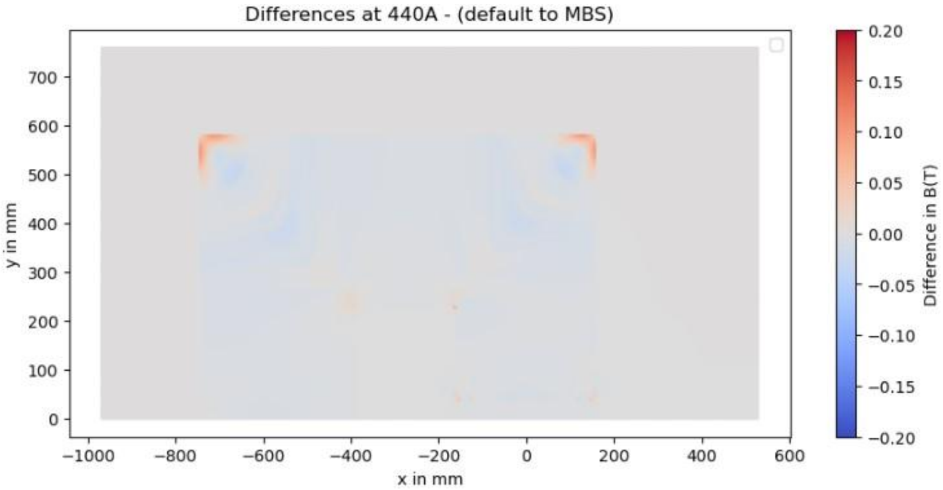

Figure 23: Difference field map using the materials default and MBS at 440 A

This difference field map illustrates the absolute deviations between the given reference and comparison field map at a current of I_{lin} = 440 A. The horizontal axis ranges from -1000 mm to 600 mm, while the vertical axis is given from 0 mm to 700 mm. A color scale on the right displays the absolute difference ΔB in the magnetic field in T, where blue represents negative deviations and red represents positive deviations. Blue coloration means that $B_{comparison} > B_{reference}$ at the given coordinate point, while red indicates $B_{comparison} < B_{reference}$. The range of deviations was set between -0.20 T and +0.20 T to be able to properly see the discolored areas.

The difference field map illustrates that the absolute deviations are minimal or zero in the background, where the magnetic field is generally very weak. This is shown by the predominantly gray areas (ΔB ≈ 0).

The dominant absolute deviations are primarily concentrated in the outer corners of the magnet yoke, around [-700, 500] and [300, 500]. These regions exhibit notable positive deviations (red) and slight negative deviations (blue). The central area of the plot, particularly near the aperture and the magnet yoke close to the coils, shows very small deviations. This indicates that the magnetic field maps in these regions are in good agreement.

Despite the small deviations, particularly in the outer corners of the magnet geometry, it can be concluded that the simulation of the field map for the MCB magnet at a current of $I_{lin} = 440\ A$, in the linear region of the BI curve shows very good agreement when comparing the materials MBS and default.

To determine whether the change between all materials results in a significant difference in the field map within the linear range, a plot was created highlighting all areas within the defined reference region where the set threshold of ΔB > 0.1 T is exceeded.

The corresponding reference region for the MCB magnet and the plots comparing each material to the reference material are shown in Figure 24.

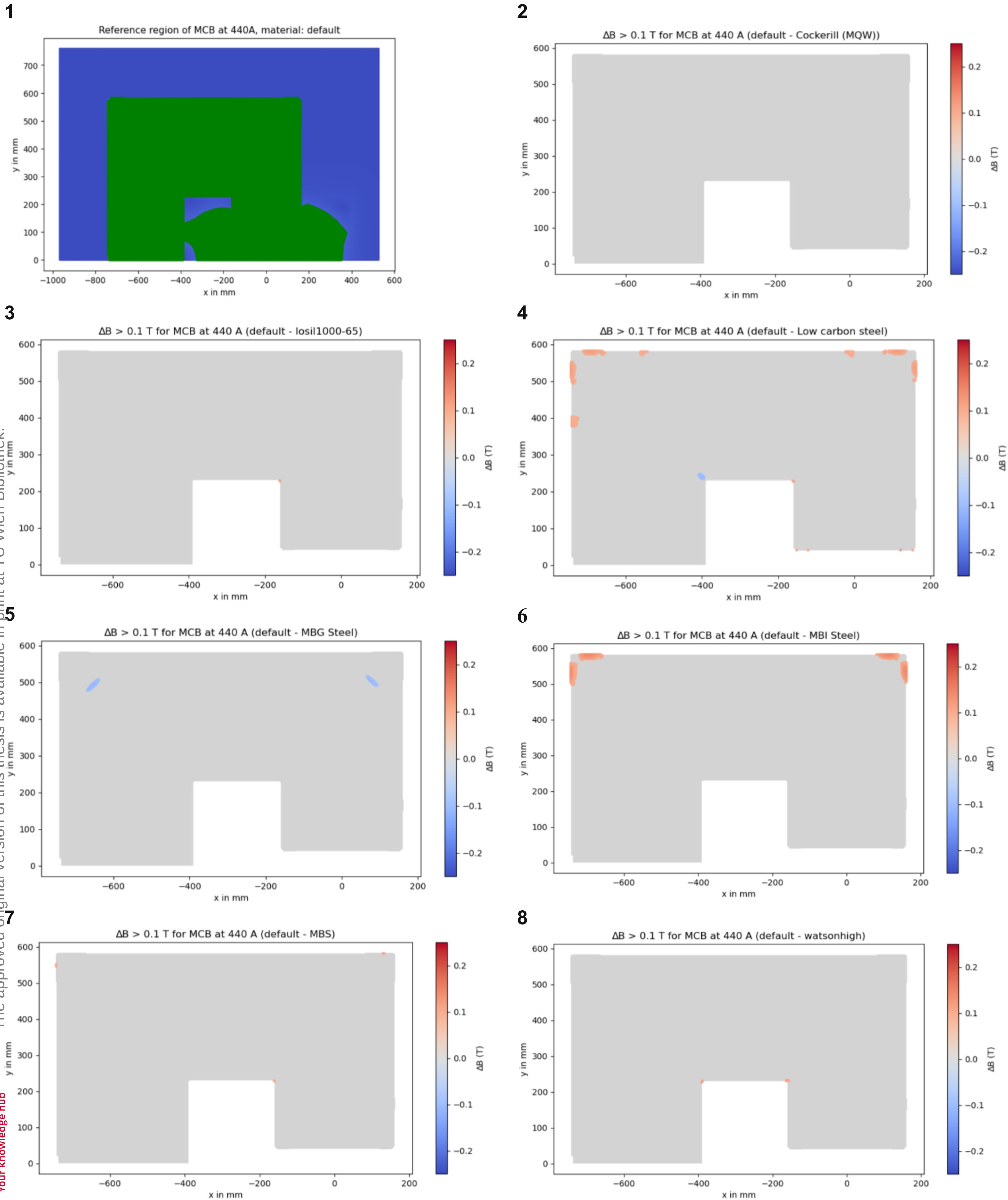

Figure 24: Difference field maps of the MCB magnet for all materials with areas that exceed the threshold at 440 A

All plots in Figure 24 refer to the same reference material, default and the same current of $I_{lin} = 440$ A.
In plots 2–8, only regions where the magnetic field deviation, ΔB, exceeds the threshold of ± 0.1 T are emphasized:

- Positive deviations ($\Delta B \geq 0.1\ T$) are displayed using a red gradient, with darker red shades indicating larger positive deviations.
- Negative deviations ($\Delta B \leq 0.1\ T$) are represented by a blue gradient, with darker blue tones corresponding to larger negative deviations.

Regions where the absolute deviation is less than the threshold ($-0.1\ T\ \leq \Delta B \leq 0.1\ T$) are shown in gray, indicating that these deviations fall within the acceptable range and are not considered significant for the analysis.

In all seven comparison field map plots, it can be observed that there are only a few small regions where the threshold is exceeded. The areas where the threshold is surpassed are located either at the inner or outer corners, which are regions with sharp transitions. These are not critical areas and a slight exceedance, as seen here, would not create any significant issues.
Based on analysis of these plots, it can be concluded that for the MCB magnet at a current of $I_{lin} = 440$ A, within the linear range, a material change between the eight different materials does not have a significant impact on the calculated field map. Therefore, the MCB magnet is not sensitive to material variations in the linear range.

4.3.1.5 Saturation Region

The plot in Figure 25, again, shows the difference field map for the MCB magnet, comparing the new standard material default and the old standard material MBS, this time at the maximal operation current of the MCB, I_{sat}= 880 A, representing the saturation region of its BI curve.

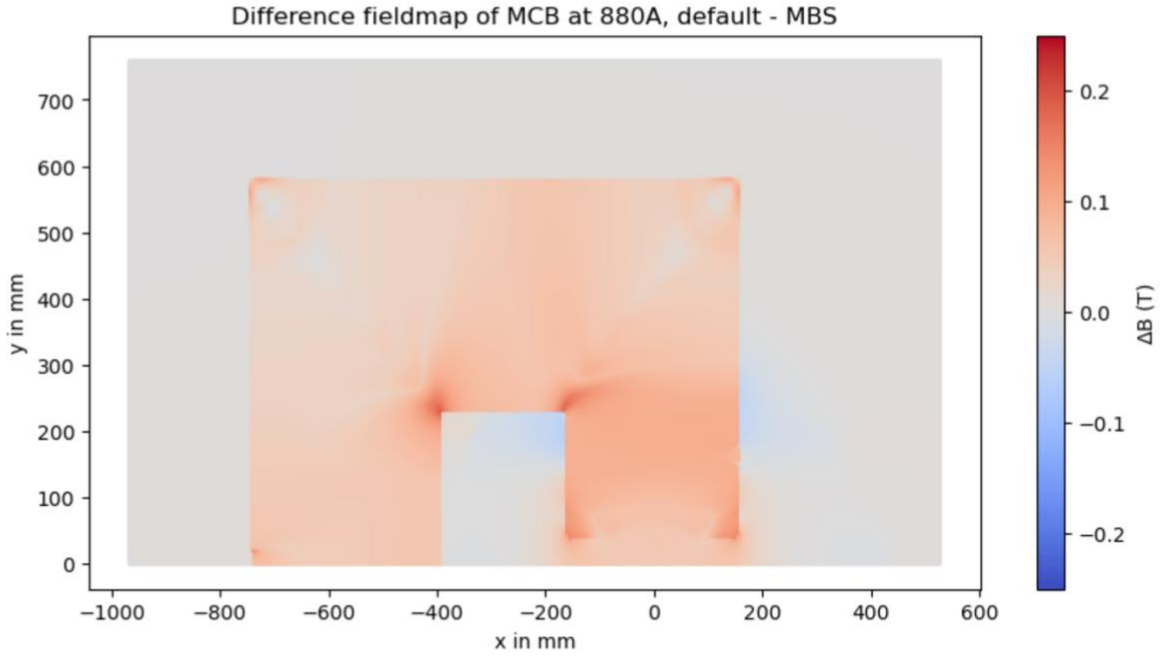

Figure 25: Difference field map of the MCB magnet using the materials default and MBS at I_{sat}= 880 A

When comparing the difference field maps at I_{lin} and I_{sat} (Figure 23 and Figure 25), it becomes evident that the differences in magnetic field distribution between the materials default and MBS increase with higher current. In contrast to the plot at I_{lin}, where deviations were primarily localized in the outer corners, the plot at I_{sat} shows widespread deviations across the entire magnet yoke and aperture.

Particularly striking are the deviations in the inner corners of the magnet yoke and at the shims, where significant positive deviations (red) of more than +0.20 T are observed. At the same time, notable negative deviations (blue) are present outside the magnet yoke in the region of the coils.

The comparison of the two plots also shows that while the field maps exhibit very good agreement in the linear range, the deviations increase significantly in the saturation region. This increase in deviations can be traced back to the different saturation behaviors of the materials used, further emphasizing the importance of this material study.

To gain deeper insight into the magnetic field behavior in the saturation region across all different materials within the entire magnet geometry, the analysis previously done at I_{lin}= 440 A was performed again, this time at I_{sat}= 880 A using all available materials.

The results are shown in Figure 26 and all plots, again, refer to the same reference material, default, and current I_{sat}.

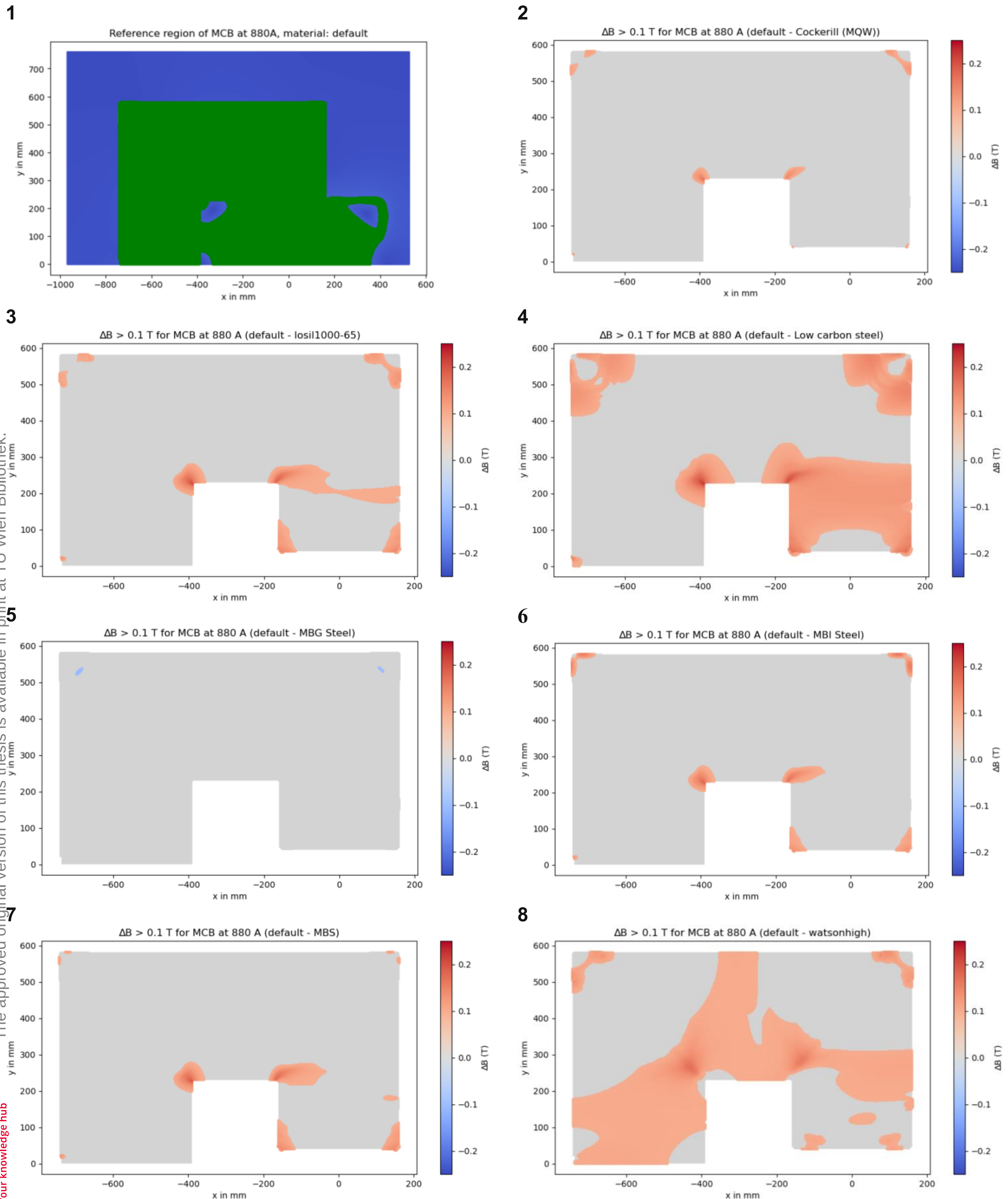

Figure 26: Difference field maps of the MCB magnet for all materials with areas that exceed the threshold at 880 A

When analyzing the difference field maps of the MCB magnet for all materials, it is clear that there are many more and larger regions where ΔB exceeds the 0.1 T threshold. These regions are not only larger but also occur in areas where no exceedance was observed at I_{lin}, such as in the region of the shims and the magnet yoke itself. Furthermore, clear differences between materials can be identified. For instance, while the comparison between default and MBG steel shows almost no exceedances, the comparison between default and Low Carbon Steel or Watsonhigh reveals widespread exceedances across the entire magnet yoke and the shims.

This indicates that, depending on the saturation behavior of each material, the magnetic field at higher currents undergoes significant changes. The areas where the threshold is exceeded are no longer confined to the outer and inner corners, where they can be discounted. Instead, for certain materials, these exceedances occur in critical regions, such as the magnet yoke or particularly around the shims. As a result, the choice of material for simulating the magnet becomes crucial.

Given these findings, it can be concluded that the MCB magnet simulation model at $I_{sat} = 880$ A is sensitive to material changes.

The maximum absolute difference, as well as the percentage of deviations exceeding the threshold within the reference region for the MCB magnet, are presented in Table 9. The reference material used as the baseline is default.

	Linear Region I_{lin}		**Saturation Region I_{sat}**	
Material	**Max. absolute. Difference [T]**	**Deviation [%]**	**Max. absolute. Difference [T]**	**Deviation [%]**
Cockerill (MQW)	0.097	0.00	0.163	0.60
Iosil1000-65	0.106	0.002	0.205	4.46
Low Carbon Steel	0.125	0.48	0.221	21.55
MBG Steel	0.110	0.09	0.110	0.03
MBI Steel	0.146	0.52	0.180	1.85
MBS	0.105	0.007	0.193	2.53
watsonhigh	0.122	0.008	0.171	32.53
# of exceedances		0		5

Table 9: Absolute and relative deviations exceeding the threshold within the reference region for the MCB magnet in the linear and saturation region

This analysis was done for every magnet at the two defined currents for the linear and the saturation region I_{lin} and I_{sat}. It revealed that significant differences in the magnetic behavior of the various materials occur, especially in the saturation region.

Table 10 presents, for every magnet model, the number of materials for which the difference field map exceeds the threshold of 0.1 T by more than 1%. The maximum number (#) of exceedance is 7, which means that using every other material compared to the used best-fit standard material would lead to a non-negligible change in the magnetic field. A table with all values calculated for each magnet can be found in **Appendix D**.

Magnet	**# exceedance lin. Reg.**	**# exceedance sat. Reg.**
MAL	1	1
MBE	1	0
MBN	5	2
MBPL_110	1	3
MBPL_140	0	5
MBPL_170	1	2
MBPL_200	1	1
MBPS_140	1	3

MBW	0	1
MCA	2	1
MCB	0	5
MCV	3	1
MCVS	1	1
MCW	1	3
MDA	-	-
MDL	1	1
MDS	1	1
MDP	0	0
MDX_100	0	1
MDX_80	1	0
MDX_52	1	2
MPLS	0	0
MSN	3	2
MTN	3	2
MTR	5	3
QFS	1	1
QM	-	-
QNLB	5	3
QNL	7	7
QNRB	3	5
QPL	1	1
QPS	1	1
QSL	4	5
QTA	6	7
QTL	6	5
QTS	5	5
QWL	7	4

Table 10: Number of materials for which the difference field map exceeds the threshold of 0.1 T by more than 1%

5 Reliability Statement

The assessment of uncertainties in the magnetic field simulations conducted is essential to ensure the reliability of the results. This section introduces an approach for the quantitative evaluation of known sources of error. The method involves assigning scores by weighting the error sources and calculating an overall uncertainty value for each simulation model.

5.1 Methodology

5.1.1 Definition of Error Sources and their Weighting

The potential error sources defined below are assigned specific weighting factors to account for their relative significance in the reliability of each magnet model. The following error sources were identified.

5.1.1.1 Geometry Inaccuracies (G1)

The reconstruction of the magnet geometry, often based on incomplete or outdated documentation, represents a significant source of uncertainty. These inaccuracies may affect the simulation results, particularly in regions with complex geometries, such as the shims.

5.1.1.2 Availability and Reliability of BI Curves (B1)

The measured BI curves, which served as reference data for the simulations, may be outdated or inaccurate, leading to additional uncertainties in evaluating the simulation results. This is particularly relevant for measurements documented in the 1960s or 1970s, where the precision of the original measurements is uncertain.

5.1.1.3 Consistency of BI Curves in the Validation Plot (V1)

To evaluate the consistency of the BI curves, the total absolute deviation between the measured BI curve and each BI curve simulated using the best-fit material, as previously calculated in 4.2.1.1, was utilized. Based on the magnitude of this deviation, an uncertainty score was assigned to each magnet model.

5.1.1.4 Material Uncertainty and Sensitivity to Material Changes (M1)

The material composition of the magnet yoke was unknown and therefore had to be substituted with materials available in the database. This material uncertainty may lead to deviations between the simulated and actual magnetic fields, particularly in regions outside the aperture where material behavior may differ. Through the analysis of the difference field maps, it was determined whether a magnet model exhibits sensitivity to material changes, either in the linear or saturation range.

5.1.2 Assignment of Scores for each Error Source

Each error source is assigned a score between 0 and 5, where 0 represents no uncertainty, and 5 indicates maximum uncertainty. The scores are based on detailed analysis of the specific uncertainty associated with each magnet.

5.1.3 Determination of Weighting Factors

Weighting factors (WF) are assigned based on the relative importance of each error source, ensuring that the overall uncertainty reflects the significance of the respective sources of error.

Error Source	Weighting Factor (WF)
G1	0.4
B1	0.1
V1	0.2

M1	0.3

Table 11: Weighting factors assigned to error sources

5.1.4 Calculation of the Overall Uncertainty Value (U):

The overall uncertainty value is calculated as a weighted average of the individual scores. The formula for this calculation is as follows:

$$U = \sum (W_i * S_i)$$

where W_i is the weighting factor of each error source, and S_i is the score assigned to the corresponding error source.

The lower the uncertainty value U of a model, the more reliable it is at representing the magnetic field. Models with a U value below a defined threshold of 2.5 can thus be considered precise enough and trustworthy, as they are capable of accurately simulating the magnetic behavior of the real magnet.

In contrast, magnetic models with higher uncertainty values that exceed the threshold, exhibit greater deviations from the real behavior of the magnet, which calls into question their exact reliability. These models should be used with caution, as their predictions may be more inaccurate and they do not provide an exact representation of the real magnetic behavior.

This uncertainty threshold of 2.5 is a good balance between the complexity of the simulations and the need for accurate field representations. By choosing a U value of 2.5, the model ensures that any deviations remain within acceptable limits, while taking into account the partly incomplete and inaccurate documentation available.

5.2 Results

In Table 12, the U values for all dipole magnet simulation models are listed, while Table 13 presents the U values for the quadrupole models. The dipole models were successfully created with such precision that for all models the U value remains below the critical threshold of U = 2.5. This high level of accuracy was also achieved for nearly all quadrupole models, with the exceptions of QFS, QPS and QTA, whose U values slightly exceed 2.5. These results indicate that the simulation models developed in this work provide a reliable foundation for the generation of field maps.

Magnet	U
MAL	0.31
MBE	0.81
MBN	0.95
MBPL_110	1.63
MBPL_140	1.53
MBPL_170	0.82
MBPL_200	0.71
MBPS_140	1.93
MBW	0.93
MCA	0.32
MCB	0.54
MCV	0.21
MCVS	0.43
MCW	2.13
MDL	0.31

MDS	0.51
MDP	1.3
MDX_100	0.4
MDX_80	0.71
MDX_52	0.92
MPLS	0.6
MSN	0.54
MTN	0.54
MTR	0.73

Table 12: Uncertainty values for all dipole simulation models

Magnet	U
QFS	2.61
QNLB	1.66
QNL	2.1
QNRB	1.46
QPL	2.41
QPS	2.81
QSL	1.56
QTA	2.79
QTL	1.56
QTS	1.67
QWL	1.58

Table 13: Uncertainty values for all quadrupole simulation models

6 Conclusion

This thesis developed a simulation code capable of reliably simulating both dipole and quadrupole geometries and calculating their corresponding field maps. The strength of the code lies in its universal design, allowing it to simulate any dipole or quadrupole configuration by using magnet-specific input files. These input files contain all the parameters for each magnet, meaning changes to the magnetic geometry or properties can be made easily without altering the main code itself. This setup not only simplifies the use of the code but also ensures its security by preventing unintentional modifications to the core simulation framework.

The reliability of the simulations was thoroughly tested and confirmed. The simulated models accurately represented real-world magnet behavior within an acceptable deviation range, proving the robustness of the approach developed. However, one important observation was the sensitivity of the simulations to changes in material properties. While a best-fit material was selected for each model, this does not guarantee a perfect match with real-world materials. Even small variations in material properties could affect the results, so future simulations should always account for this uncertainty to maintain high accuracy.

One major achievement of this work is the ability to generate highly accurate field maps, which can now be used in beamline simulations. This allows for simulations with the highest possible precision based on the available input data, greatly improving the potential for accurate beamline designs. It should be noted that the evaluation of reliability incorporates subjective judgments and personal assessments, which ultimately influenced the conclusions drawn. This consideration should be kept in mind when interpreting the findings.

However, a limitation in the current approach is that the field maps are only two-dimensional. While these 2D simulations are sufficient for many applications, extending them to three dimensions would provide a more complete understanding of the magnetic field distribution.

This would be particularly useful for more complex magnet configurations, where 3D field information could offer deeper insights that 2D simulations cannot capture.

In summary, this thesis has successfully developed a flexible and reliable simulation framework for dipole and quadrupole magnets. The system is both precise and adaptable, making it a valuable tool for future research. Moving forward, addressing the sensitivity to material properties and expanding the simulations to three dimensions will further enhance the capabilities of this framework for studying magnetic systems.

7 Table of Figures

8 List of tables

9 Bibliography

[1] C. Benvenuti, R. Calder, and O. Gröbner, “Vacuum for particle accelerators and storage rings,” *Vacuum*, vol. 37, no. 8, pp. 699–707, Jan. 1987, doi: 10.1016/0042-207X(87)90057-1.

[2] J. He *et al.*, “Design and optimization of a Goubau line for calibration of BPMs for particle accelerators,” *Nuclear Instruments and Methods in Physics Research Section A: Accelerators, Spectrometers, Detectors and Associated Equipment*, vol. 1045, p. 167635, Jan. 2023, doi: 10.1016/j.nima.2022.167635.

[3] R. I. Gilmer, F. D. Neu, R. J. Sprafka, and J. E. Strople, “PARTICLE-BEAM PROFILING SYSTEM,” Oct. 1966, Accessed: Jan. 21, 2025. [Online]. Available: https://escholarship.org/uc/item/5s8255ph

[4] D. Banerjee *et al.*, “M2 Experimental Beamline Optics Studies for Next Generation Muon Beam Experiments at CERN,” *Proceedings of the 12th International Particle Accelerator Conference*, vol. IPAC2021, p. 4 pages, 0.598 MB, 2021, doi: 10.18429/JACOW-IPAC2021-THPAB143.

[5] L. J. Nevay *et al.*, “BDSIM: An accelerator tracking code with particle–matter interactions,” *Computer Physics Communications*, vol. 252, p. 107200, Jul. 2020, doi: 10.1016/j.cpc.2020.107200.

[6] S. Russenschuck, “DESIGN OF ACCELERATOR MAGNETS”.

[7] T. Zickler, “Basic design and engineering of normal-conducting, iron-dominated electromagnets,” Mar. 06, 2011, *arXiv*: arXiv:1103.1119. doi: 10.48550/arXiv.1103.1119.

[8] B. Holzer, “Lattice Design in High-energy Particle Accelerators,” 2014, *CERN*. doi: 10.5170/CERN-2014-009.61.

[9] CERN intern communication

[10] “Welcome to BDSIM’s documentation! — BDSIM 1.7.7 documentation.” Accessed: Jan. 21, 2025. [Online]. Available: https://www.pp.rhul.ac.uk/bdsim/manual/

[11] “Magnetic Field Mapping,” in *ResearchGate*. Accessed: Jan. 21, 2025. [Online]. Available: https://www.researchgate.net/publication/227573497_Magnetic_Field_Mapping

[12] “Opera | SIMULIA von Dassault Systèmes.” Accessed: Jan. 21, 2025. [Online]. Available: https://www.3ds.com/de/produkte-und-services/simulia/produkte/opera/

[13] “Ansys | Engineering Simulation Software.” Accessed: Jan. 21, 2025. [Online]. Available: https://www.ansys.com/

[14] G. L. D’Alessandro *et al.*, “Target Bypass Beam Optics for Future High Intensity Fixed Target Experiments in the CERN North Area,” *Proceedings of the 12th International Particle Accelerator Conference*, vol. IPAC2021, p. 3 pages, 0.663 MB, 2021, doi: 10.18429/JACOW-IPAC2021-WEPAB185.

[15] L. Gatignon *et al.*, "Design and Tuning of Secondary Beamlines in the CERN North and East Areas" CERN, Geneva, Switzerland, CERN-ACC-NOTE-2020-0043, 2020. [Online]. Available: https://cds.cern.ch/record/2730780/files/CERN-ACC-NOTE-2020-0043.pdf [Accessed: Jan. 21, 2025].

[16] H.W. Atherton, C. Bovet, N. Doble, G. von Holtey, L. Piemontese, A. Placci, M. Placidi, D.E. Plane, M. Reinharz and E. Rossa., "Precise measurements of particle production by 400 GeV/c protons on beryllium targets" CERN, Geneva,

Switzerland, CERN-80-07, 1980. [Online]. Available: https://cds.cern.ch/record/133786/files/CERN-80-07.pdf [Accessed: Jan. 21, 2025].

[17] S. Izquierdo Bermudez, G. Sabbi, and A. Zlobin, "Accelerator Technology - Magnets," FERMILAB-FN-1208-TD, arXiv:2208.13349, 1898869, Aug. 2022. doi: 10.2172/1898869.

[18] D. Banerjee *et al.*, "Addendum to the Proposal P348: Search for dark sector particles weakly coupled to muon with NA64μ".

[19] A. Milanese, "An introduction to Magnets for Accelerators".

[20] M. Mahran, A. ELsabbagh, and H. Negm, "A comparison between different finite elements for elastic and aero-elastic analyses," *Journal of Advanced Research*, vol. 8, no. 6, pp. 635–648, Nov. 2017, doi: 10.1016/j.jare.2017.06.009.

[21] M. Hazim and J. Aziz, "Design and Simulation of an Enhanced Bandwidth Microstrip Antenna Using Metamaterial," *IJCSET(www.ijcset.net)*, Dec. 2015.

[22] "Boundary Conditions." Accessed: Jan. 21, 2025. [Online]. Available: https://www.iue.tuwien.ac.at/phd/milovanovic/diss_htmlse6.html

[23] "Neumann Boundary Condition," Resolved Analytics. Accessed: Jan. 21, 2025. [Online]. Available: https://www.resolvedanalytics.com/cfd/what-is-a-neumann-boundary-condition

[24] "What is Finite Element Analysis (FEA)? | Ansys." Accessed: Jan. 21, 2025. [Online]. Available: https://www.ansys.com/simulation-topics/what-is-finite-element-analysis

[25] H. E. Nigh, "Magnetization and electrical resistivity of gadolinium single crystals," Doctor of Philosophy, Iowa State University, Digital Repository, Ames, 1963. doi: 10.31274/rtd-180814-4593.

[26] "Magnetic saturation," Questions and Answers in MRI. Accessed: Jan. 21, 2025. [Online]. Available: http://mriquestions.com/magnetizing-metal.html

[27] M. D. Hossain, M. A. Hossain, and S. S. Sikder, "Hysteresis loop properties of rare earth doped spinel ferrites: A review," *Journal of Magnetism and Magnetic Materials*, vol. 564, p. 170095, Dec. 2022, doi: 10.1016/j.jmmm.2022.170095.

[28] "Nondestructive Evaluation Physics : Magnetism." Accessed: Jan. 21, 2025. [Online]. Available: https://www.nde-ed.org/Physics/Magnetism/HysteresisLoop.xhtml

[29] "12.3: Magnetization and Susceptibility," Physics LibreTexts. Accessed: Jan. 21, 2025. [Online]. Available: https://phys.libretexts.org/Bookshelves/Electricity_and_Magnetism/Electricity_and_Magnetism_(Tatum)/12%3A_Properties_of_Magnetic_Materials/12.03%3A_Magnetization_and_Susceptibility

[30] L. N. Mulay, "Basic Concepts Related to Magnetic Fields and Magnetic Susceptibility," in *Biological Effects of Magnetic Fields*, M. F. Barnothy, Ed., Boston, MA: Springer US, 1964, pp. 33–55. doi: 10.1007/978-1-4899-6578-3_3.

[31] S. W. Contributors, "Spyder | The Python IDE that scientists and data analysts deserve," Spyder IDE. Accessed: Jan. 21, 2025. [Online]. Available: https://www.spyder-ide.org

[32] "Project Jupyter." Accessed: Jan. 21, 2025. [Online]. Available: https://jupyter.org

[33] "Fig. 1. Epstein frame and single sheet tester to determine magnetic...," ResearchGate. Accessed: Jan. 21, 2025. [Online]. Available: https://www.researchgate.net/figure/Epstein-frame-and-single-sheet-tester-to-determine-magnetic-properties-and-iron-losses-in_fig1_274384051

[34] “Fig. 4. BH hysteresis loops from Epstein frame test and ring core...,” ResearchGate. Accessed: Jan. 21, 2025. [Online]. Available: https://www.researchgate.net/figure/BH-hysteresis-loops-from-Epstein-frame-test-and-ring-core-measurements-before-and-after_fig4_234217985

[35] T. D. T. Oyedotun, “X-ray fluorescence (XRF) in the investigation of the composition of earth materials: a review and an overview,” *Geology, Ecology, and Landscapes*, vol. 2, no. 2, pp. 148–154, Apr. 2018, doi: 10.1080/24749508.2018.1452459.

[36] P. J. Potts and M. Sargent, “In situ measurements using hand-held XRF spectrometers: a tutorial review,” *J. Anal. At. Spectrom.*, vol. 37, no. 10, pp. 1928–1947, Oct. 2022, doi: 10.1039/D2JA00171C.

[37] Z. Zhou, K. Zhou, X. Hou, and H. Luo, “Arc/Spark Optical Emission Spectrometry: Principles, Instrumentation, and Recent Applications,” *Applied Spectroscopy Reviews*, vol. 40, no. 2, pp. 165–185, May 2005, doi: 10.1081/ASR-200052001.

10 Appendix

10.1 Appendix A

All materials used in the studies and their BH curve values.

Cockerill (MQW)		default		losil1000-65		Low carbon steel		MBG steel		MBI steel		MBS		watsonhight	
B	H	B	H	B	H	B	H	B	H	B	H	B	H	B	H
0	0	0	0	0	0	0	0	0	0	0	0	0	0	0	0
0.41	60.5	0.64	7.95	0.5	95	0.05	61	0.18	40	0.018	17.9	0.01	6.36	0.5	7.957
0.68	81.3	0.92	13.52	0.8	152	0.1	94	0.47	60	0.02	24.6	0.01	7.95	1	15.915
0.92	109.7	1.01	15.91	1	190	0.15	114	0.98	120	0.05	39.6	0.02	13.26	1.22	23.873
1.11	148.5	1.1	19.09	1.1	220	0.2	133	1.41	500	0.07	44.8	0.06	20.75	1.33	31.830
1.24	200	1.2	23.87	1.2	260	0.25	147	1.56	1200	0.13	60.5	0.1	26.52	1.39	39.788
1.35	270.2	1.3	31.83	1.3	340	0.3	159	1.62	2500	0.29	81.3	0.27	39.78	1.45	55.703
1.43	364.2	1.4	49.33	1.35	400	0.35	174	1.71	5000	0.55	109.7	0.3	40.80	1.51	79.577
1.48	489.6	1.45	64.47	1.4	480	0.4	187	1.83	10000	0.78	148.5	0.4	47.50	1.57	159.15
1.53	659.7	1.5	87.53	1.45	610	0.45	205	2.06	24000	0.96	200	0.5	56.04	1.62	238.73
1.56	889.6	1.55	127.32	1.5	830	0.5	221	2.12	30000	1.10	270.2	0.58	63.65	1.67	397.88
1.59	1191.1	1.575	159.15	1.55	1300	0.55	237			1.22	364.2	0.65	71.34	1.72	636.61
1.59	1200.1	1.6	214.85	1.6	2000	0.6	258			1.31	489.6	0.71	79.57	1.77	954.92
1.62	1618	1.65	334.22	1.65	3000	0.65	280			1.39	659.7	0.85	99.47	1.82	1353.8
1.65	2179.2	1.7	477.46	1.7	4400	0.7	309			1.45	889.6	0.98	127.32	1.87	1907.8
1.68	2937.5	1.75	652.53	1.75	6100	0.75	332			1.50	1191	1.09	159.16	1.97	3650.5
1.72	3964.4	1.8	914.14	1.8	8300	0.8	364			1.51	1200	1.26	238.75	2.1	6366.1
1.75	5349.5	1.85	1193.66	1.85	10800	0.85	398			1.55	1618	1.35	318.33	2.2	11141
1.80	7212.3	1.9	1514.97	1.9	13800	0.9	448			1.59	2179	1.40	397.94	2.3	15916
1.85	9696	1.95	1853.70	1.95	17600	0.95	488			1.63	2938	1.48	636.79		
1.91	13087.2	2	2227.76	2	22000	1	531			1.67	3964	1.55	1193.4		
1.98	17577	2.05	2745.27	2.02	30000	1.05	597			1.71	5350	1.62	2388.0		
2.05	24225.1	2.1	3580.98			1.1	673			1.76	7212	1.68	3985.0		
		2.15	4774.64			1.15	732			1.81	9695	1.78	7969.3		
		2.2	6366.19			1.2	830			1.87	13090	1.85	11927.6		
		2.25	9388.12			1.25	947			1.94	17580	2.01	23926.6		
		2.3	12732.38			1.3	1089			2.02	23879.9				
						1.35	1264								
						1.4	1485								
						1.45	1775								
						1.5	2170								
						1.55	2597								
						1.6	3183								
						1.65	4040								
						1.7	5203								
						1.75	6963								
						1.8	8952								
						1.85	11324								
						1.9	15120								
						1.95	20690								
						2	31831								

10.2 Appendix B

Validation plots of all magnets simulated in the thesis.

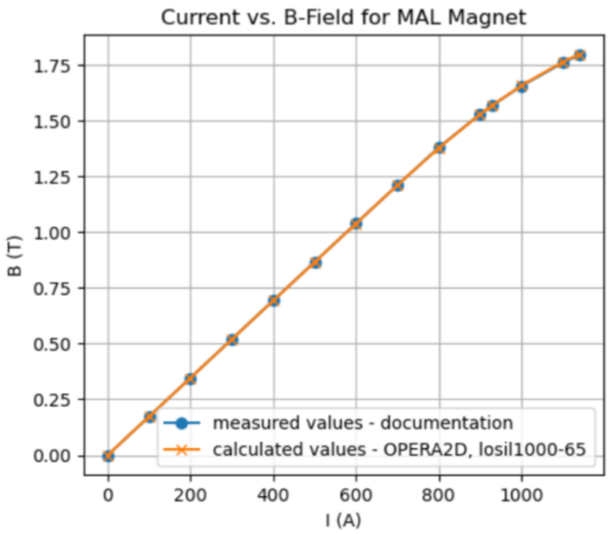

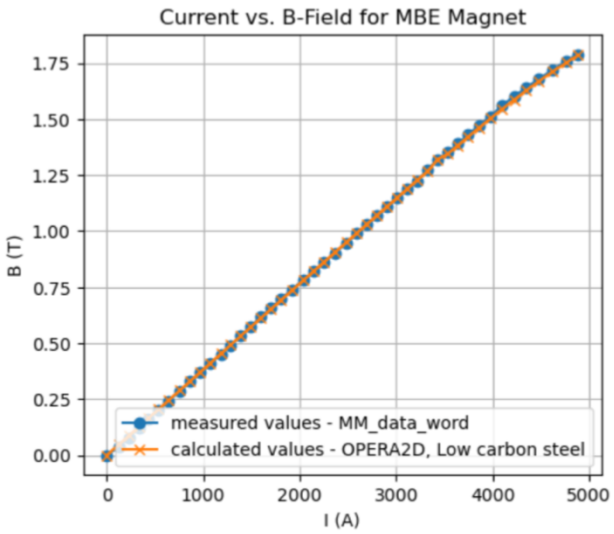

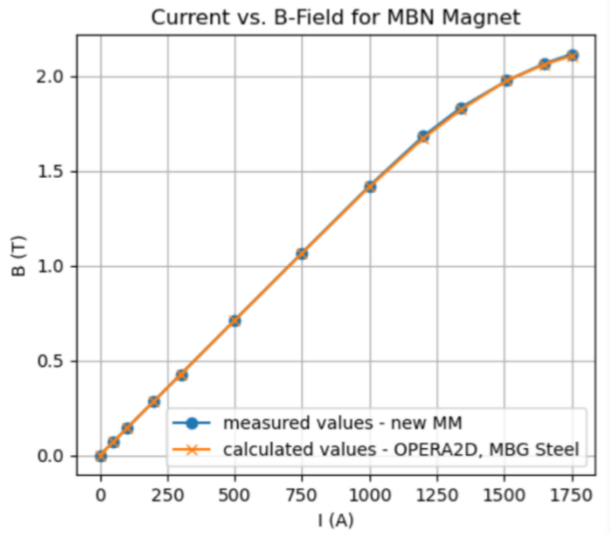

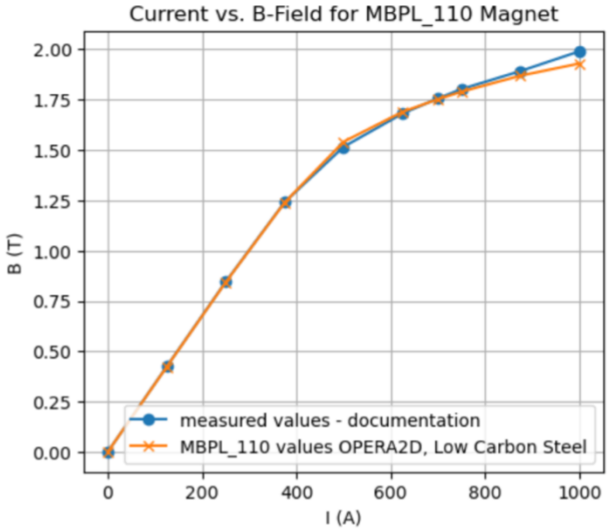

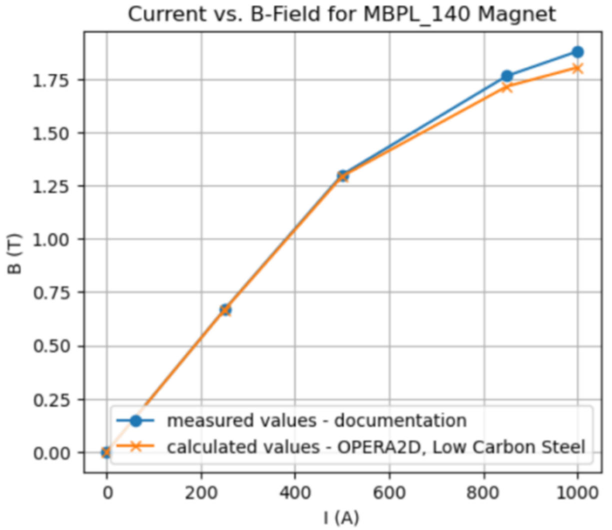

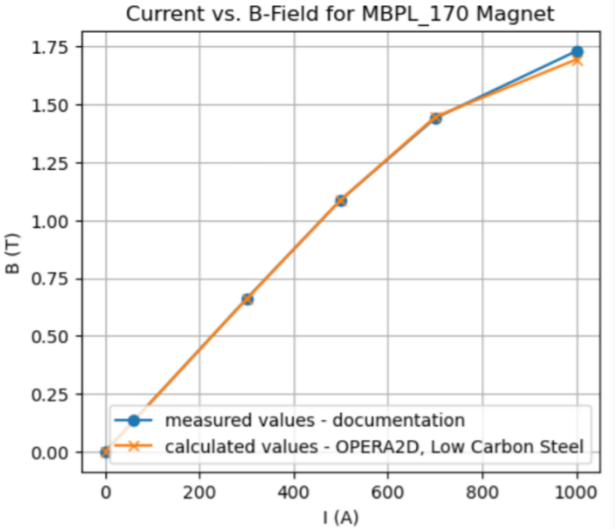

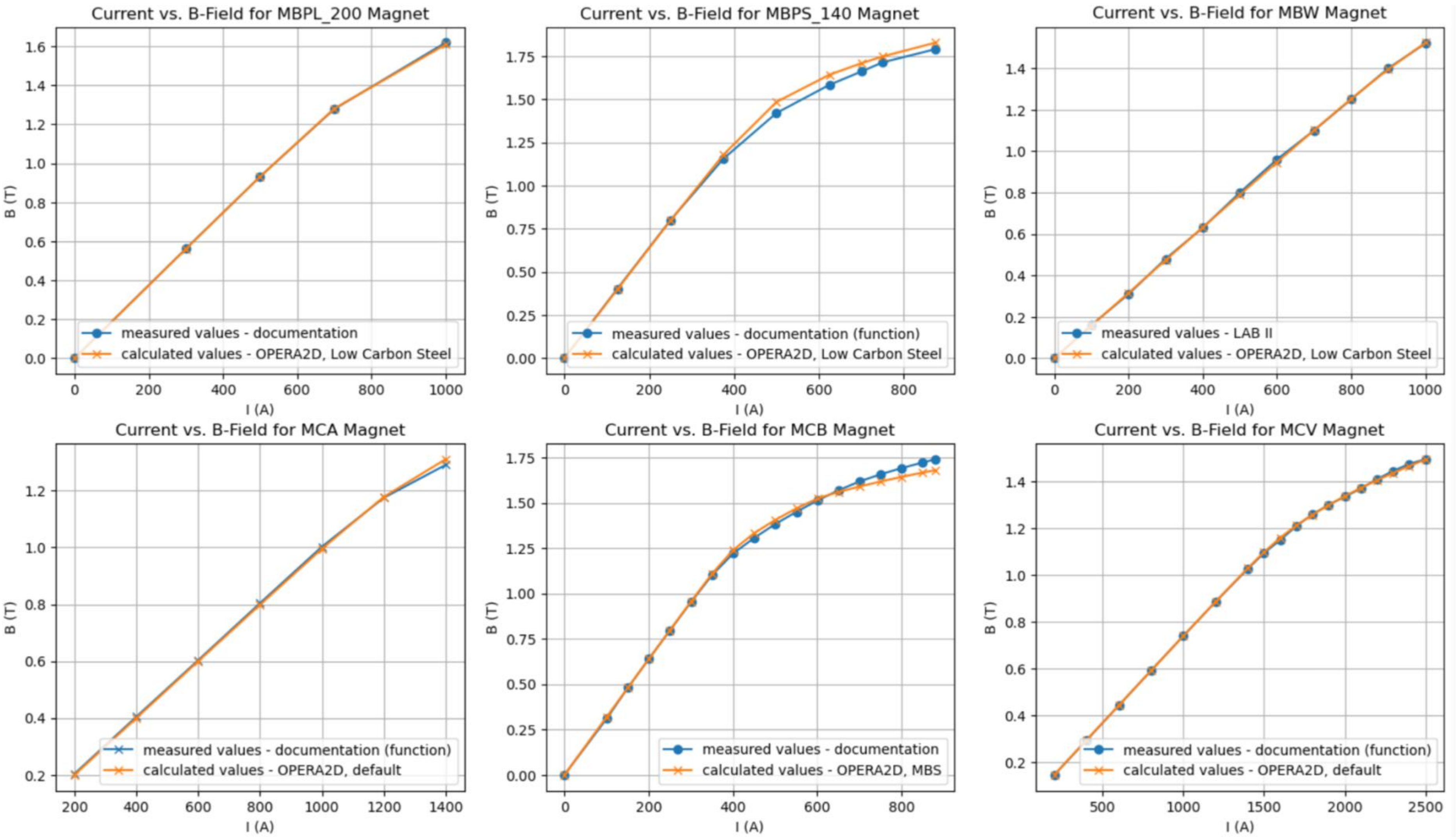
Current vs. B-Field for MBPL_200 Magnet
B (T)
I (A)
measured values - documentation
calculated values - OPERA2D, Low Carbon Steel
Current vs. B-Field for MBPS_140 Magnet
B (T)
I (A)
measured values - documentation (function)
calculated values - OPERA2D, Low Carbon Steel
Current vs. B-Field for MBW Magnet
B (T)
I (A)
measured values - LAB II
calculated values - OPERA2D, Low Carbon Steel
Current vs. B-Field for MCA Magnet
B (T)
I (A)
measured values - documentation (function)
calculated values - OPERA2D, default
Current vs. B-Field for MCB Magnet
B (T)
I (A)
measured values - documentation
calculated values - OPERA2D, MBS
Current vs. B-Field for MCV Magnet
B (T)
I (A)
measured values - documentation (function)
calculated values - OPERA2D, default

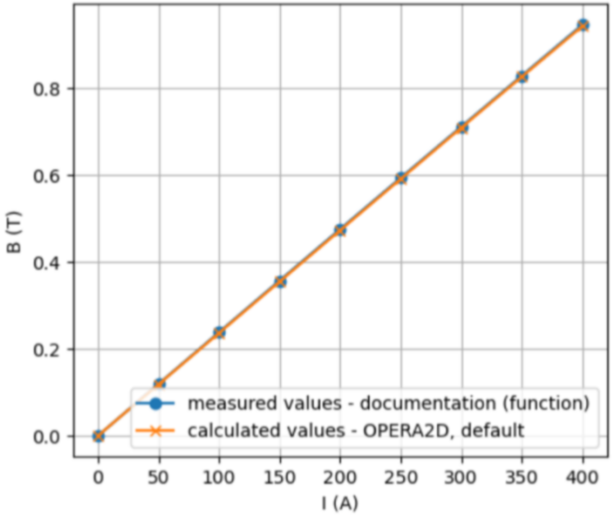
Current vs. B-Field for MCVS Magnet

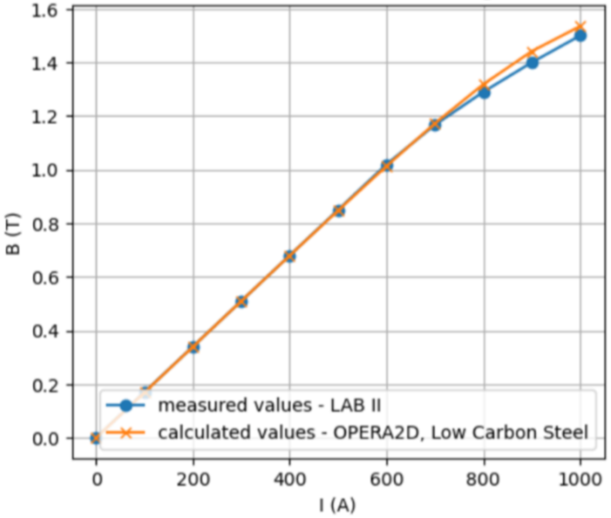
Current vs. B-Field for MCW Magnet

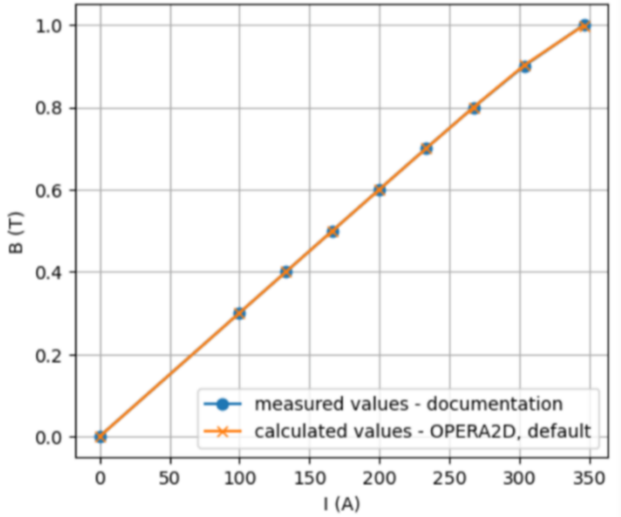
Current vs. B-Field for MDL Magnet

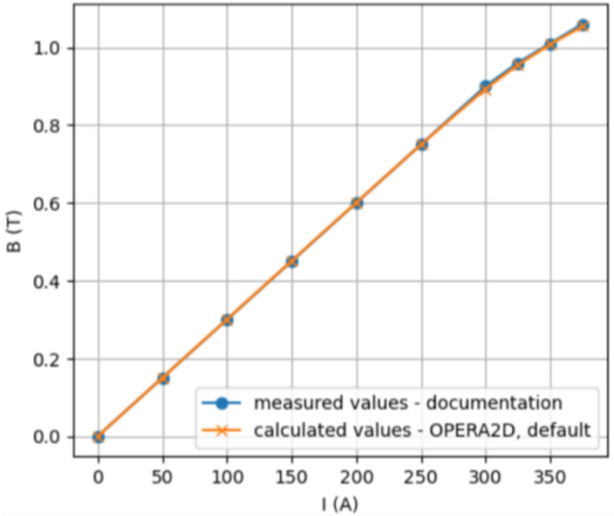
Current vs. B-Field for MDS Magnet

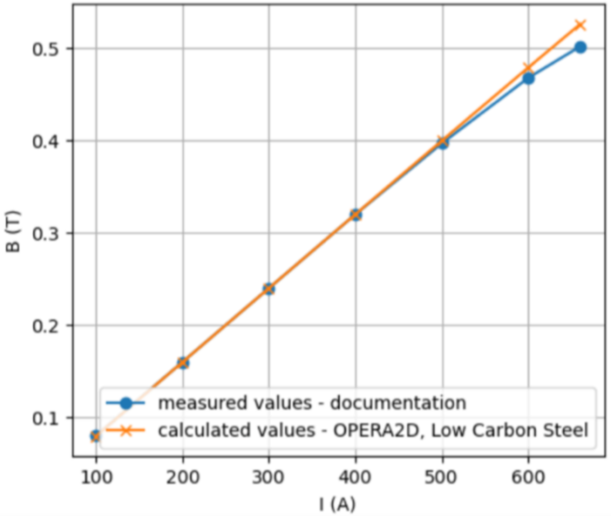
Current vs. B-Field for MDP Magnet

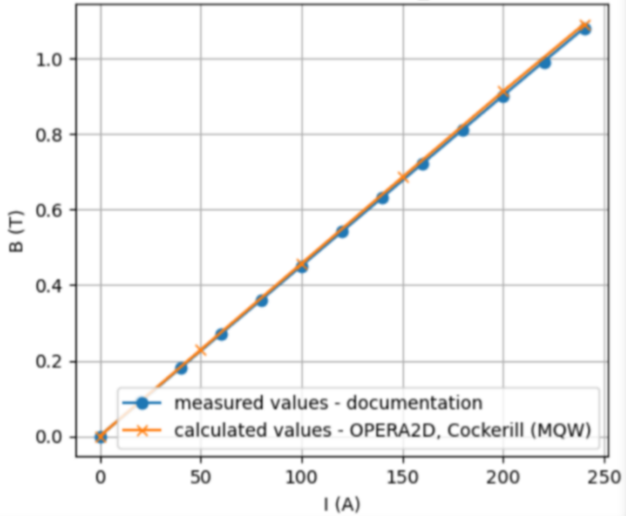
Current vs. B-Field for MDX_100 Magnet

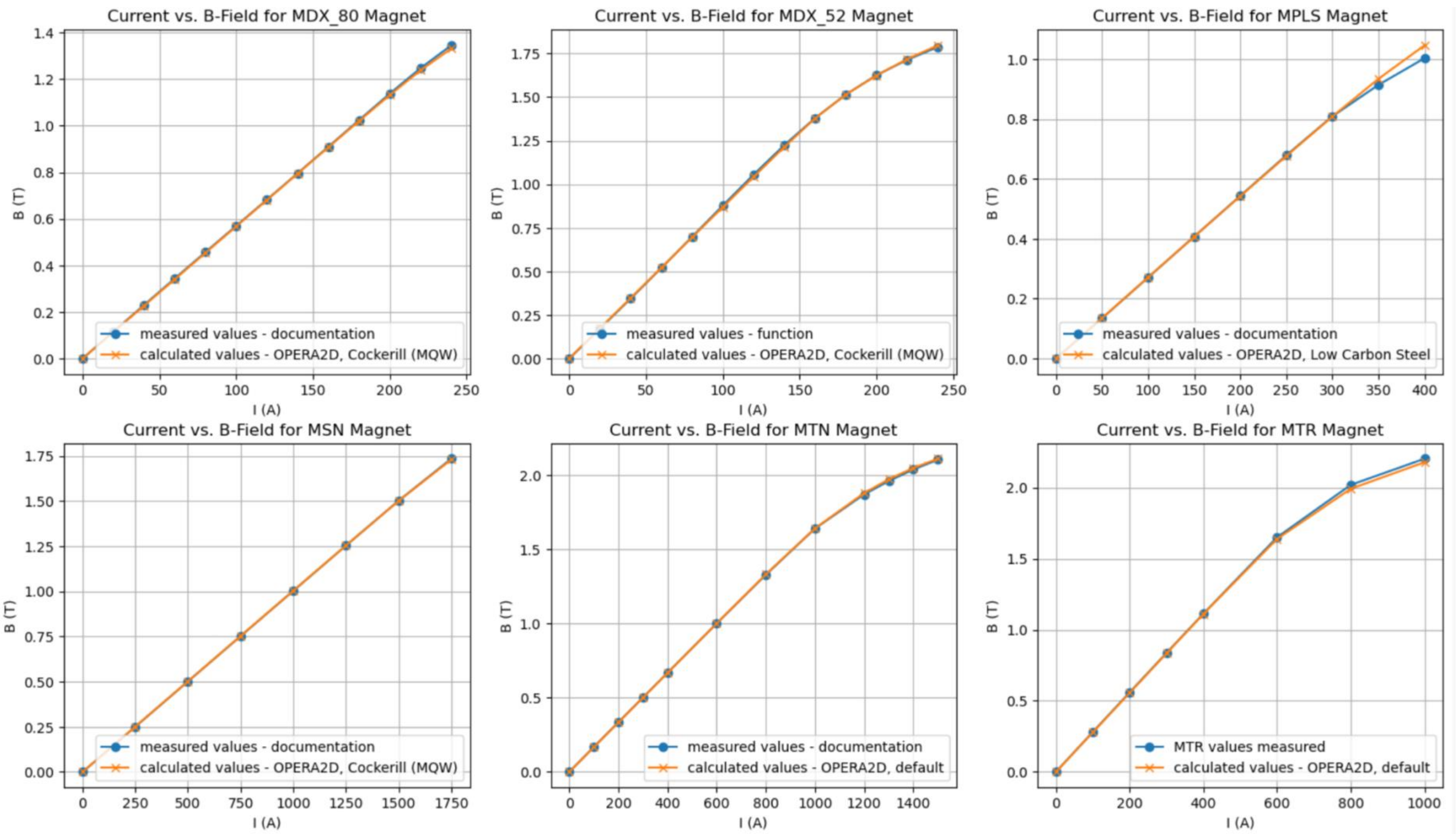
Current vs. B-Field for MDX_80 Magnet
B (T)
I (A)
0.0
0.2
0.4
0.6
0.8
1.0
1.2
1.4
0
50
100
150
200
250
measured values - documentation
calculated values - OPERA2D, Cockerill (MQW)
Current vs. B-Field for MDX_52 Magnet
B (T)
I (A)
0.00
0.25
0.50
0.75
1.00
1.25
1.50
1.75
0
50
100
150
200
250
measured values - function
calculated values - OPERA2D, Cockerill (MQW)
Current vs. B-Field for MPLS Magnet
B (T)
I (A)
0.0
0.2
0.4
0.6
0.8
1.0
0
50
100
150
200
250
300
350
400
measured values - documentation
calculated values - OPERA2D, Low Carbon Steel
Current vs. B-Field for MSN Magnet
B (T)
I (A)
0.00
0.25
0.50
0.75
1.00
1.25
1.50
1.75
0
250
500
750
1000
1250
1500
1750
measured values - documentation
calculated values - OPERA2D, Cockerill (MQW)
Current vs. B-Field for MTN Magnet
B (T)
I (A)
0.0
0.5
1.0
1.5
2.0
0
200
400
600
800
1000
1200
1400
measured values - documentation
calculated values - OPERA2D, default
Current vs. B-Field for MTR Magnet
B (T)
I (A)
0.0
0.5
1.0
1.5
2.0
0
200
400
600
800
1000
MTR values measured
calculated values - OPERA2D, default

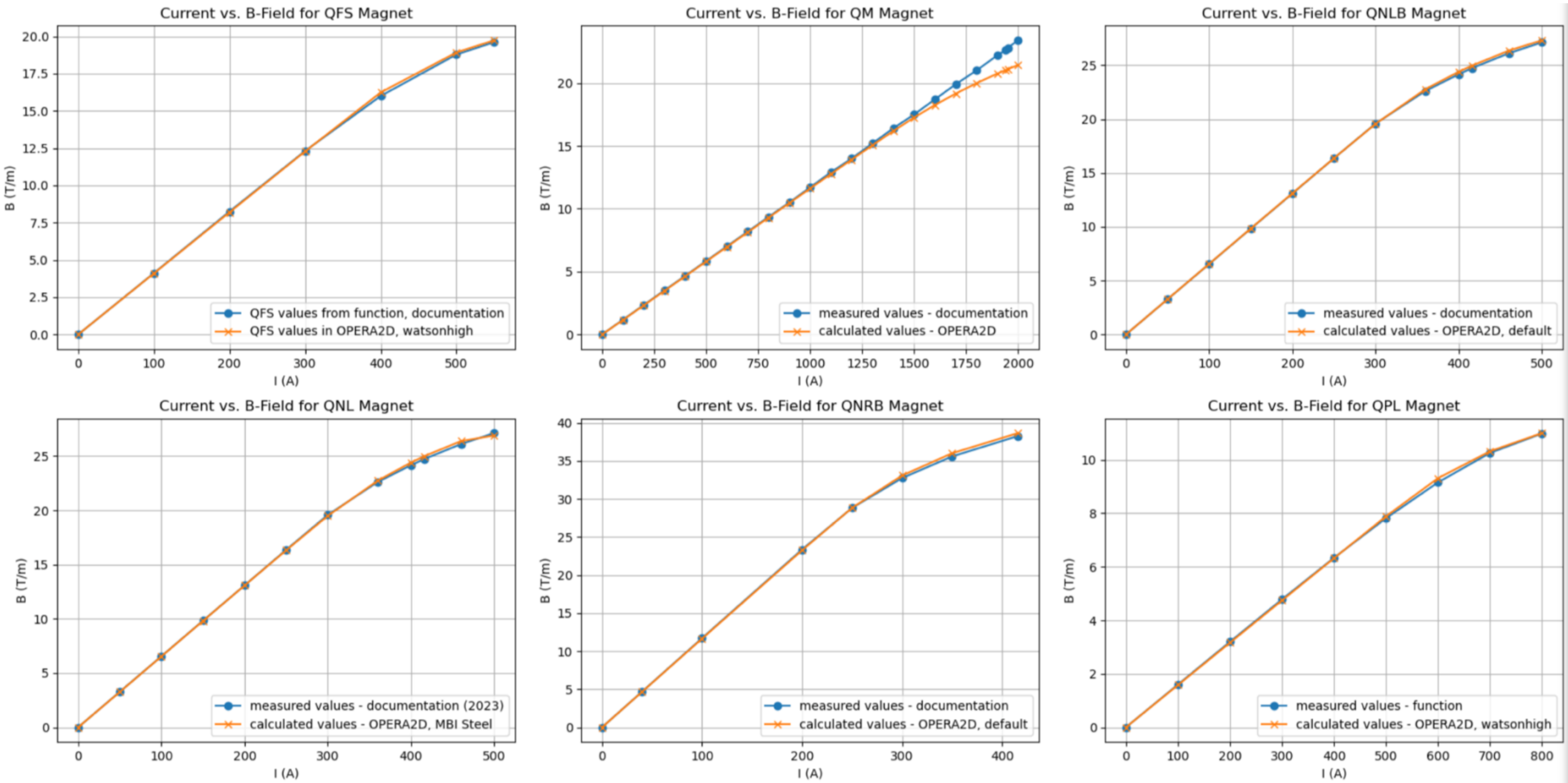
Current vs. B-Field for QFS Magnet
B (T/m)
0.0
2.5
5.0
7.5
10.0
12.5
15.0
17.5
20.0
I (A)
0
100
200
300
400
500
QFS values from function, documentation
QFS values in OPERA2D, watsonhigh
Current vs. B-Field for QM Magnet
B (T/m)
0
5
10
15
20
I (A)
0
250
500
750
1000
1250
1500
1750
2000
measured values - documentation
calculated values - OPERA2D
Current vs. B-Field for QNLB Magnet
B (T/m)
0
5
10
15
20
25
I (A)
0
100
200
300
400
500
measured values - documentation
calculated values - OPERA2D, default
Current vs. B-Field for QNL Magnet
B (T/m)
0
5
10
15
20
25
I (A)
0
100
200
300
400
500
measured values - documentation (2023)
calculated values - OPERA2D, MBI Steel
Current vs. B-Field for QNRB Magnet
B (T/m)
0
5
10
15
20
25
30
35
40
I (A)
0
100
200
300
400
measured values - documentation
calculated values - OPERA2D, default
Current vs. B-Field for QPL Magnet
B (T/m)
0
2
4
6
8
10
I (A)
0
100
200
300
400
500
600
700
800
measured values - function
calculated values - OPERA2D, watsonhigh

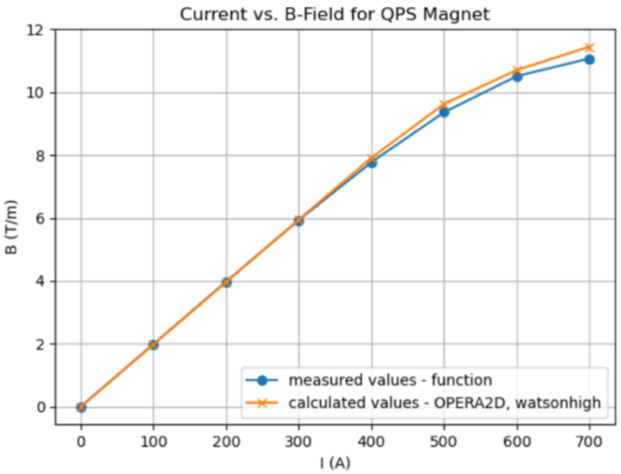
Current vs. B-Field for QPS Magnet
B (T/m)
0
2
4
6
8
10
12
I (A)
0
100
200
300
400
500
600
700
measured values - function
calculated values - OPERA2D, watsonhigh

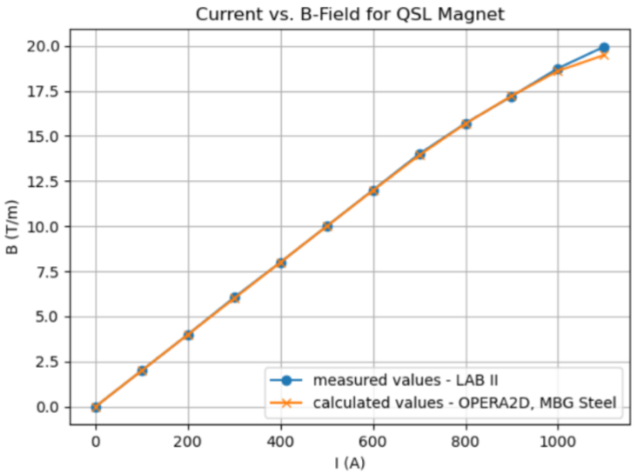
Current vs. B-Field for QSL Magnet
B (T/m)
0.0
2.5
5.0
7.5
10.0
12.5
15.0
17.5
20.0
I (A)
0
200
400
600
800
1000
measured values - LAB II
calculated values - OPERA2D, MBG Steel

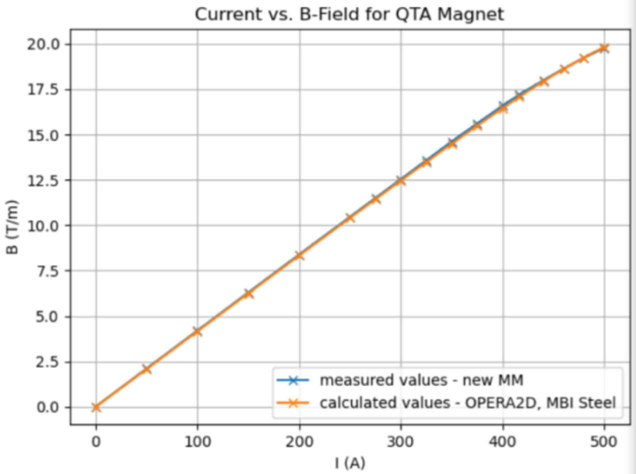
Current vs. B-Field for QTA Magnet
B (T/m)
0.0
2.5
5.0
7.5
10.0
12.5
15.0
17.5
20.0
I (A)
0
100
200
300
400
500
measured values - new MM
calculated values - OPERA2D, MBI Steel

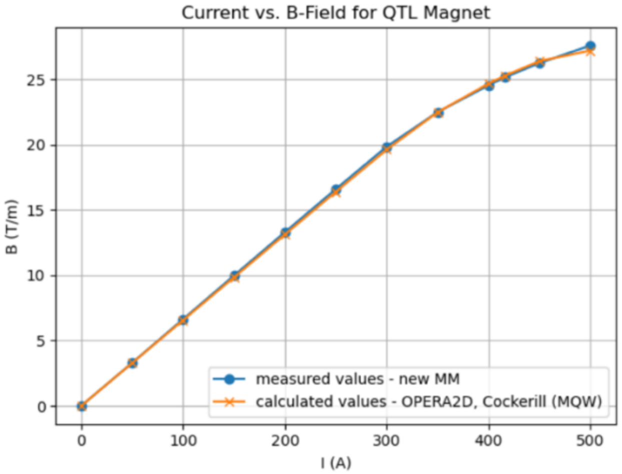
Current vs. B-Field for QTL Magnet
B (T/m)
0
5
10
15
20
25
I (A)
0
100
200
300
400
500
measured values - new MM
calculated values - OPERA2D, Cockerill (MQW)

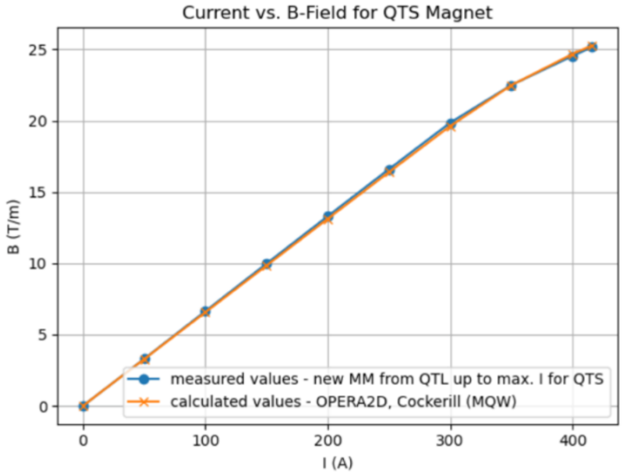
Current vs. B-Field for QTS Magnet
B (T/m)
0
5
10
15
20
25
I (A)
0
100
200
300
400
measured values - new MM from QTL up to max. I for QTS
calculated values - OPERA2D, Cockerill (MQW)

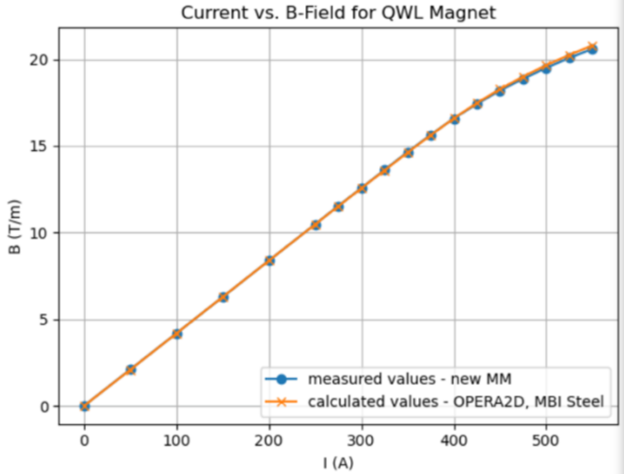
Current vs. B-Field for QWL Magnet
B (T/m)
0
5
10
15
20
I (A)
0
100
200
300
400
500
measured values - new MM
calculated values - OPERA2D, MBI Steel

Absolute and relative difference as well as total deviation of the BI curves using the old standard material MBS and the new standard material for each dipole (first table) and quadrupole (second table).

Magnet	Initial standard material	Max. Difference [T]	Max. Difference [%]	Total Difference	New standard Material	Max. Difference [T]	Max. Difference [%]	Total Difference
MAL	MBS	0.002	0.16	0.014	Iosil1000-65	0.004	0.22	0.013
MBE	MBS	0.015	1.00	0.345	Low Carbon Steel	0.017	1.06	0.209
MBN	MBS	0.636	3.01	0.169	MBG Steel	0.011	0.68	0.045
MBPL_110	MBS	0.040	2.40	0.143	Low Carbon Steel	0.068	3.03	0.138
MBPL_140	MBS	0.057	3.04	0.111	Low Carbon Steel	0.075	4	0.133
MBPL_170	MBS	0.024	1.41	0.057	Low Carbon Steel	0.036	2.07	0.043
MBPL_200	MBS	0.036	2.07	0.028	Low Carbon Steel	0.010	0.60	0.013
MBPS_140	MBS	0.074	5.19	0.354	Low Carbon Steel	0.064	4.50	0.271
MBW	MBS	0.018	2.61	0.089	Low Carbon Steel	0.014	1.80	0.052
MCA	MBS	0.024	1.99	0.053	default	0.020	1.88	0.048
MCB	MBS	0.060	3.47	0.361	default	0.022	3.10	0.012
MCV	MBS	0.009	0.74	0.053	default	0.005	0.43	0.040
MCVS	MBS	0.003	1.04	0.016	default	0.003	0.36	0.018
MCW	MBS	0.061	4.34	0.228	Low Carbon Steel	0.042	2.96	0.121
MDL	MBS	0.004	0.40	0.008	default	0.002	0.19	0.003
MDS	MBS	0.005	0.55	0.016	default	0.007	0.75	0.023
MDP	MBS	0.028	5.62	0.052	Low Carbon Steel	0.024	4.82	0.039
MDX_100	MBS	0.011	1.41	0.083	Cockerill (MQW)	0.058	5.69	0.099
MDX_80	MBS	0.022	1.63	0.066	Cockerill (MQW)	0.014	1.47	0.052
MDX_52	MBS	0.017	1.45	0.112	Cockerill (MQW)	0.013	1.53	0.060
MPLS	MBS	0.054	5.38	0.114	Low Carbon Steel	0.043	4.30	0.069
MSN	MBS	0.011	0.64	0.017	Cockerill (MQW)	0.005	0.26	0.008
MTN	MBS	0.052	2.46	0.108	default	0.013	0.79	0.047

MTR	MBS	0.105	4.78	0.145	default	0.027	1.34	0.074

Magnet	Initial standard material	Max. Difference [T/m]	Max. Difference [%]	Total Difference [T/m]	New standard Material	Max. Difference [T/m]	Max. Difference [%]	Total Difference [T/m]
QFS	MBS	0.647	3.30	1.377	watsonhigh	0.240	1.50	0.601
QNLB	MBS	0.359	1.32	1.398	default	0.245	0.96	1.149
QNL	MBS	0.317	1.31	1.482	MBI Steel	0.278	1.07	1.322
QNRB	MBS	0.467	1.31	1.570	default	0.424	1.19	1.345
QPL	MBS	0.310	2.82	0.835	watsonhigh	0.156	1.71	0.416
QPS	MBS	0.505	4.55	1.410	watsonhigh	0.376	3.40	1.001
QSL	MBS	0.975	4.89	1.638	MBG Steel	0.464	2.33	0.801
QTA	MBS	0.268	1.35	1.849	Low Carbon Steel	0.134	1.38	1.088
QTL	MBS	0.821	2.97	2.240	Cockerill (MQW)	0.393	1.42	1.660
QTS	MBS	0.255	1.34	1.267	Cockerill (MQW)	0.229	1.35	1.112
QWL	MBS	0.210	1.06	1.459	MBI Steel	0.262	1.27	0.922

10.4 Appendix D

The relative exceedance of the 0.1 T threshold for different materials inside the reference region for every magnet models at the two defined currents.

Current [A]	Cockerill (MQW)	default	Iosil1000-65	Low carbon steel	MBG Steel	MBI Steel	MBS	watsonhigh
	B-field values that exceed 0,1T in %							
	MAL, Iosil1000-65							
570	0.0000	0.0000		0.4528	5.084	0.463	0.0000	0.0000
1140	0	0.0504	-	0.3158	1.962	0.023	0.010	0.0134
	MBE, MBI Steel							
2875	0.0386	2.4181	0.1158	0.0000	0.004		0.000	0.2655
5750	0.0000	0.4060	0.1039	0.0000	0.000		0.000	0.5146
	MBN, MBG Steel							
670	2.7006	1.1240	5.0362	1.0598		0.005	0.201	2.8268
1340	0.1287	0.0486	1.0927	3.5929		0.005	0.011	1.0155
	MBPL_200, Low Carbon Steel							
425	0.0659	0.0209	0.1496	-	1.319	0.001	0.014	0.0097
850	0.4502	0.9707	0.1351	-	2.398	0.000	0.000	0.1506
	MBPL_170, Low Carbon Steel							
425	0.0173	0.0576	0.0123	-	1.516	0.008	0.047	0.0395
850	1.3867	6.6356	0.0966	-	7.011	0.000	0.000	0.0832
	MBPL_140, Low Carbon Steel							
425	0.106	0.391	0.048	-	1.951	0.005	0.206	0.201
850	1.522	18.405	0.092	-	8.812	0.000	0.000	0.378
	MBPL_110, Low Carbon Steel							
425	0.175	1.565	0.378	-	3.584	0.006	0.137	0.213
850	3.030	28.067	0.133	-	22.668	0.000	0.000	1.837
	MBPS_140, Low Carbon Steel							
338	0.0531	0.201	0.0372	-	1.683	0.010	0.127	0.1381
675	1.5031	15.42	0.0869	-	7.878	0.000	0.000	0.2454
	MBW, Low Carbon Steel							
494	0.1237	0.000	0.4330	-	0.680	0.000	0.000	0.0000
988	0.0298	0.089	0.0298	-	1.399	0.029	0.119	0.2382
	MCA, default							
717	0.3071	-	0.0000	0.0000	1.708	4.695	0.292	0.0000
1434	0.0000	-	0.0000	0.3219	0.074	0.536	0.000	0.0093
	MCB, default							
440	0.0000	-	0.0015	0.4798	0.089	0.523	0.006	0.0082
880	0.6043	-	4.4642	21.549	0.025	1.853	2.526	32.5250
	MCV, default							
638	0.119	-	0.328	0.170	0.140	0.104	0.030	0.110
1275	0.085	-	0.000	0.111	0.300	1.481	0.056	0.000
	MCVS, default							
200	4.863	-	0.318	0.000	1.293	14.139	0.611	0.020
400	0.956	-	0.000	0.141	0.295	1.486	0.089	0.000
	MCW, Low Carbon Steel							
500	0.0171	0.008	0.8300	-	1.831	0.000	0.008	0.0513
1000	6.9106	1.372	0.5310	-	4.664	0.000	0.106	0.3349
	MDL, default							

165	0.3527	-	0.0600	0.000	0.795	3.459	0.127	0.0000
330	0.0625	-	0.0069	1.8809	0.041	0.270	0.013	0.0000
	MDS, default							
125	1.541	-	0.096	0.000	0.819	6.985	0.193	0.000
250	0.487	-	0.000	0.044	0.398	0.973	0.089	0.000
	MDP, Low Carbon Steel							
300	0.1801	0.007	0.0113	-	0.153	0.000	0.000	0.0000
600	0.0355	0.042	0.0213	-	0.922	0.007	0.039	0.0426
	MDX_100, Cockerill (MQW)							
120	-	0.208	0.111	0.237	0.534	0.000	0.030	0.000
240	-	0.258	0.000	0.115	0.172	0.000	0.086	0.000
	MDX_80, Cockerill (MQW)							
120	-	0.000	0.0000	0.0443	1.108	0.000	0.108	0.0000
240	-	0.038	0.0000	0.0954	0.071	0.000	0.004	0.0048
	MDX_52, Cockerill (MQW)							
120	-	0.612	0.0000	0.0154	3.098	0.030	0.195	0.0000
240	-	0.005	0.0000	2.3762	0.020	0.000	0.000	1.4096
	MPLS, Low Carbon Steel							
193	0.2244	0.000	0.2557	-	0.426	0.000	0.000	0.0239
386	0.0209	0.127	0.0209	-	0.996	0.001	0.061	0.0890
	MSN, Cockerill (MQW)							
733	-	5.051	0.000	1.160	3.181	0.482	0.598	0.0000
1465	-	2.718	0.000	0.124	1.439	0.000	0.342	0.0000
	MTN, default							
725	1.2447	-	0.000	0.022	1.880	2.741	0.053	0.000
1450	0.4316	-	2.225	13.085	0.0218	0.574	0.388	0.657
	MTR, default							
410	0.794	-	0.000	0.010	1.747	4.931	0.081	0.000
820	0.124	-	0.542	5.384	0.100	0.317	0.052	1.114

Current (A)	**Cockerill (MQW)**	**default**	**Iosil1000-65**	**Low carbon steel**	**MBG Steel**	**MBI Steel**	**MBS**	**watsonhigh**
	B-field values that exceed 0,1T/m in %							
	QFS, watsonhigh							
250	0.0000	0.0000	0.0000	0.077	0.512	3.3996	0.077	-
500	0.0000	0.0000	0.0000	0.099	5.424	0.0638	0.000	-
	QNLB, default							
208	1.5551	-	0.6794	7.316	3.856	17.196	2.976	0.0157
416	1.6704	-	0.0000	3.724	0.921	2.6622	0.737	0.2249
	QNL, MBI Steel							
208	3.0906	18.202	9.2635	2.716	1.163	-	1.500	9.4279
416	2.3146	2.7442	1.2555	2.529	2.836	-	1.918	2.3554
	QNRB, default							
208	0.7960	-	0.0000	0.398	3.1841	10.398	1.293	0.0000
416	1.0984	-	4.6800	8.643	0.8118	1.767	0.1910	6.6141
	QPL, watsonhigh							
375	0.0000	0.0000	0.0000	0.000	2.0243	0.396	0.0000	-
750	0.0299	0.0479	0.0299	0.299	1.142	0.083	0.0120	-
	QPS, watsonhigh							
350	0.0000	0.0000	0.0000	0.0348	4.8432	0.0871	0.0000	-
700	0.2321	0.8455	0.0332	0.0995	3.9125	0.1326	0.0332	-

	QSL, MBG Steel							
500	3.4127	1.6956	3.1230	0.3971	-	0.1288	0.0859	1.7600
1000	6.9824	0.6403	12.3488	9.0558	-	0.3456	1.3924	13.3144
	QTA, Low Carbon Steel							
208	4.9309	6.1030	2.9343	-	4.7091	3.1185	3.4282	3.2231
416	7.5212	5.3855	5.9204	-	11.305	2.3659	3.6844	5.7012
	QTL, Cockerill(MQW)							
208	-	1.542	0.783	6.415	4.730	2.539	0.113	0.237
416	-	1.666	1.655	11.952	6.973	2.368	0.026	0.000
	QTS, Cockerill(MQW)							
208	-	1.5424	0.7831	6.414	4.730	2.539	2.258	0.2373
416	-	1.6657	1.6547	11.952	6.973	2.367	0.025	0.0000
	QWL, MBI Steel							
250	3.0794	17.478	8.4162	3.323	1.331	-	1.7048	8.6854
500	1.8227	1.5458	0.1642	2.3219	0.3864	-	0.8985	1.3622

10.5 Appendix E

10.5.1 Determination of the Score for the Results Validation Plot V1

Magnet	Total absolute difference [T]	Score
MAL	0.013	0
MBE	0.209	2
MBN	0.045	1
MBPL_110	0.111	2
MBPL_140	0.197	3
MBPL_170	0.043	0
MBPL_200	0.013	0
MBPS_140	0.271	5
MBW	0.052	1
MCA	0.048	0
MCB	0.012	0
MCV	0.018	0
MCVS	0.015	0
MCW	0.121	2
MDL	0.003	0
MDS	0.014	0
MDP	0.039	0
MDX_100	0.032	0
MDX_80	0.052	1
MDX_52	0.06	1
MPLS	0.069	1
MSN	0.008	0
MTN	0.047	0
MTR	0.069	1

Magnet	Total absolute difference [T/m]	Score
QFS	0.601	2
QNLB	1.149	3
QNL	1.322	3
QNRB	1.345	3
QPL	0.416	1
QPS	1.001	3
QSL	0.801	2
QTA	1.088	3
QTL	1.424	3
QTS	1.112	3
QWL	0.922	2

10.5.2 Determination of the Score for the Material Uncertainity & Sensitivity M1

Magnet	# exceedance lin. Reg.	Score	# exceedance sat. Reg.	Score	Sum of scores
MAL	1	0.71	1	0.71	0.71
MBE	1	0.71	0	0	0.355
MBN	5	3.57	2	1.43	2.5
MBPL_110	2	1.43	4	2.86	2.415
MBPL_140	1	0.71	3	2.14	1.425
MBPL_170	1	0.71	2	1.43	1.07
MBPL_200	1	0.71	1	0.71	0.71
MBPS_140	1	0.71	3	2.14	1.425
MBW	0	0	1	0.71	0.355
MCA	2	1.43	1	0.71	1.07
MCB	0	0	5	3.57	1.785
MCV	0	0	1	0.71	0.71
MCVS	3	2.14	1	0.71	1.425
MCW	1	0.71	3	2.14	1.425
MDL	1	0.71	1	0.71	0.71
MDS	1	0.71	1	0.71	0.71
MDP	0	0	0	0	0
MDX_100	0	0	0	0	0
MDX_80	1	0.71	0	0	0.355
MDX_52	1	0.71	2	1.43	1.07
MPLS	0	0	0	0	0
MSN	3	2.14	2	1.43	1.785
MTN	3	2.14	2	1.43	1.785
MTR	2	1.43	2	1.43	1.43
QFS	1	0.71	1	0.71	0.71
QNLB	5	3.57	3	2.14	2.855
QNL	7	5	7	5	5
QNRB	3	2.14	5	3.57	2.855
QPL	1	0.71	1	0.71	0.71
QPS	1	0.71	1	0.71	0.71
QSL	4	2.86	5	3.57	2.855
QTA	6	4.29	7	5	4.645
QTL	4	2.86	5	3.57	3.215
QTS	5	3.57	5	3.57	3.57
QWL	7	5	4	2.86	3.93

10.5.3 All four criterias scored, not weighted

Magnet	Geometry Inaccurities G1	Availability of measured BI curves B1	Results Validation Plot V1	Material Uncertainity & sensitivity M1
MAL	0	1	0	0.71
MBE	0	3	2	0.355
MBN	0	0	1	2.5
MBPL_110	1	1	2	2.415
MBPL_140	1	1	3	1.425
MBPL_170	1	1	0	1.07
MBPL_200	1	1	0	0.71
MBPS_140	1	1	5	1.425
MBW	0	3	1	0.355
MCA	0	0	0	1.07
MCB	0	0	0	1.785
MCV	0	0	0	0.71
MCVS	0	0	0	1.425
MCW	0	3	2	1.425
MDL	0	1	0	0.71
MDS	0	3	0	0.71
MDP	2.5	3	0	0
MDX_100	1	0	0	0
MDX_80	1	0	1	0.355
MDX_52	1	0	1	1.07
MPLS	0.5	2	1	0
MSN	0	0	0	1.785
MTN	0	0	0	1.785
MTR	0	1	1	1.43

Magnet	Geometry Inaccurities G1	Availability of measured BI curves B1	Results Validation Plot V1	Material Uncertainity & sensitivity M1
QFS	5	0	2	0.71
QNLB	0	2	3	2.855
QNL	0	0	3	5
QNRB	0	0	3	2.855
QPL	5	0	1	0.71
QPS	5	0	3	0.71
QSL	0	3	2	2.855
QTA	2	0	3	4.645
QTL	0	0	3	3.215

QTS	0	0	3	3.57
QWL	0	0	2	3.93

10.5.4 All four criterias scored and weighted

Magnet	**G1 * WF**	**B1 * WF**	**V1 * WF**	**M1 * WF**	**U**
MAL	0	0.1	0	0.213	0.313
MBE	0	0.3	0.4	0.1065	0.8065
MBN	0	0	0.2	0.75	0.95
MBPL_110	0.4	0.1	0.4	0.7245	1.6245
MBPL_140	0.4	0.1	0.6	0.4275	1.5275
MBPL_170	0.4	0.1	0	0.321	0.821
MBPL_200	0.4	0.1	0	0.213	0.713
MBPS_140	0.4	0.1	1	0.4275	1.9275
MBW	0	0.3	0.2	0.4275	0.9275
MCA	0	0	0	0.321	0.321
MCB	0	0	0	0.5355	0.5355
MCV	0	0	0	0.213	0.213
MCVS	0	0	0	0.4275	0.4275
MCW	0	0.3	0.4	1.425	2.125
MDL	0	0.1	0	0.213	0.313
MDS	0	0.3	0	0.213	0.513
MDP	1	0.3	0	0	1.3
MDX_100	0.4	0	0	0	0.4
MDX_80	0.4	0	0.2	0.1065	0.7065
MDX_52	0.4	0	0.2	0.321	0.921
MPLS	0.2	0.2	0.2	0	0.6
MSN	0	0	0	0.5355	0.5355
MTN	0	0	0	0.5355	0.5355
MTR	0	0.1	0.2	0.429	0.729

Magnet	**G1 * WF**	**B1 * WF**	**V1 * WF**	**M1 * WF**	**U**
QFS	2	0	0.4	0.213	2.613
QNLB	0	0.2	0.6	0.8565	1.6565
QNL	0	0	0.6	1.5	2.1
QNRB	0	0	0.6	0.8565	1.4565
QPL	2	0	0.2	0.213	2.413
QPS	2	0	0.6	0.213	2.813

QSL	0	0.3	0.4	0.8565	1.5565
QTA	0.8	0	0.6	1.3935	2.7935
QTL	0	0	0.6	0.9645	1.5645
QTS	0	0	0.6	1.071	1.671
QWL	0	0	0.4	1.179	1.579